NASA Lunabotics 2023-2024

A Major Qualifying Project Report

submitted to the faculty of

WORCESTER POLYTECHNIC INSTITUTE

in partial fulfillment of the requirements for the

degree of Bachelor of Science

by

Brendan Byrne (CS/RBE)

Zeb Carty (ME)

Giovanni Giacalone (RBE)

Kelli Huang (ME)

Ian MacInerney (ME/RBE)

James Nguyen (ME)

Terence Tan (ME)

Sean Thal (ME)

Submitted to:

Professor Kenneth Stafford, Advisor

Professor Carlo Pinciroli, Advisor


WPI LUNABOTICS
2024

Abstract

The NASA Lunabotics Challenge is a robotics competition that allows teams from across the country to design and build a lunar mining robot. Teams can prove their engineering skills by showcasing a robot with the ability to navigate simulated lunar terrain, collect regolith, and construct a berm on the regolith surface. With new competition rules this year, the WPI Lunabotics Team designed and manufactured Muffin. A lightweight, agile, and autonomous robot, Muffin takes inspiration from successful robots at past Lunabotics competitions. The project also allowed the team to develop invaluable engineering skills they will use throughout their careers. Using these skills, the team created innovative subsystems to meet the challenges of the competition.

Acknowledgements

The Worcester Polytechnic Institute Lunabotics Team would like to thank Professor Kenneth Stafford and Professor Carlo Pinciroli for advising the project. We would also like to thank Jay Blauser, Brian Boxell, Alex Brown, Gabe Brown, Joel Harris, Josh Mallette, and Andrew Qi for their manufacturing support. Finally, the team would like to thank our sponsors, which made this project possible: WPI, Michael Ciaraldi, WPI Voyagers, Overthrow Inc., the Gene Haas Foundation, and the Massachusetts Space Grant Consortium.

Contents

List of Figures

List of Tables

Table of Authorship

Section		Author(s)
Executive Summary		Kelli, Zeb
1	*Introduction*	Kelli
2	*Background*	Zeb
2.1	*Competition*	Zeb
2.2	*Previous Lunabotics*	Kelli
3	*Statement of Work*	Giovanni, Zeb
4.1	*Concept of Operations (CONOPs)*	Ian
4.2	*Robot Layout*	James, Terence
4.3	*Drive Base*	Ian, James
4.3.1	*Chassis*	James, Ian
4.3.2	*Drivetrain*	James, Ian
4.3.3	*Ground Interface*	Ian
4.3.4	*Suspension*	Ian
4.3.5	*Prototype*	Ian
4.4	*Regolith Management*	Terence, Sean, Zeb
4.4.1	*Intake*	Terence, Sean, Zeb
4.4.2	*Storage/Deposit*	Kelli, Terence
4.5	*Electronics*	Ian, Giovanni
4.5.1	*System Architecture*	Ian, Giovanni
4.5.2	*Communications*	Ian, Giovanni
4.6	*Software*	Brendan
4.6.1	*System Architecture*	Brendan
4.6.2	*Environment*	Giovanni, Brendan
4.6.3	*Localization and Pose Estimation*	Giovanni, Ian
4.6.4	*Obstacle Detection*	Giovanni
4.6.5	*Mapping and Autonomous Navigation*	Giovanni
4.6.6	*Subsystem Controls*	Ian
5.1	*Drive Base*	Zeb
5.2.1	*Intake*	Sean, Zeb
5.2.2	*Storage & Deposit*	Kelli, Terence
5.3	*Electronics*	Zeb
5.4	*Software*	Zeb
5.5	*Validation*	Zeb
6.1	*Requirements*	Zeb
6.2	*Drive Base*	Zeb
6.3.1	*Intake*	Zeb
6.3.2	*Storage & Deposit*	Kelli, Zeb
6.4	*Electronics*	Zeb
6.5	*Software*	Zeb
7.1	*Timeline*	James, Zeb
7.2	*Budget*	Sean, Zeb
8	*Conclusions and Recommendations*	Kelli, Terence

References	Zeb
Appendix A: Regolith Rate/Capacity Analysis	Terence, Sean, Zeb
Appendix B: Drive Train Tube Calculations	Terence
Appendix C: Safety Requirements Checklist	Zeb

Executive Summary

NASA's Lunabotics Challenge provides institutions of higher education with the opportunity to design a robot capable of performing operations on the lunar surface in support of their mission to return humanity to the Moon and establish a permanent residency. This year, teams must fabricate a robot to extract regolith from an obstacle-ridden excavation zone and deliver it to a designated berm area. The scoring system pushes teams to design with the Artemis Mission in mind, penalizing mass and power consumption while awarding efforts towards full autonomy.

The guidelines of the challenge provided the framework for this project. Using competition requirements, our team developed technical goals that challenged our engineering skills and pushed the team to develop a competitive robot, Muffin. We held a Systems Requirements Review (SRR) to address the attainability of these goals, and subsequently developed Technical Performance Measures (TPMs) that the team would work towards for the remainder of the project.

To design a robot capable of meeting our technical requirements, we brainstormed techniques for robot mobility, management of regolith, and software capabilities. We completed trade studies for these techniques, determining which design was most feasible for our project. We conducted Preliminary and Critical Design Reviews at important design milestones, evaluating the attainability of our technical requirements. Finally, we tested each system, assessing its ability to perform subsystem requisites.

The robot can be broken down into four main subsystems: Drive Base, Intake, Storage/Deposit, and Electronics/Software. Each system was carefully optimized to achieve the level of low-mass and power consumption that we aimed for.

The drive base is responsible for the locomotion of the robot. From watching previous Lunabotics competition runs, the team observed that many robots utilized a skid steering style, but the harsh nature of the regolith caused the wheels to spin out or smear through the regolith—wasting a large amount of power. With our design, the team prioritized maneuverability of the drivetrain and buoyancy while traversing through the regolith. The final design features a duplex swerve steering style, where the wheels on the right side are mechanically linked, as well as the wheels on the left. This allows the robot to drive forward, perform point turns, and turn about an instantaneous center of curvature with minimal smear. A rocker suspension system with differential shaft ensures that all four wheels maintain contact with the ground to prevent the wheels from spinning out.

The goal of the robot is to collect regolith from the excavation zone and deliver it to the berm construction zone. The top priority for the regolith management systems was reliability and mass optimization. The intake consists of a bucket ladder conveyor belt actuated into the regolith by a lead screw. We chose this method because of its simplicity to control and its history of success in previous Lunabotics robots. Once the regolith is collected, it gets transferred to the storage and deposit system, which must contain the regolith during transportation, then unload all of it when commanded. The storage compartment is made of a

load-bearing aluminum structure and fiberglass walls to balance rigidity and low-mass design. A trap door mechanism at the bottom of the storage deposits the entire load of regolith with a simple linear actuation, minimizing the power required to complete the cycle. These mechanisms also feature several dust mitigation features to reduce the chance of regolith impeding robot ability.

A high priority of lunar rovers is their ability to operate with limited human control. Aptly, the electronics and software package allow the team to control all systems through teleoperation as well as autonomy. The robot also can autonomously detect obstacles, determine its pose with respect to its starting location, and map areas of drivable territory. Furthermore, the robot can plan paths through this territory using the A* algorithm with Pure Pursuit, utilizing all three steering techniques. After navigating around obstacles, autonomous control allows the robot to collect material while limiting jamming and deposit material once completed with an excavation cycle.

The robot was able to partially complete its technical requirements by the conclusion of the project. The mobility of the robot allowed it to agilely maneuver across uneven terrain, while the lightweight design of the robot kept the total mass of the robot relatively low. The robot also met all required safety goals. By the conclusion of the project, the robot demonstrated its ability to autonomously navigate around obstacles and collect the required volume of berm; however, the team was unable to completely validate these technical requirements. The robot also never proved its ability to run interrupted for 30 minutes, although the team rigorously tested the dust isolation and analyzed the energy usage for long-term trials.

Through our experience working on the project, our team recommends keeping and utilizing a detailed timeline to track the progress towards technical goals. This timeline is a great tool to work more efficiently and will save effort and prevent unforeseen setbacks. Although setbacks are unavoidable at a project of this scale, constant communication between the team will ensure smooth integration between subsystems and proper management of deadlines.

Our team intends on improving the reliability of our robot and validating all remaining minimum objectives before competing in the Lunabotics Challenge. Past this project, autonomous robots will use berm construction methods to protect semi-permanent lunar structures, aiding in mankind’s first effort towards space colonization.

1 Introduction

It has been almost 50 years since astronauts last walked on the Moon's surface during the Apollo program. Now, NASA plans to send the first woman and person of color to the Moon as soon as 2024 [1]. The Artemis Mission will push humans to return to the Moon and investigate sustainable lunar exploration, paving the way to Mars and beyond. Astronauts will live and work on the Moon, collecting and analyzing samples to unravel some of the greatest mysteries in our solar system for the benefit of humanity. They will be supported by a collection of rovers that will expand the range of exploration and scientific return, allowing humans to stay on the Moon for a long period. NASA engineers are not the only ones involved in this mission, however. The program also works to inspire the next generation of astronauts by hosting educational activities and competitions that challenge students to explore what it takes to live and operate on the Moon.

NASA's Lunabotics Challenge provides institutions of higher education with the opportunity to design and build a robot capable of performing operations on the lunar surface in support of future Artemis Mission goals [2]. To operate on the Moon, a robot needs to semi-autonomously traverse the chaotic terrain while protecting itself from the surface's abrasive lunar dust, or regolith. Previous competitions have challenged students to dig deep down into a regolith stimulant-filled area to collect and deliver gravel stones, simulating the icy regolith samples that humans will collect and research. Iterations of these Lunabotics mining robots will be explored in a future section. This year, however, NASA brought on a brand-new challenge.

The Artemis Mission will use regolith-based berm structures for blast and ejecta protection during lunar landings and launches, shading cryogenic propellant tank farms, and providing radiation protection around nuclear power plants [3]. This year, NASA challenges students to build a robot capable of extracting regolith from an obstacle-ridden excavation zone and delivering it to a designated berm area. The scoring system pushes teams to design with the Artemis Mission in mind, penalizing mass and power consumption while awarding efforts towards full autonomy. The WPI team took on the challenge to create a robot that can not only complete the mission, but also expand each member's personal education and experience. The realization of this project also fulfills WPI's requirements to complete a Major Qualifying Project (MQP) while adhering to the NASA Challenge's guidelines. To reach these goals, the team drew inspiration from previous teams' discoveries and applied them to the new task of berm construction.

The WPI Lunabotics Team designed, fabricated, and tested a robot to compete in the NASA Lunabotics Challenge. The robot can semi-autonomously navigate across the rough lunar terrain, actively avoiding obstacles. It is designed to complete at least one full digging and delivery cycle within its 15-minute competition run. The team aimed to make a small, low-mass robot to achieve a high score in the competition and meet each of the team's technical requirements.

2 Background

2.1 Competition

The Lunabotics Challenge is a long-running NASA Challenge focused on developing lunar mining robots to complete a simulated lunar mission. The 2024 Lunabotics Guidebook [3] details the rules and requirements of this year's challenge. In 2024, entrants must build a robot that can dig regolith and construct a berm on the simulated lunar surface. While participating in the Lunabotics Challenge, students develop engineering skills and learn more about systems engineering by completing several deliverables to submit to NASA. Ultimately, the designs developed as a part of the 2024 Lunabotics Challenge can provide NASA with novel ideas and solutions to potential challenges brought up by the Artemis Mission.

As stated in [3], the competition is divided into an initial development phase, a qualification round, and a final round. The development portion of the contest consists of several deliverables. Teams participating in the 2024 Lunabotics Challenge must submit a STEM engagement report, presentation and demonstration slides, a systems engineering paper, and a proof of life video. After completing the development process, a qualification round takes place at the University of Central Florida (UCF) and consists of two 15-minute attempts where teams must collect regolith from an excavation zone and construct a berm within a specified target area. The highest performing teams will then perform a similar task in one longer, 30-minute attempt at Kennedy Space Center (KSC).

The overall performance of each team is based on the deliverables, as well as the team's performance in the qualification and final challenges. There are several metrics used to grade a team's performance during the construction attempts, listed in [3]. For example, a team scores more points if their robot is of less mass, constructs a greater volume of berm, or maneuvers autonomously.

2.2 Previous Lunabotics

To build a successful robot, we first looked at past Lunabotics teams to identify what methods worked for them and what we could improve. The first teams we looked at were the WPI Lunabotics teams from 2021-2023, reviewing the documentation contained in [4], [5].

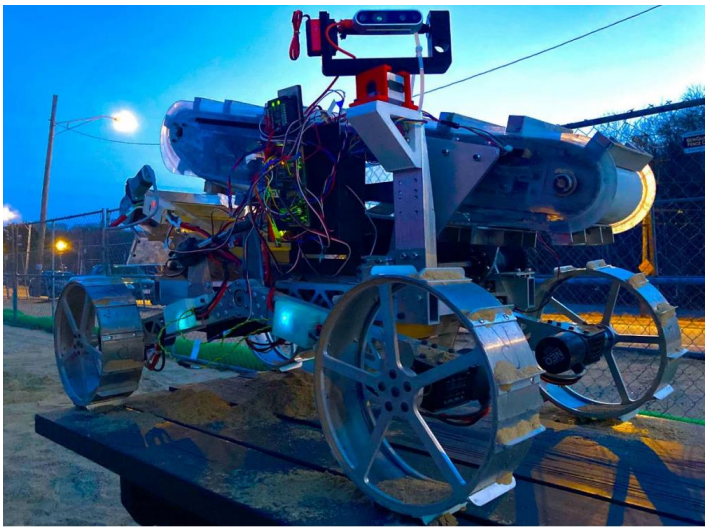

Fig. 2.1 2022 WPI Lunabotics Robot. [4].

In 2022, WPI students designed and built Project COMET. Fig. 2.1 shows the 2022 Lunabotics robot. The goal of the robot was to traverse a regolith-filled arena, dig deep down to retrieve the gravel rocks underneath, and deliver them to the collection point. The team used four-wheel-drive skid steering to maneuver their rocker-type chassis around the area. The robot had two conveyor belts: one for digging deep into the regolith and one to deliver the gravel up to the collection sieve. The team was successful in designing their robot to be well within their mass, speed, and power consumption goals. However, they failed to reach the level of partial autonomy that they aimed for and collected less gravel than expected [4].

The 2023 WPI team inherited the previous year's robot and sought to improve it. They aimed to make the robot partially autonomous and redesign several mechanical systems to increase the amount of gravel collected. The team was able to increase the ground clearance and decrease mechanical complexity by replacing the depositing conveyor belt with a bucket lever arm. The team coded the robot to nearly full autonomy but experienced several compatibility issues when integrating with the robot. Overall, the team recommended that future students aim for neater wiring and better software compatibility [5].

For the past several years, the University of Alabama team, Alabama Astrobotics, has been the reigning champion of the NASA Lunabotics Challenge. Their robot has been passed down through many years, allowing them to continually reiterate and improve their design. Information about the Astrobotics team can be found in [6]. Fig. 2.2 shows the Astrobotics robot for 2022.

Fig. 2.2 2022 Alabama Astrobotics Robot. [6].

The outriggers located in each corner of the robot can adjust the vehicle's ground clearance, expand the robot's effective wheelbase during stationary operations, allowing for a more tightly packed robot. The team also has a noticeably faster cycle time than other teams. Most competitors can complete a single cycle within the 15-minute competition run, but the Astrobots are able to complete three full cycles, helping them to collect the highest amount of gravel.

The final robot that the team explored was WPI's own Moonraker 2.0. Led by Paul Ventimiglia, The Moonraker 2.0 competed and won NASA's Regolith Excavation Challenge in 2009. Like the Challenge this year, Moonraker 2.0 collected regolith from a 16-square-meter arena and deposited it in a collection area. Moonraker 2.0 is shown in Fig. 2.3. The robot was able to collect and deliver 439 kg of regolith in a 30-minute competition run [7].

Fig. 2.3 Moonraker 2.0. [8].

Some key features of the robot include its lightweight chain system for regolith collection and its treads. To deposit regolith, the entire upper half of the robot tips backwards, dumping its entire load into the collection area. The time needed to complete one whole cycle is three minutes, which is much faster than most robots that compete in the recent Lunabotics Challenges [9].

3 Statement of Work

The goal of this year's Challenge is to produce a robot that can traverse uncertain terrain, dig into the ground to excavate lunar regolith simulant, and navigate to the berm construction site to deposit the regolith simulant. As a team, we determined our technical objectives methodically, by maximizing the number of points our robot can score during a competition attempt. As such, we have identified that the most important design considerations for this year's challenge are to reduce the total mass of the robot, reflected in the real world by the disproportionate cost associated with sending payloads to orbit compared to other mission costs. This will also reduce the overall power consumption of our robot. While mass and power consumption are important design considerations, excavating regolith and constructing high volume berms are clearly essential goals. Aligning with these objectives, we designed our robot to complete multiple digging and deposition cycles during competition run.

From a hardware point of view, we want to prioritize mission longevity and resistance to wear overtime due to environmental conditions over berm construction efficiency. The lunar environment is a harsh and unforgiving place, where FOD (foreign object debris/damage) can rapidly decommission a robot over time. With this in mind, we aimed to design systems that are either highly resistant to dust penetration or reliably operable in a dusty environment.

Autonomy is also important for this year's challenge. A robot that incorporates a prominent level of autonomy earns points from the autonomy bonuses. In addition, it reduces the Mission Control Center operator's reliance on situational awareness cameras, which limits bandwidth penalties. The team aimed to design and produce a robot system capable of addressing all the challenges guided by the design optimization criteria. Specifically, we prioritized a highly autonomous robot that consumes minimal power and bandwidth resources.

Based on the technical objectives, the team developed Technical Performance Measures (TPM), written with minimum and reach goals. These goals were derived from the 2024 Lunabotics Guidebook [3], as well as metrics that were important to the team. The reach goals serve as a vision of our project's extent and are in no particular order of importance. Each TPM also has an allocation that describes what part of the robot the measure corresponds to. The TPM shown in Table 3.1 serves as a visual representation of our team's plan to measure the technical performance of our project and each TPM is mapped to the Robot System Hierarchy shown in Fig. 3.1.

Table 3.1 Technical Performance Measures.

Technical Performance Measures	Minimum Goals	Reach Goals	TPM Allocation
Movement	Shall be able to traverse at least 7 m in 2 min. Shall not get stuck on rocks or in craters.	Should be able to traverse at least 7 m in 1 min.	Drivetrain/ Chassis
Berm Construction	Shall be able to deposit at least 0.01 m^3 of regolith in the berm construction zone after 15 min of operation.	Should be able to deposit at least 0.03 m^3 of regolith in the berm construction zone after 15 min of operation.	BP-1 Management
Dust Protection	Shall not lose functionality due to ingress of particulate matter after operating for 30 min in sand.	Should operate without the ingress of particulate matter in any critical system.	CPU, Hardware
Maximum Mass	Shall be less than 40 kgs.	Should be less than 20 kgs.	Hardware
Size Requirements	Shall fit within an envelope of 1.50 m x 0.75 m x 0.75 m.	-	Hardware
Energy Consumption	Shall be able to operate for at least 30 min.	Should be able to operate for at least 45 min.	Power
Autonomy	Shall be able to detect obstacles, prevent collisions, and complete the digging sequence autonomously.	Should be able to complete navigation, digging, and dumping completely autonomously.	Software
Safety	Shall comply with competition required safety precautions as defined in the Lunabotics guidebook.	Should have a graphical display of robot system telemetry for monitoring purposes.	Hardware, Power Systems

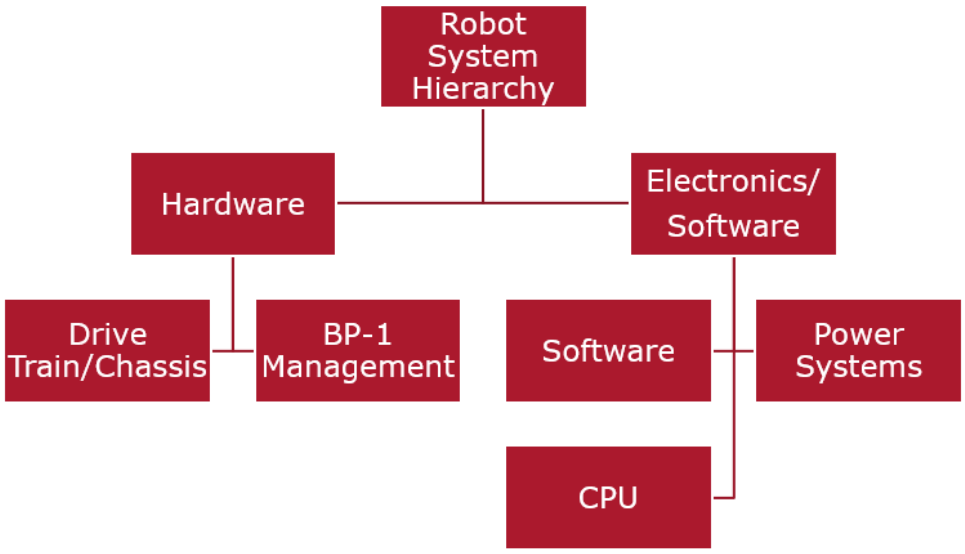

Fig. 3.1 Robot System Hierarchy.

4 Design

4.1 Concept of Operations (CONOPs)

The team developed a concept of operations to achieve the goals defined by the statement of work, as shown in Fig. 4.1. The competition zones can be found in Fig. 4.2. The robot starts in the designated start location. Upon boot, the robot calibrates any critical systems and determines the starting positions of all its actuators. When the run is started, the robot localizes itself with respect to the field using its onboard camera and a fiducial marker placed in the starting zone, as well as one or more beacons placed in the construction zone. Once localization is completed, the robot begins autonomously navigating to the excavation zone. When the robot reaches the excavation zone, it begins to intake regolith. As it digs, it continuously checks how much time is left, for how long it has dug, and whether the intake has jammed. If the robot determines that there is not enough time to finish its digging cycle or the storage is full (based on digging time), it will stop. If the robot determines that it is jammed, it runs a troubleshooting protocol. If still jammed, the robot ends regolith collection. Once regolith extraction is done, the robot navigates to the berm building zone (marked by the beacon), where it deposits all the collected material. Finally, the robot determines if enough time is left for another deposit cycle. If there is sufficient time remaining, the robot navigates back to the excavation zone to perform another cycle. Otherwise, the run is complete, and the robot enters a power-saving mode.

The robot is intended to operate autonomously throughout the run. As a safety measure, it transmits positional information to the operator so they can take over manually, should the robot fail. Failures could include, but are not limited to, crashing into obstacles, generating incorrect paths to objectives, failing to find a valid path to an objective, jamming of any of the subsystems, or becoming otherwise incapacitated. In the event of any of these outcomes, the robot runs autonomous troubleshooting protocols. The driver will also be able to assume full control of some, or all, of the subsystems.

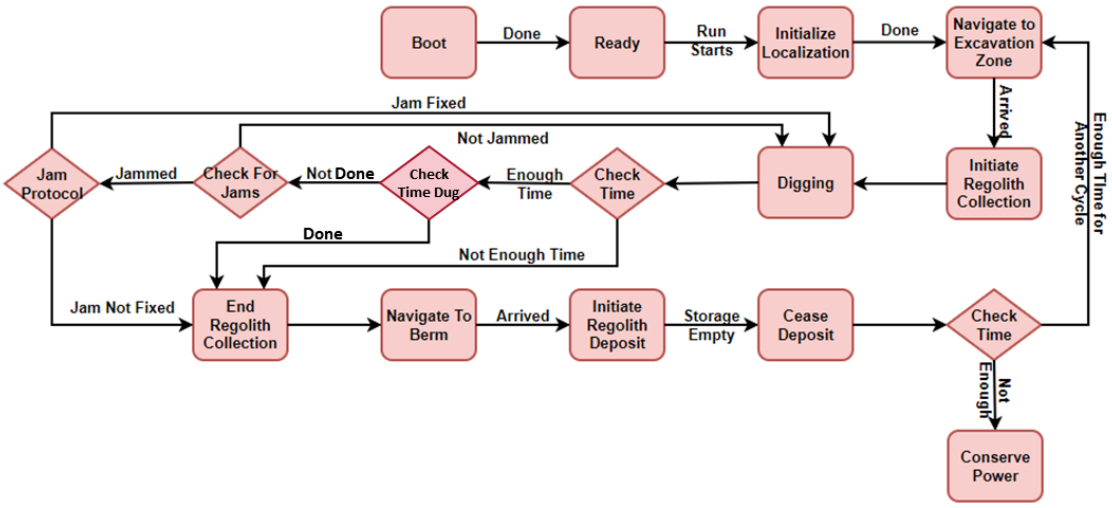

Fig. 4.1 Robot Concept of Operations.

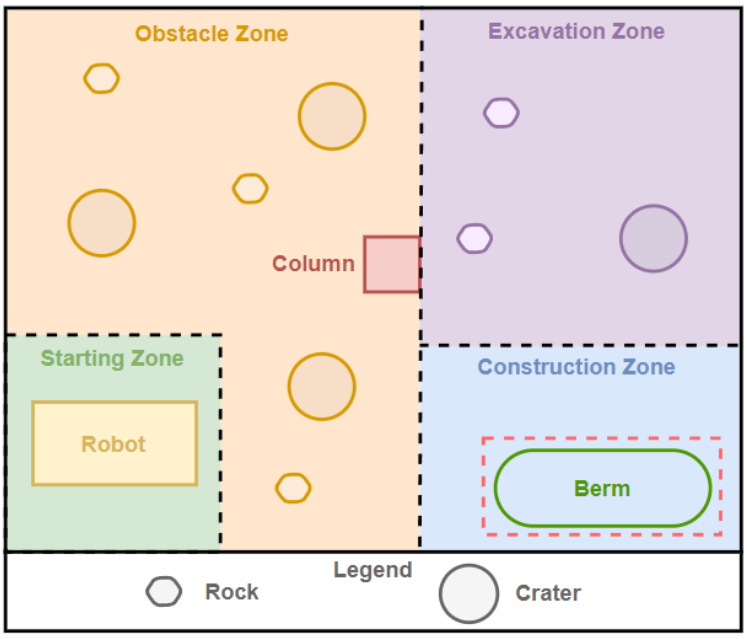

Fig. 4.2 Field Map.

4.2 Robot Layout

Fig. 4.3 details an approximate layout and packaging for the systems on the robot. The robot is much smaller than the NASA size regulations, so the shape of the robot can be more independent from the rectangular envelope. Fig. 4.4 and Fig. 4.5 show the robot assemblies.

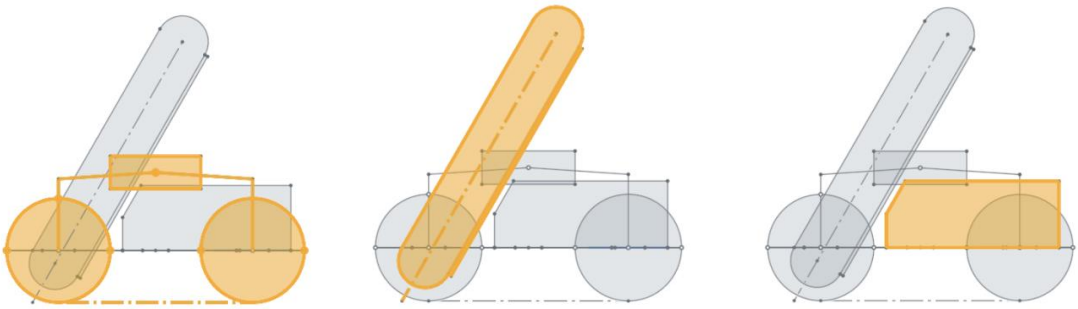

Fig. 4.3 Master sketches. Left: Drive Base. Center: Regolith Intake. Right: Storage.

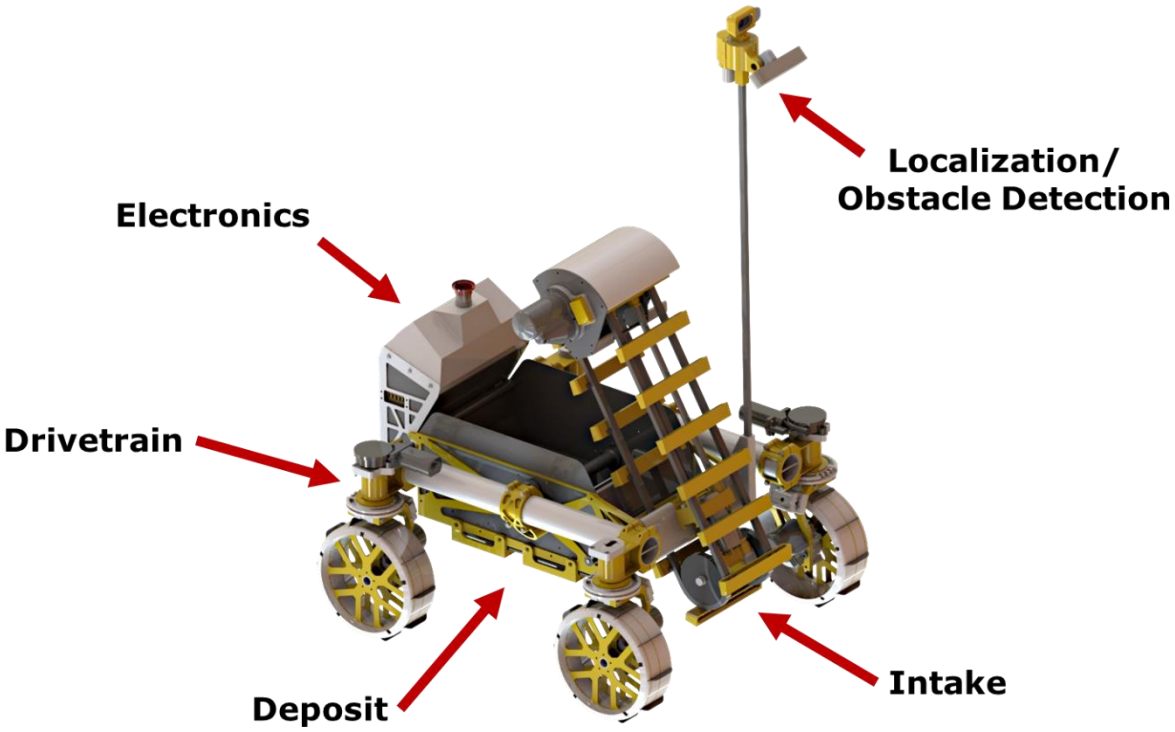

Fig. 4.4 Top Assembly.

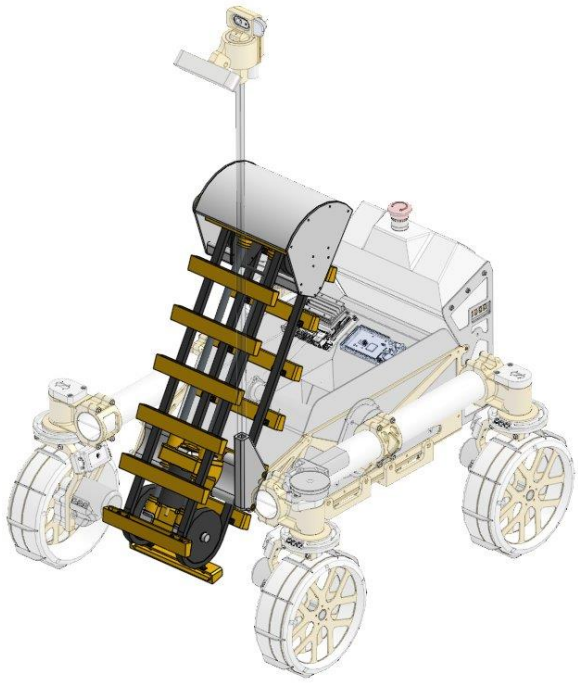

Intake

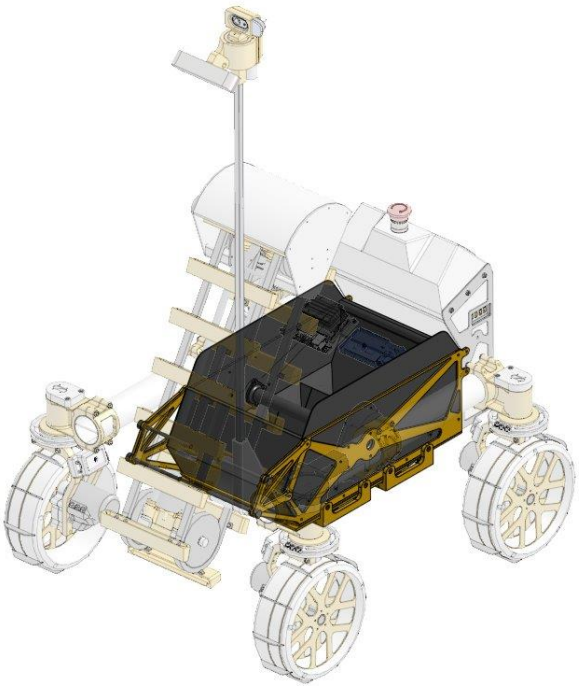

Storage/Deposit

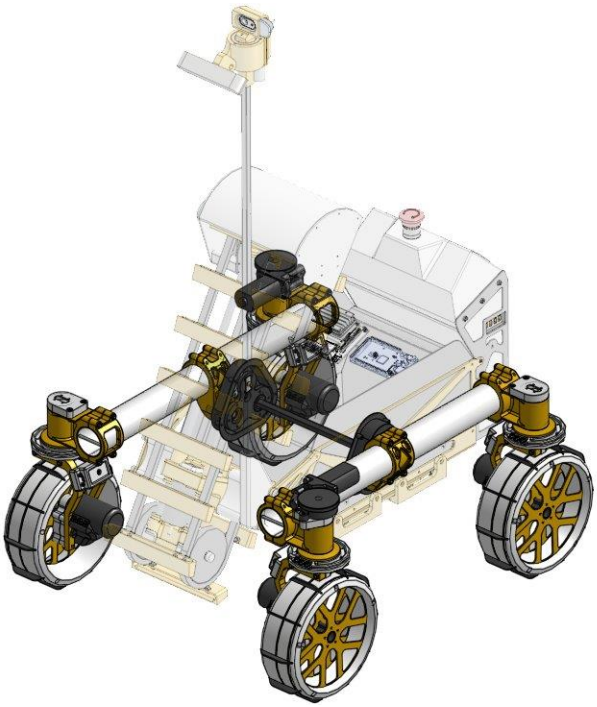

Drivetrain

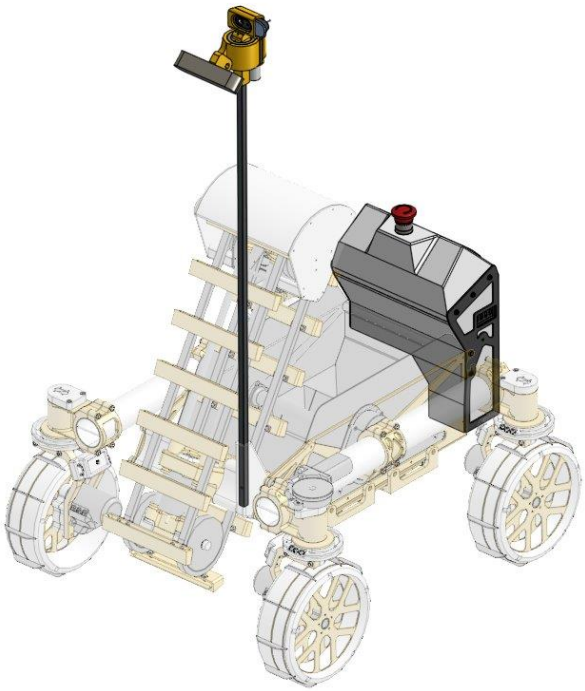

Electronics Package

Fig. 4.5 Isolated Subsystem Views.

4.3 Drive Base

The drive base subsystem is responsible for the locomotion of the rover. This is particularly difficult due to the uneven and shifting nature of the regolith simulant. To handle this challenge, the drive base was broken into four subsystems: chassis, drivetrain, ground interface, and suspension. The chassis encompasses the structure of the drive base and suspension, the drivetrain is responsible for the power transfer and steering, the ground interface provides buoyancy and traction in the regolith, and the suspension maintains four points of contact on the ground. Furthermore, as the lead time on the drive train parts was relatively high, we produced a prototype version of this system to aid software development while the final version was being manufactured.

4.3.1 Chassis

The robot's chassis is a major structural component of the robot, and therefore is a critical design component. The primary philosophy behind the chassis construction is to be as lightweight and stiff as possible. To achieve this end, we decided to use circular aluminum tubes for the primary structure, as they have a high strength-to-weight ratio. To attach components to these tubes, we elected to use a clamping design with dowel pins for indexing. This allows the robot to distribute force evenly on the surface of the tube while ensuring that everything is positioned correctly. The structure of the chassis is depicted in Fig. 4.6.

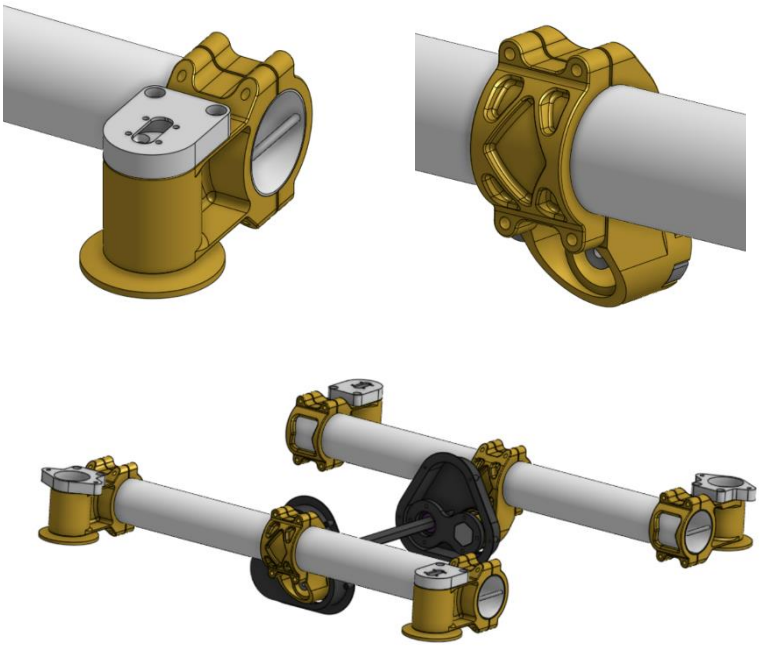

Fig. 4.6 Chassis Structure.

To keep the system as light as possible, we took several lightweighting measures. First, we calculated the thinnest possible walls for the tubes to be .03” while retaining a safety factor

of 10. The calculations for this are shown in Appendix B. Furthermore, every component of the suspension was lightweighted to further save mass.

4.3.2 Drivetrain

The design of the drivetrain is central to the success or failure of the robot. The drivetrain allows the robot to traverse and maneuver on the regolith and accomplish its objectives. After careful review of this year's challenge, we determined that our top drive base characteristics were maneuverability and mass. Complexity was also an important metric that we wanted to consider.

To determine which drivetrain was the best option for the robot, the team considered four different drivetrain styles: wheeled skid steering, treads, quadruplex swerve, and duplex swerve. We analyzed these drivetrain styles with respect to our priorities to determine which option was best. Our analysis is detailed in Table 4.1.

Tread drivetrains are heavy and energy inefficient but have low ground pressure on the regolith surface, meaning they sink less. We determined that a light robot is a key design feature, and treads are not conducive to that strategy due to their complex integration requirements. Additionally, light robots have fewer issues with sinking, negating the ground pressure advantage of treads. As a result, we determined that wheels were the correct choice for our robot's design strategy. While reviewing previous Lunabotics robots, we found that turning was difficult for most wheeled skid-steer drivetrains. While this was not a significant concern in previous years due to the linear rover paths required, maneuverability is important this year due to the obstacle zone. To limit wheel scrub, we opted to actuate the rotation of our wheel pods. While this does increase complexity and mass in comparison to a traditional skid-steer mechanism, it allows the rover to move efficiently with reduced risk of getting stuck.

The two actuated wheel pod designs we further investigated are the quadraplex and duplex swerve. Upon further investigation, we determined that translating diagonally, in reference to the rover's heading is not a major design requirement. Additionally, syncing four-wheel pods has proven to be a difficult task for past Lunabotics teams. While there are strategies to remedy this, it is simpler to have less degrees of freedom on the robot.

From this analysis, the team determined that duplex swerve was the best option, as it provided excellent turning, easy robot integration, and reduced actuation complexity in comparison to other drivetrain systems.

Table 4.1 Drivetrain Breakdown.

Drivetrain	Complexity	Mass	Maneuverability	Diagram
Skid Steering - Wheels	**Low** Simple construction methods required	**Low** 2-DOF system allows for lower mass budget	**Medium** Static wheel interface leads to functioning but not exceptional movement	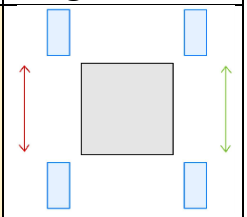
Skid Steering - Treads	**Medium** Simple concept but complex integration	**High** Heavy ground interface, both mounting and system itself	**Low** Minimized sinking, but turning efficiency is low due to excessive turning resistance	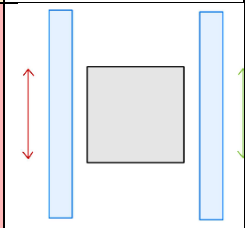
Quadruplex Swerve	**High** 8-DOF system but independently driven modules	**Medium** Simple mounting system but requires more actuators	**High** Independent wheel pods allow for very minimal scrub and sidling	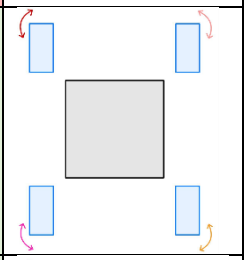
Duplex Swerve	**High** 6-DOF system but more complex mounting method	**High** The complex mounting system that ties the front-back modules together leads to a heavier system	**High** Duplex pods allow for very minimal scrub	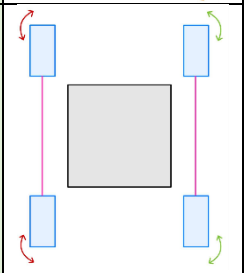

To construct the duplex swerve steering system, the team had three challenges: designing a bearing stack to take the weight of the robot, developing a mechanical link between the front and rear wheels, and determining how to turn the wheels.

The bearing stack went through two iterations. The first version of the stack used large angular contact bearings and a spider coupling to protect against potential damage. During the assembly of the prototype drivetrain however, we found that the bearings we had sourced were too large for this application, and that the spider coupling resulted in excessive play in the mechanism for minimal protection. As a result, the final iteration used significantly lighter thin-section ball bearings to support the wheel pods and eliminated the spider coupling in favor of a precision machined spline pattern. The initial and final designs of the bearing stack can be seen in Fig 4.7.

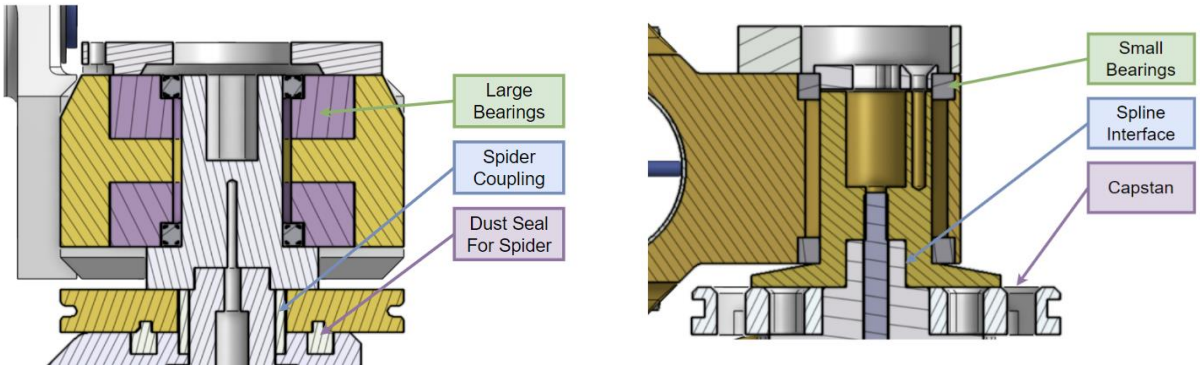

Fig. 4.7 Initial and final designs for the bearing stack.

For the mechanical link between the front and back wheels, we had three objectives: maintaining proper alignment between the wheels, the ability to turn 90 degrees in either direction, and high durability of the system. To meet these objectives, we had two suitable options: a linkage system and a cable-driven capstan system. The linkage system would be mechanically simpler and lighter but was unable to turn the necessary 90 degrees in either direction. As such, we selected a capstan system for wheel actuation. The risk of choosing the capstan system was that it was vulnerable to the pulleys slipping and losing tension over a run. To help counteract this, we designed our pulleys to have serrated bolts which dig into the cable, preventing slippage. Also, we installed turnbuckles on each cable to maintain tension. The final design for the pulleys is shown in Fig. 4.8.

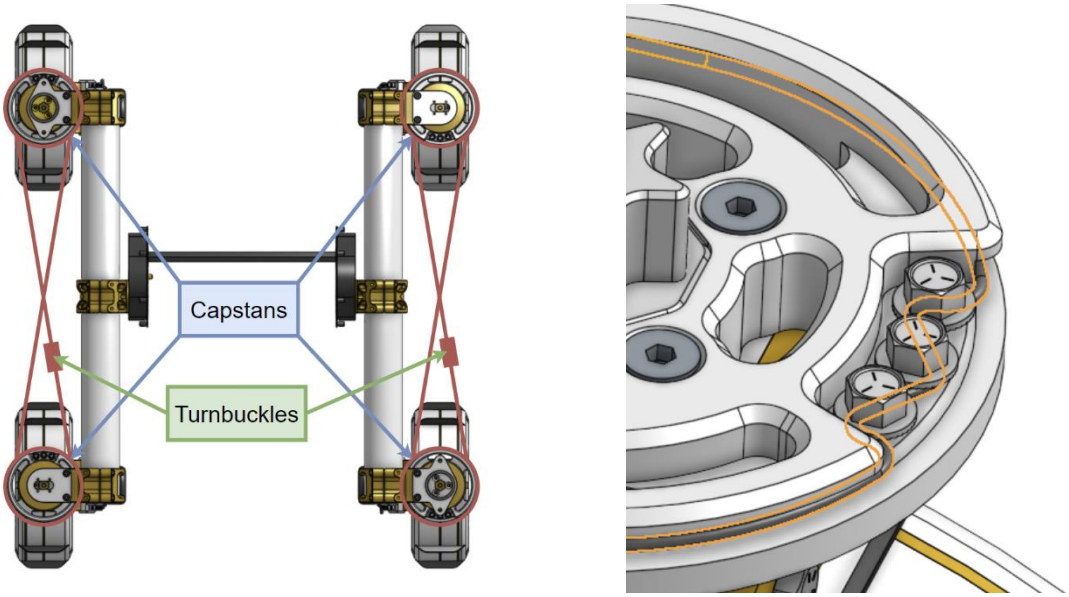

Fig. 4.8 Capstan steering system.

Next, we focused on the design of the steering power system. The power system must have enough torque to turn the wheels and cannot be backdrivable (this would cause the wheels to lose alignment). To this end, we decided that a worm drive would be an excellent option, as it offered a low-mass system with a high reduction. In our search, we found that a snowblower motor had all the qualities we desired, being a worm drive and packaged in a small form factor.

Furthermore, these motors have built in safeguards to protect from overheating, as well as a preferable mass output speed.

4.3.3 Ground Interface

When determining the construction of the wheels, the team first identified several standard features for every wheel design. Firstly, the wheels needed to have grousers, as a smooth wheel would not have sufficient traction. Secondly, the wheels required chamfered exterior edges to reduce turning resistance. Finally, the wheels would need to be able to reject the buildup of regolith internally.

For the main structure of the wheel, the team considered five different methods of construction: a plate stack, a single aluminum billet, a composite layup, fully 3D printed, and a spoked construction. Each concept has an example model to explore the differences between the designs. The team also compared the estimated masses and durability, as well as any additional pros and cons. As we were comparing just the structures of each design, grousers and dust rejection were not included in the 3D models. The conclusions of this investigation are detailed in Table 4.2.

Table 4.2 Wheel Designs.

Wheel Type	Mass/ Wheel	Durability	Additional Pros and Cons	Image
Plate Stack	~1.2 lb. + hardware + dust rejection + grousers	High	• Solved problem already done by most Lunabotics teams	
Aluminum Billet	~.9 lb. + dust rejection + grousers	Exceptionally high	• Difficult to make, possibly needing to be outsourced • Expensive • Allows for grousers to be integrated into part, making them lighter	
Composite Layup	~.6 lb. + dust rejection + grousers	Medium	• Difficult and potentially hazardous to make • Risk of delamination	
3D Printed Polymer	~1 lb. + grousers	Low	• Highest risk of breaking and wearing over time • Allows for rapid prototyping • Allows for integrated dust rejection	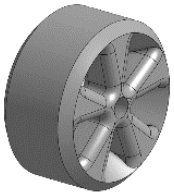

Spokes	~.9 lb. + hardware + dust rejection + grousers	Medium	• Maintaining spoke tension and roundness could be a challenge • Assembly is a difficult and highly involved process	

Using this information, the team determined that a combination of a composite plate stack and 3D printing would result in a strong and light wheel while still being easy to manufacture. A wheel design was made to these specifications, as depicted in Fig. 4.9. To verify the integrity of the wheels, we constructed a sample wheel. We placed this wheel into a bucket of regolith and loaded it with three times the expected weight to prove that it could maintain its structure without sinking. This test is depicted in Fig. 4.10. From this test, we determined that we could print wheel sections light, resulting in a wheel that weighed less than 500 g (~1.1 lb).

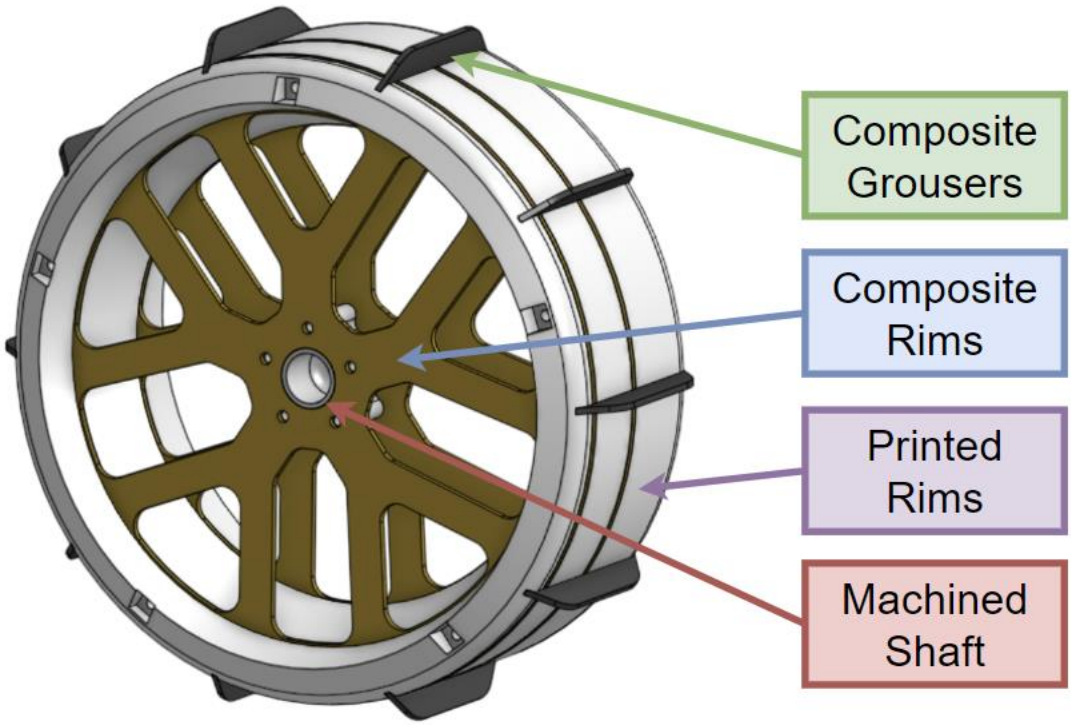

Fig. 4.9 Final wheel design.

Fig. 4.10 Wheel structure/sinkage test.

To specify a motor and gearbox to drive each wheel, we first measured the depth that the test wheel sunk into the regolith from the stress test. We used this value to approximate the rolling resistance in the regolith—represented as a slope with angle theta that the wheel would be driving up. This is shown in Fig. 4.11.

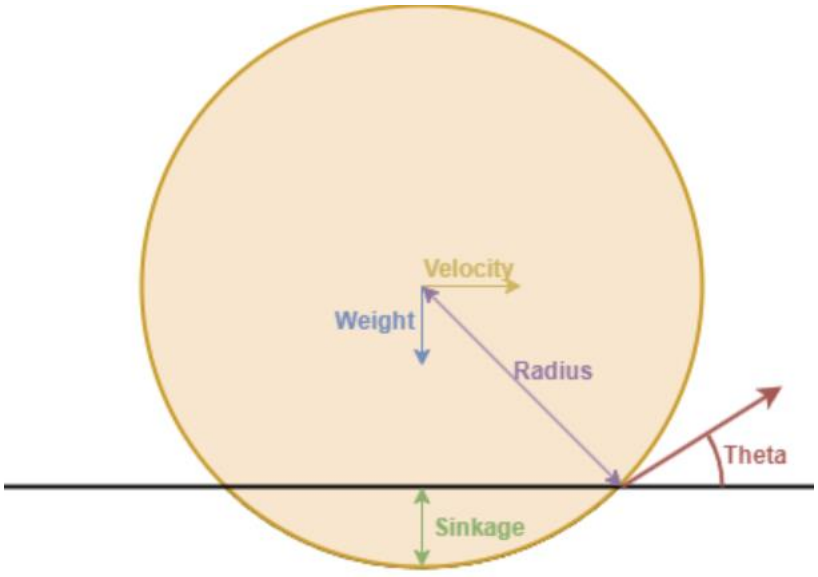

Fig. 4.11 Wheel Sinkage Diagram.

From this model, we could use the expected mass of the robot to determine the required torque of each motor. This calculation is shown in Table 4.3.

Table 4.3 Wheel Resistance.

Variable	Value	Units
Wheel Radius	4.00	in
	0.10	m
Sinkage	0.38	in
	0.01	m
Theta	25.01	deg
Mass on wheel	10.00	kg
Weight on wheel	98.10	N
Resistance Force	41.47	N
Output torque	4.21	Nm

From this calculation, we found two suitable motors, a DJI M3508 and a BAG motor. For both motors, we calculated the necessary reductions to reach the specified torque with a safety factor of four, allowing the motor to output more power if additional resistance was encountered. This calculation is shown in Table 4.4. Furthermore, using the calculated ratios, we performed a cost and mass analysis on the two systems. This analysis is shown in Table 4.5.

Table 4.4 Drive Motor Calculations.

DJI M3508 motor + gearbox			BAG motor		
Stall Torque	5.00	Nm	Stall Torque	0.40	Nm
Free speed	482	rpm	Free speed	13180	rpm
	50.48	rad/sec		1380.21	rad/sec
Safety factor	4.00		Safety factor	4.00	
Safe Input Torque	1.25	Nm	Safe Input Torque	0.10	Nm
	450	rpm		9885	rpm
Input speed loaded	47.12	rad/sec	Input speed loaded	1035.16	rad/sec
Ratio	3.37	:1	Ratio	42.13	:1
Output speed	133.5	rpm	Output speed	234.6	rpm
	13.98	rad/sec		24.57	rad/sec
Max speed	4.66	f/s	Max speed	8.19	f/s
Output power	58.91	W	Output power	103.52	W

Table 4.5 Cost and Weight Estimations.

Cost (per unit)					
DJI M3508 Motor & Gearbox			BAG Motor & Versaplanetary		
Motor	$100	DJI	Motor	$30	VEX
ESC	$80	DJI	ESC	$90	VEX
Gearbox	$45	Amazon/SCS	Versaplanetary	$85	VEX
Encoder	$25	AD	Encoder	$25	AD
			180 deg	$65	VEX
Total	$250		Total	$295	

Preliminary Mass Estimates (g per unit)			
DJI M3508 motor & Gearbox		BAG motor & Versaplanetary	
Motor	365 g	Motor	320 g
ESC	35 g	ESC	117 g
Gearbox	240 g	Gearbox	335 g
		180 deg	150 g
Total	640 g	Total	922 g

We chose the DJI M3508 gearmotor as our drive motor, as it performed better in all metrics that we measured. Next, we designed a custom gearbox for this motor with the necessary external reduction. The design consists of two custom machined plates that seal against each other to prevent dust ingress and a custom machined shaft to interface with the wheel's composite plates. This design is shown in Fig. 4.12.

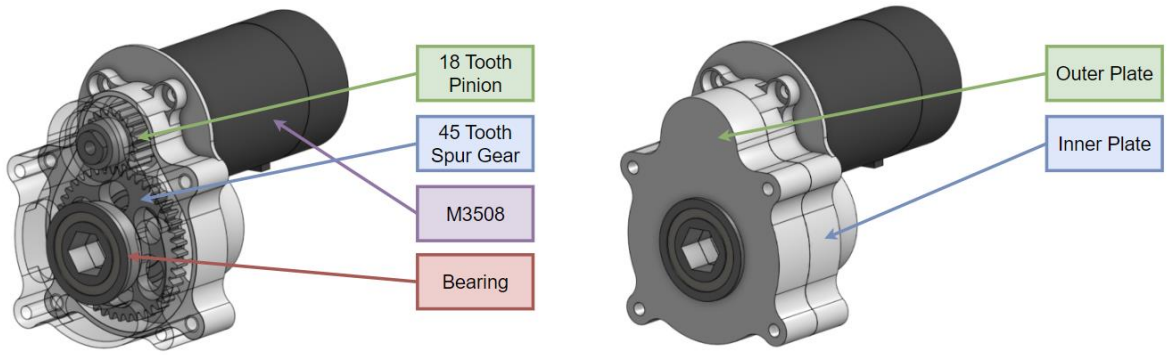

Fig. 4.12 Drive Gearbox.

4.3.4 Suspension

As the wheels are only designed to each move one quarter of the robot's mass, losing ground contact on any wheel could risk the robot getting stuck. As such, the robot utilizes a rocker-style suspension system. This allows the robot to maintain four points of contact to the regolith surface while driving. Unlike the previous team's cable design (as shown by the 2022 Lunabotics Team) [4], the robot employs a central differential shaft. This system was chosen as it integrates better with the central deposit mechanism. Rotation is transferred from the rocker to

the shaft through gears. The direction of rotation is inverted on one side using an idler gear, whereas no idler gear is present on the other side. This geartrain allows for the proper rocker-style suspension movement while integrating cleanly with the rest of the subsystems. The rocker suspension is shown in Fig. 4.13. On each side of the chassis, a hard stop limits this rotation.

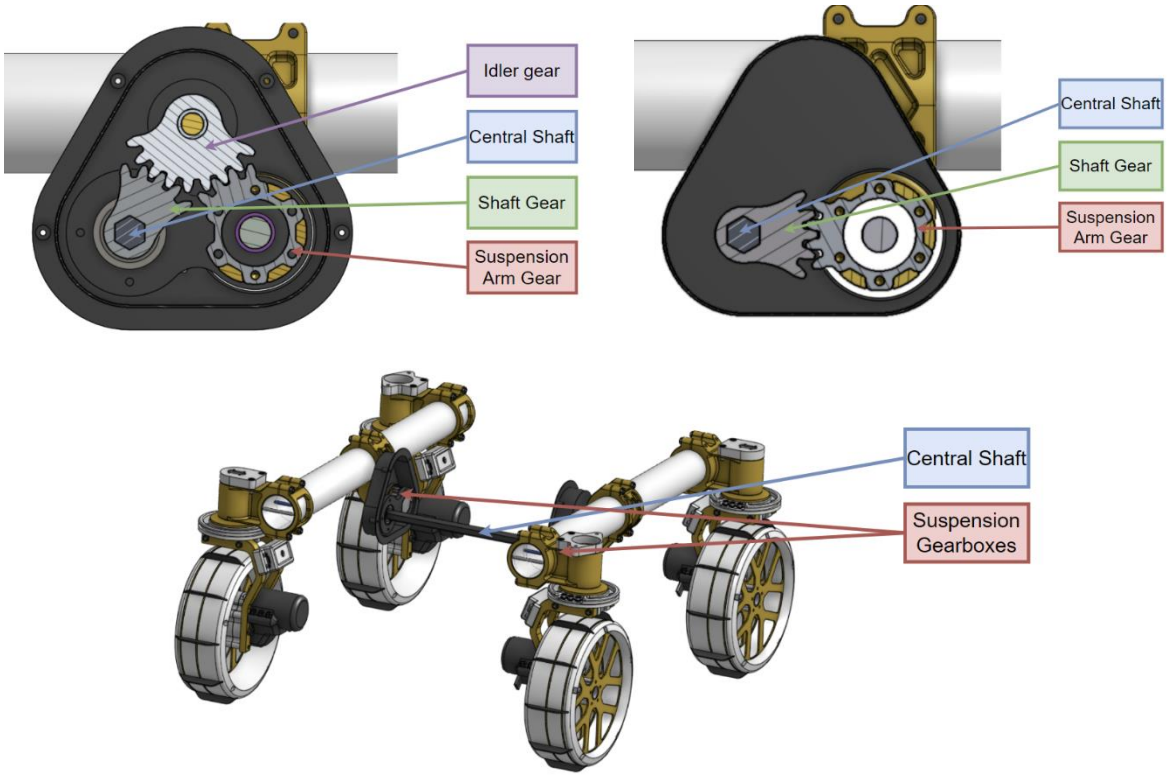

Fig. 4.13 Geared Rocker Suspension.

4.3.5 Prototype

Due to the drivetrain containing many custom manufactured parts, the team determined it was necessary to construct a prototype drivetrain for initial software development. This prototype is identical in proportion to the actual design but entirely 3D printed for rapid production. Furthermore, we replaced the wheels of the prototype with grouser-less thermoplastic polyurethane (TPU) wheels. These wheels permit testing on hard surfaces without damage. Creating this drivetrain allowed for electronics, software, and hardware to be worked on in parallel. The prototype drivetrain is shown in Fig. 4.14.

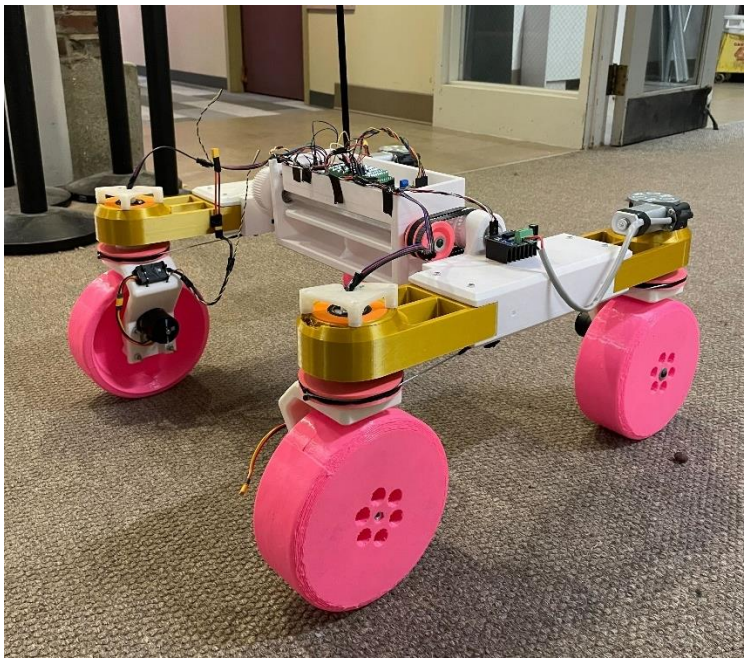

Fig. 4.14 Prototype Drivetrain.

4.4 Regolith Management

The rover's goal is to ultimately excavate regolith simulant from the excavation zone and deliver it into the berm construction zone. The high-level operation of the robot can be found in Section 4.1.

The team performed an analysis on the berm construction zone to determine the archetype of the regolith deposition mechanism. An approximate efficiency of deposited regolith helped to determine if simply dumping the regolith in the center of the berm zone will result in lost regolith. The analyses shown in Fig. 4.15 and 4.16 show this efficiency as a ratio of deposited regolith to the amount dumped. The berm construction zone analysis assumes that the regolith is poured along the centerline of the berm zone. We determined the maximum amount of dumped regolith using an estimated 30° angle of repose. Angle of repose is a characteristic related to the friction between the regolith particles that describes how effectively the regolith can pile up upon itself.

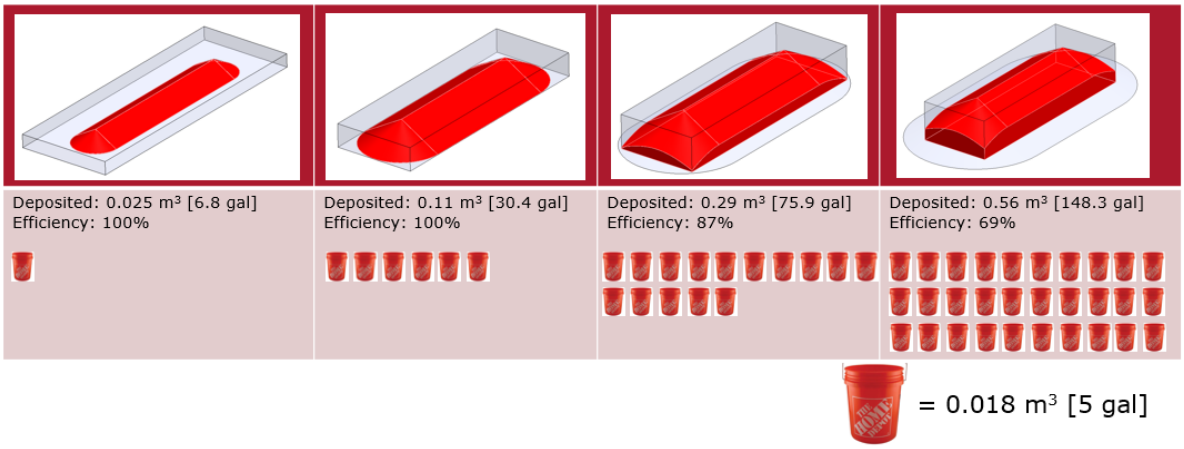

Fig. 4.15 Berm construction zone analysis. Adapted from [10].

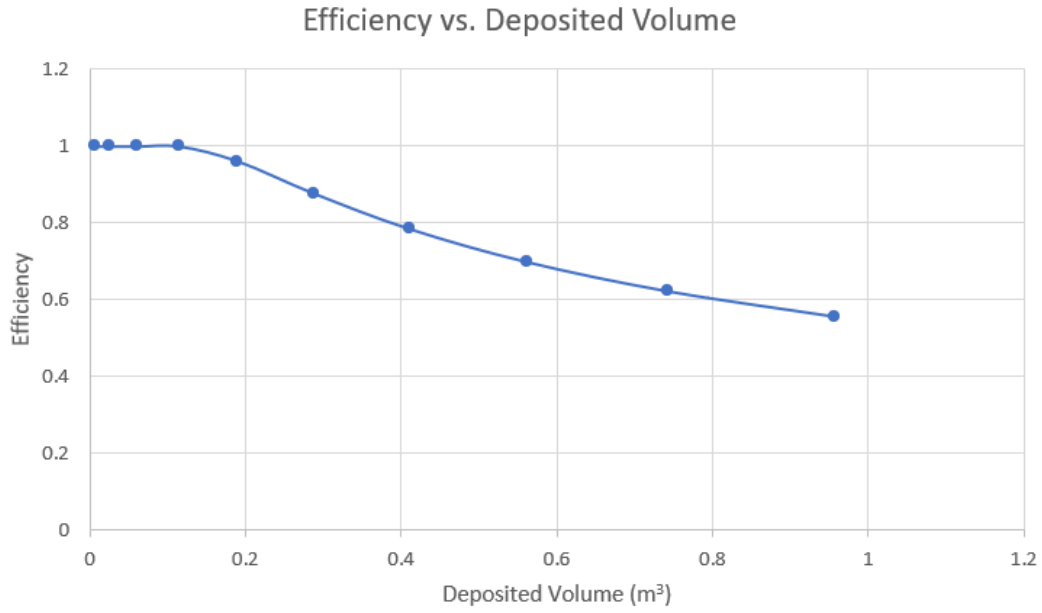

Fig. 4.16 Regolith efficiency declines as more volume is deposited.

The team determined that dumping the regolith in the center of the construction zone does not result in large losses of regolith at low volumes. To meet the goals defined by the Statement of Work, a simple dumping mechanism will be sufficient.

A simple dumping mechanism creates regolith pile(s) that do not need to span the length of the berm zone. Fig. 4.17 shows how much space these piles will take up in the berm zone. The following sections will discuss each regolith management subsystem.

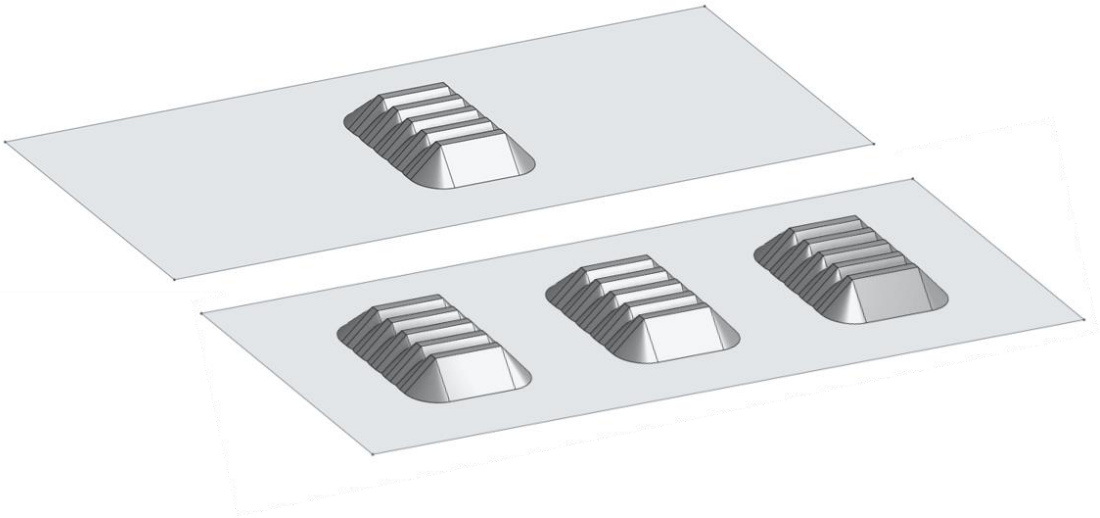

Fig. 4.17 Regolith pile(s) in the berm zone for minimum and reach goals.

4.4.1 Intake

As stated by [3], the excavation zone is roughly 3 m long by 3 m wide with rocks and craters randomly scattered around. Unlike the obstacle zone, in the excavation zone the robot can push rocks aside and can navigate through craters without penalty. The rules also disallow far-reaching or projectile mechanisms, meaning regolith intake and regolith delivery must be two separate and independent actions.

The top priorities for this excavation mechanism are reliability/consistency, mass, and navigation simplicity. During brainstorming sessions, the team drew inspiration from robust construction machines that primarily remove and transport ground particulates. Digging mechanisms are simply differentiated into three archetypes based on their inherent strategy. This strategy can be seen in Table 4.6, with examples shown in Fig. 4.18-4.20.

Table 4.6 Excavation Strategy Layout.

Excavation Strategies		
Type 1	*Type 2*	*Type 3*
• Deep digger • Cannot translate during excavation Examples: Vertical Auger (Fig. 4.7)	• Deep digger • Can translate during excavation Examples: Archimedes Screw, Conveyer Belt (Fig. 4.8)	• Shallow digger • Must translate during excavation Examples: Roomba, Golf Ball Rake (Fig. 4.9)

Fig. 4.18 Type 1 Excavators. [11].

Fig. 4.19 Type 2 Excavators. [12], [13].

Fig. 4.20 Type 3 Excavators. [14], [15].

The team analyzed these 3 excavation types by the top priorities. This analysis is shown in Table 4.7.

Table 4.7 Excavation Type Breakdown.

Excavation Type	Reliability/Consistency	Mass	Navigation Simplicity
Type 1	**Medium** 2-DOF	**High** Large mechanism to dig deep	**Low Complexity** Only needs to navigate to desired excavation spot
Type 2	**Medium** 3-DOF	**High** Large mechanism to dig deep	**Medium Complexity** Navigates to desired excavation spot with sufficient space in front for translation
Type 3	**High** 1-DOF	**Low** Small mechanism for shallow digging	**High Complexity** Requires high situational awareness to dig and navigate around obstacles

Although Type 3 excavators have the highest reliability and lowest mass, they are more complex because of the increased level of situational awareness and maneuverability required. Type 1 and Type 2 excavators have comparatively short and discrete digging paths, which is better for autonomous or teleoperated navigation. Further rate/capacity analysis helped determine if Type 1 and Type 2 excavators would be capable of accomplishing our minimum and reach goals. Appendix A shows this analysis.

A robot with an estimated dry mass of 20 kg can excavate up to 18 kg per deposit cycle and store up to 0.0133 m^3 of regolith. To hit the minimum goal of 0.01 m^3 of berm volume, the rover would need to complete one deposit cycle. To hit the reach goal of 0.03 m^3 of berm volume, the robot would need to complete three deposit cycles. Based on these initial system requirements, we were able to quantify mechanism performance based on various sizing parameters.

A vertical auger mechanism needs a diameter of roughly 20 cm [~8 in] to excavate the required 0.01 m^3 of regolith in one digging cycle. Vertical augers with diameters less than 20 cm [~8 in] would need to complete multiple digging cycles, which involves additional time for finding a new excavation site, navigation, and mechanism setup/retraction. These calculations are for a mechanism that digs 0.4 m deep (Note: the max depth of the arena is 0.45 m). A reduced digging depth would require an unreasonably large auger diameter. An increased digging depth also brings up challenges: high external loading from compacted regolith, large/heavy mechanism required to reach such depth, and increased likelihood of jamming. Finally, large diameter augers present significant manufacturing difficulties and extra mass.

Both Type 2 excavator mechanisms performed similarly in their rate and capacity of regolith mining. Certain sizes of the mechanism do not require side-to-side translation. Type 2 excavators with a smaller size can translate if the excavated volume is not sufficient. Another consideration is digging depth versus translation distance. Large digging depths require a mechanism of higher mass and large translation distances impose increased operational complexity. Type 2 excavators must balance these two parameters to limit plunging loads and navigation complexity. The team selected a Type 2 excavator because of its benefits over Type 1 and Type 3 excavators.

The team decided on a conveyor excavating system to meet the robot's regolith intake requirements. Many successful regolith mining robots have used a conveyor excavator for their intake systems, and a conveyor can easily employ a Type 2 digging strategy. Fig. 4.21 shows the regolith intake system.

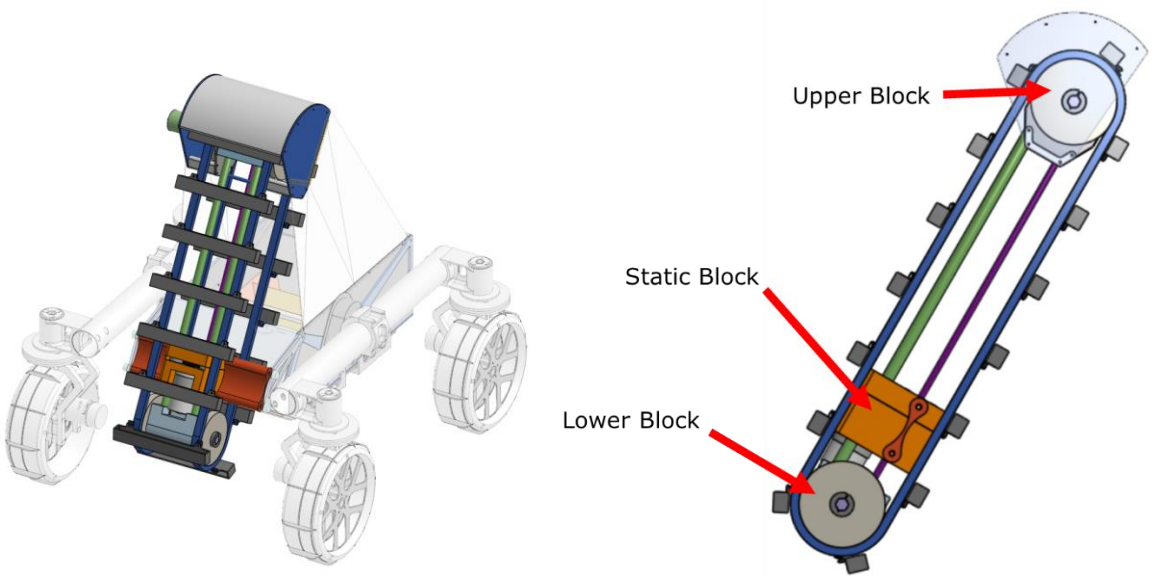

Fig. 4.21 Regolith Intake System.

The conveyor has a ground clearance of 4 in while stowed and is 25 in long (including the #35 chain and aluminum scoops). The low-profile scoops allow for limited loading on the scoops and the conveyor motor. A lead screw will actuate the conveyor beneath the surface of the regolith. The team chose a lead screw because of its compactness; a lead screw mechanism can fit entirely within the conveyor, keeping subsystem components together. Fig. 4.22 shows a section view of the linear actuation system.

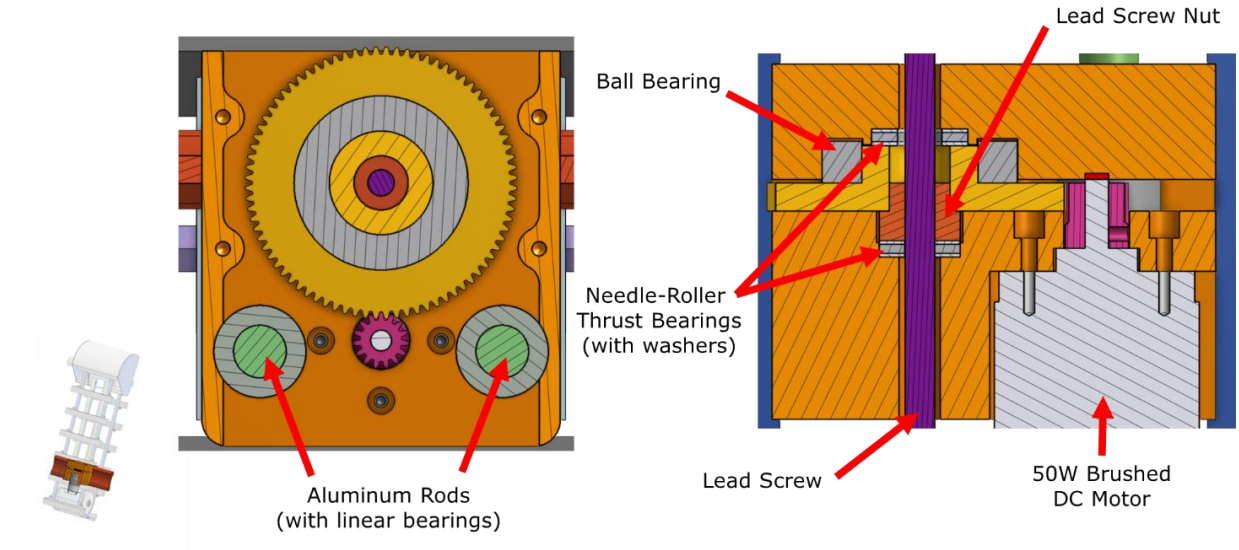

Fig. 4.22 Section Views of Linear Actuation System.

Two blocks hold the chain sprockets, in addition to fixing the lead screw and the structural aluminum rods. The lower block includes a chain-tensioning mechanism, allowing us to tension the chain after installing it around the sprockets. This is shown in Fig. 4.23.

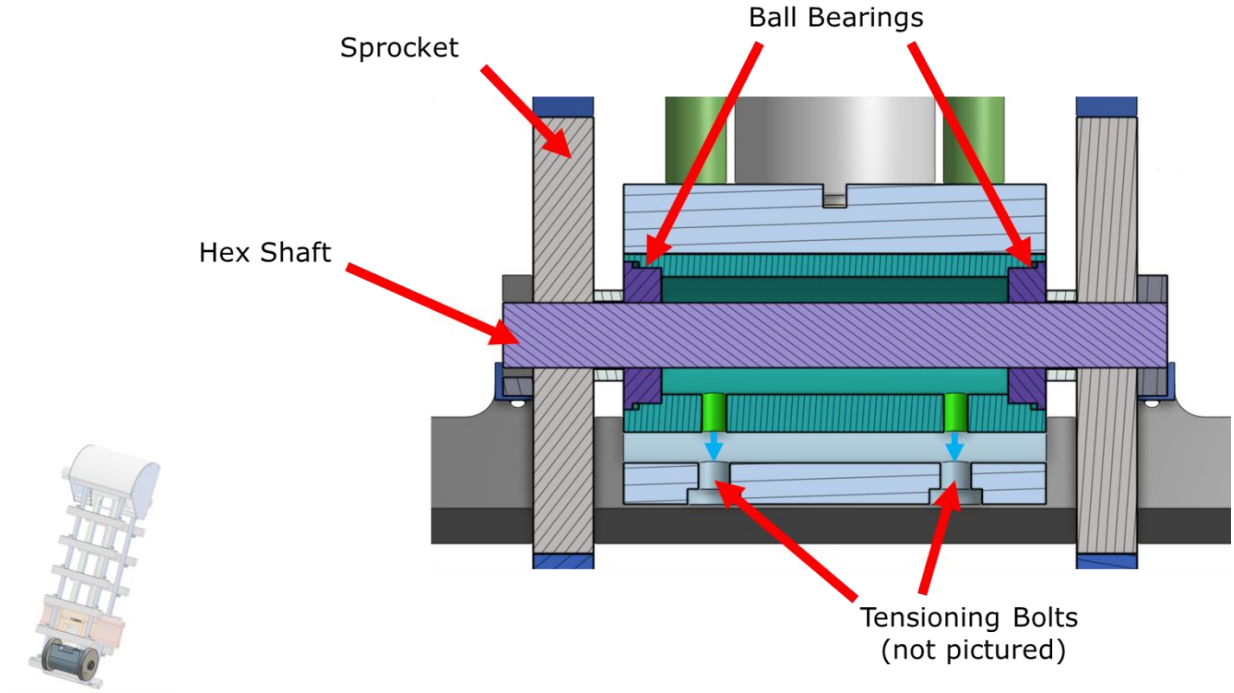

Fig. 4.23 Section View of Lower Block.

A DJI M3508 motor drives the conveyor. To theoretically determine the power requirements of the motor, the team considered the holding force of the conveyor (based on the mass of the chain, scoops, and regolith) as well as the force it takes to shear the regolith. We

determined the shear strength of regolith empirically, as discussed in Section 4.4.2. The time allotted for digging determines the plunging and translating speeds of the conveyor, which drive the scooping area of each bucket. This also helps us determine how fast the conveyor should rotate. This is shown in Fig. 4.24.

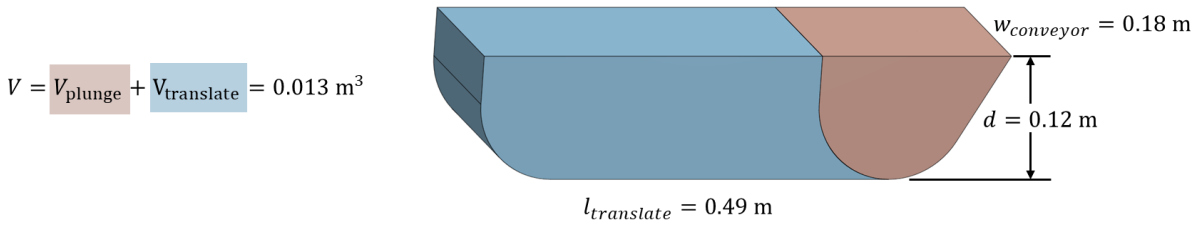

$d_{scoop\_plunge} = 0.14 \frac{cm}{scoop}$ $d_{scoop\_translate} = 0.084 \frac{cm}{scoop}$

$t_{plunge} = 11.6$ s $t_{translate} = 41.25$ s

$v_{plunge} = 1.2 \frac{cm}{s}$ $v_{translate} = 0.8 \frac{cm}{s}$

$\tau_{req} = (F_{holding} + F_{shear}) * r = 2.01$ Nm

$\omega_{req} = 150$ rpm

$P_{req} = 42.1$ W

Fig. 4.24 The plunging/translation volumes allow us to exceed our minimum regolith goal in one digging cycle.

Fig. 4.24 also shows the theoretical required torque of the conveyor: 2.01 Nm. Through testing of the system, the team determined a higher torque requirement of 4.7 Nm. This test is found in Section 5.2.1. Using this updated value and the required speed, the conveyor motor must meet a power requirement of 100.4 W. The DJI M3508 operating at a 3:1 reduction allows the conveyor to meet the required torques and speeds. The motor operates at ¼ stall torque, ¾ max power to ensure an increase in power would result in an increase in torque.

A 50W 12V DC motor drives a brass Acme nut around the steel lead screw. To determine the power requirements of the motor, the team considered a worst-case scenario of the lead screw freeing the robot by pivoting along the robot's back wheels. This calculation is shown in Fig. 4.25.

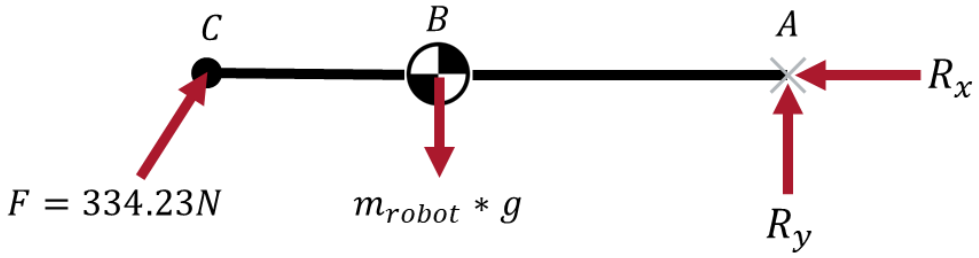

Fig. 4.25 The force required to pivot the robot on its back wheels drives the maximum load on the lead screw.

By treating the screw as an unwrapped incline plane, we can determine the required raising/lowering torques [16]. The time allotted for digging dictates the required plunging speed

of the conveyor, as shown in the conveyor calculations. Fig. 4.26 shows the calculation of the required torques, speed, and maximum power. We assumed the spur gear reduction would be 98% efficient, and the motor would operate at ¼ the stall torque.

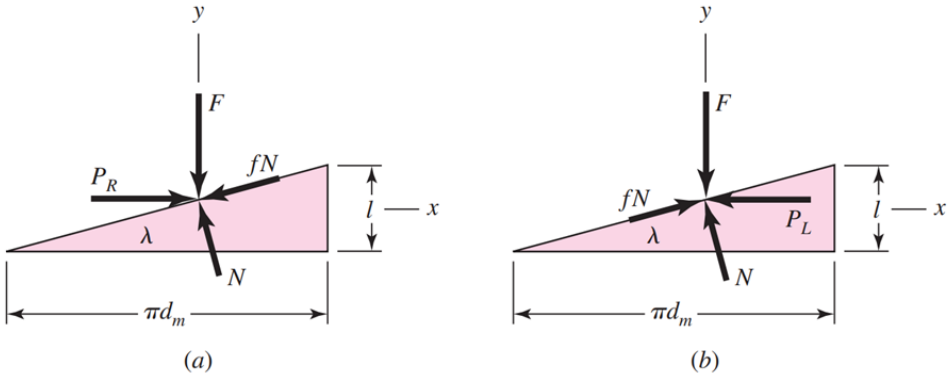

¼-20 Lead Screw:

$\tau_{raise} = 0.25$ Nm

$\tau_{lower} = 0.11$ Nm

$\eta = 0.27$

$v_{plunge} = 1.2 \frac{\text{cm}}{\text{s}}$

$\omega_{req} = 600$ rpm

$P_{req} = 21.57$ W

Fig. 4.26 Required Lead Screw Torque. View (a) shows the raising torque, View (b) shows the lowering torque. Adapted from [16].

Table 4.8 shows the motor selection for the conveyor and the lead screw.

Table 4.8 Motor Calculations for Intake.

	Conveyor		Lead Screw	
	DJI M3508		50W 12V DC Motor	
Required Max Power	100.4	W	21.57	W
Stall Torque	-	Nm	0.34	Nm
Free Speed	482.00	rpm	4500	rpm
Safety Factor	4.00		4.00	
Safe Input Torque	1.25	Nm	0.08	Nm
Input Speed Loaded	450	rpm	3375	rpm
Required Speed	150	rpm	600	rpm
Required Torque	4.7	Nm	0.25	Nm
Ratio	3	:1	5.33	:1
Actual Speed	150	rpm	633	rpm
Output Torque	14.1	Nm (from Dyno readings)	0.45	Nm

Bellows isolate the lead screw from regolith to prevent any jamming from particulates. To fit with the geometry of the system, we calculated that the bellows need extend up to 13 in and compress as small as two inches. Very few commercial options fit our size requirements, so we opted to fabricate our own. The bellows are made from clear vinyl sheets with seams melted to form a tube shape. The material is impermeable to dust, and both ends of the bellows are reliably sealed against the blocks. The bellows attach to each block via attachments shown in Fig 4.27.

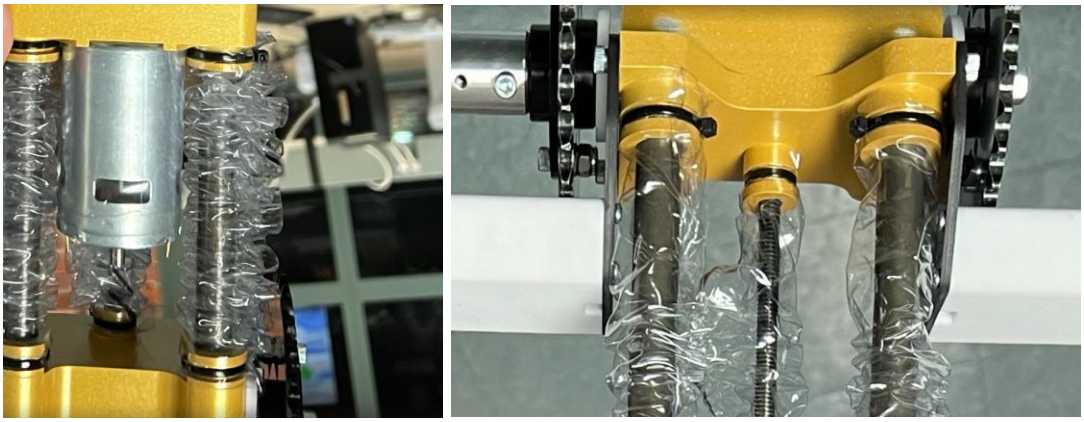

Fig. 4.27 Bellows attachments on Static and Upper blocks.

Testing of the intake system can be found in Section 5.2.1.

4.4.2 Storage and Deposit

The team determined the highest priorities for our regolith deposit system to be form factor, mass, reliability, and cycle time. The top priority for storage is its ability to interface with the intake, deposit systems, and drive base. Designs with good form factors have well integrated deposit and intake mechanisms and tightly packaged storage systems. Additionally, reliable mechanisms are unlikely to jam or malfunction during operation.

Once at the berm area, it is crucial to optimize the time required to deposit the regolith to complete a cycle within the 15-minute competition run. With these considerations in mind, the team brainstormed possible storage and deposition methods, drawing heavy inspiration from dump trucks and other industrial machines. Table 4.9 explores different possible mechanisms, against the most important characteristics identified by the team.

Table 4.9 Storage and Deposit Mechanism Breakdown

Type	Form Factor	Reliability	Cycle Time	Image
Conveyor Belt	**Compact** Takes up horizontal space	**Low** Grouser geometry is difficult to seal 1-DOF	**Long** Runs continuously until storage is depleted	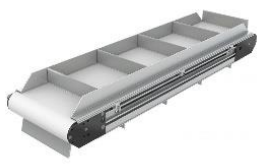

Sliding Grain Gate	**Moderate** Takes up vertical space	**Medium** Requires active preload to seal door 1-DOF	**Short** Opens door to instantaneously release regolith	
Dump Truck Without Door	**Not Compact** Takes up more horizontal and vertical space than other dump trucks	**High** No need to seal door 1-DOF	**Medium** Tips storage system further than other dump trucks	
Dump Truck: Electronically Actuated Door	**Moderate** Takes up both vertical and horizontal space	**Medium** Requires active preload to seal door 2-DOF	**Short** Tips entire storage system	
Dump Truck: Mechanically Linked Door	**Moderate** Takes up both vertical and horizontal space	**High** Weight of regolith seals door 1-DOF	**Short** Tips entire storage system	
Connect Four Trapdoor	**Compact** Storage structure does not entirely move so it takes up little space	**High** Low actuator travel and few moving parts 1-DOF	**Short** Releases all regolith instantaneously	

[17]-[22].

With a short cycle time and high reliability, the dump truck with a mechanically linked door appears to be a strong candidate. As the storage tips back, a sliding linkage simultaneously opens the door to release the regolith. The system's design also allows for the added weight of the collected regolith to increase the force working to seal the door, increasing its reliability without any additional power input. Along with the other dump truck methods, this mechanism requires a larger form factor compared to the conveyor belt. The entire storage system must tip past the regolith's angle of repose to deposit into the berm area.

Another mechanism to consider is the sliding grain gate. In this system, the storage consists of a vertical shaft with an angled bottom leading to the sliding door. The four-bar linkage used to open the door provides a quick cycle time since the door does not need to slide

far. However, this mechanism fails when it comes to reliability. The lunar regolith is extremely fine, much smaller than the grains typically used with this type of door. Therefore, the regolith will slip out of the bottom of the grain gate when the robot moves through the bumpy terrain. Additionally, the only force pushing the regolith out of the system is gravity, hindering its ability to reliably deposit its entire load.

The team also considered the addition of an agitator to the deposit system. The oscillating motion would decrease the cycle time of every system by actively pushing the regolith out, increasing its reliability to deposit the entire load. The dump truck mechanisms would also need to tip over less than they would need to without the agitator, giving them a smaller form factor. The downside of adding an agitator is the additional power consumption required and the increased complexity of adding another degree of freedom.

Lastly, the team investigated the option of using a Connect 4-inspired trapdoor mechanism placed at the bottom of the storage systems. This mechanism has a compact form factor, high reliability, and short cycle time. Unlike most other discussed mechanisms, this mechanism does not require the entire storage system to tip on its side, rather allowing for regolith to fall out when the trapdoor holes are opened. In addition, the power requirements for this mechanism are significantly lower than the other ideas. The actuator does not need to lift the weight of the filled storage structure and the short actuation distance allows for lower speeds to maintain equivalent deposit times. Like the sliding grain gate, this mechanism relies on gravity to push the regolith out, lowering its reliability. However, this structure has multiple openings for the regolith to exit, minimizing the effect of any clogs caused by friction forces between the regolith grains. For these reasons, the team decided that this mechanism is best suited for our robot architecture and requirements.

The main architecture of the deposit/storage systems (shown in Fig 4.28) consists of several main subcategories: bucket structure, actuator, conveyor mount, drivetrain mount, sliding mechanism, and the overhead fabric canopy.

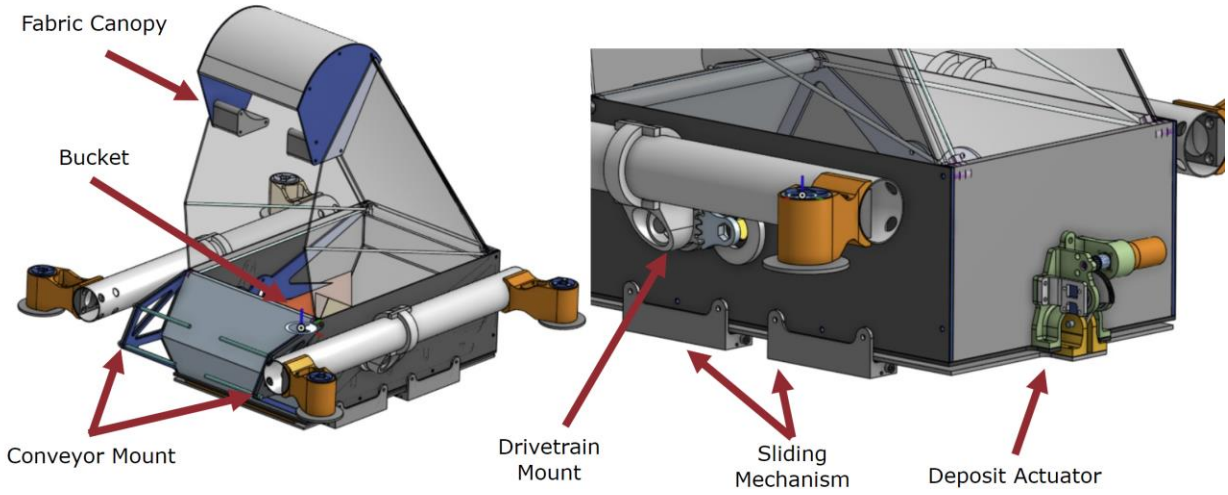

Fig. 4.28 Deposit/Storage System Architecture.

There is a sliding plate beneath the storage bucket connecting to the main bucket structure via the sliding mechanism. In the closed positions, this plate covers the holes in the bottom of the storage bucket. In the open position, these holes are uncovered. Fig. 4.29 shows a section view of the storage/deposit system.

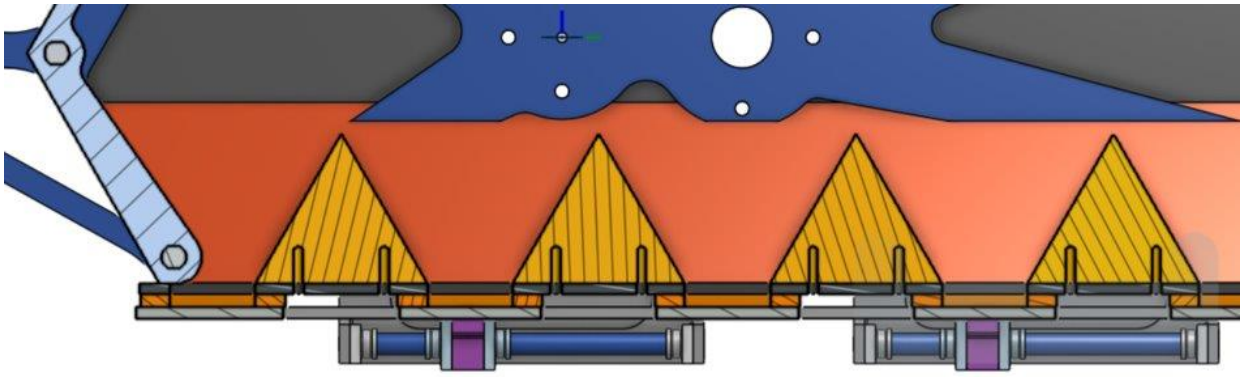

Fig. 4.29 Side Section View of Storage/Deposit.

The deposit sliding mechanism consists of a central bracket that mounts to the side of the storage structure and holds a round standoff. This standoff is the center axis of what the sliding mount (pictured in purple) rides along. The sliding mount has a pressed oil-impregnated brass bushing and connects to the bottom sliding plate. Like the intake system's lead screw, fabric bellows will isolate the standoffs from regolith. Another view of the deposit sliding mechanism is shown in Fig. 4.30.

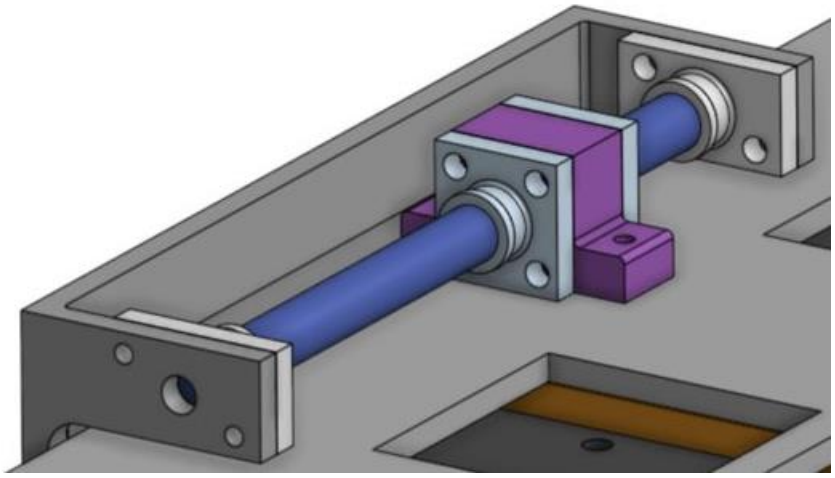

Fig. 4.30 Deposit Sliding Mechanism.

Due to the unique nature of our deposit mechanism, the team conducted a series of tests to validate that the concept is functional and to identify any flaws in the design prior to full scale construction. We conducted all our tests with both sand and regolith simulant to determine worst case scenarios. Firstly, we constructed a half-scale prototype (shown in Fig. 4.31) to validate that the brushes we chose were sufficient at isolating the bucket internals from

regolith/sand. In addition, we hoped to prove that all the regolith/sand would be able fall out of the storage bucket when we commanded the mechanism open.

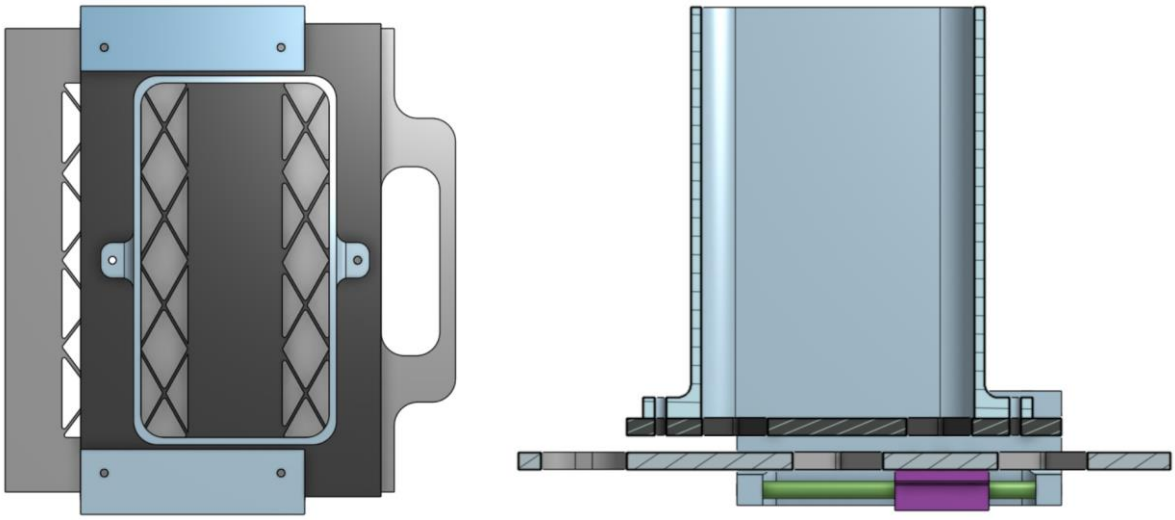

Fig. 4.31 Prototype of Half-Scale Desposit Mechainsm.

Our test results successfully fulfilled both our test objectives and we concluded that we could move forward with the full-scale design. The test is shown in Fig. 4.32.

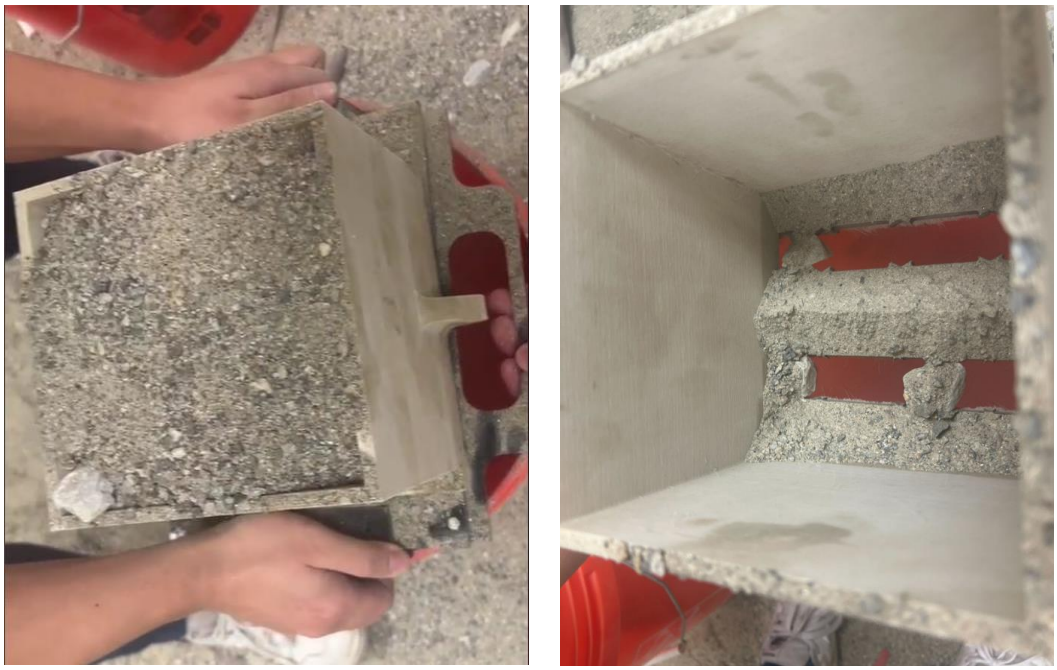

Fig. 4.32 Deposit Mechanism Prototype Test Results (Before and After).

Further testing included the characterization of the angle of repose of the regolith simulant (shown in Fig. 4.33). The angle of repose is the angle that the undisturbed particles hold with respect to the horizontal. This characterization will define the angles of the 3D-printed

ramps inside the storage. These ramps ensure that all particulates will fall out of the storage and leave a minimum amount of residual material.

Fig. 4.33 JSC-1 Regolith Simulant Angle of Repose Testing.

These test results showed that the JSC-1 regolith simulant has an angle of repose of approximately 45 degrees, compared to the angle of repose of 30-35 degrees for sand [23]. This means that we need to design to a worst-case angle of 45 degrees. Therefore, the ramp designs have an angle of 60 degrees to let the particulates fall out more reliably. These ramps are shown in Fig. 4.34.

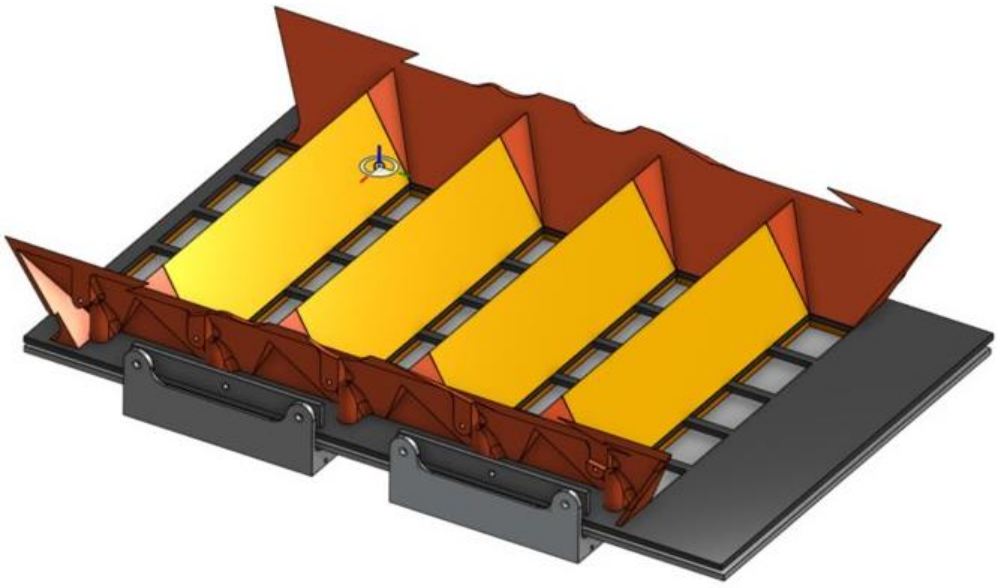

Fig. 4.34 Model of 3D-Printed Ramps.

The team discussed several methods of linear actuation for deposit mechanism including lead screw, COTS (commercial off-the-shelf) linear actuators, rack and pinions, and crank-slider mechanisms. We ultimately decided to move forward with a crank-slider derivative known as a yoke mechanism because of the downfalls of the other options. Lead screw actuation is

generally more prone to damage from FOD and have low-power efficiency. COTS linear actuators are enclosed versions of lead screws, but often have high costs. Lastly, a design study proved that the rack and pinion mechanism had a high part count and was not very dust tolerant. The yoke mechanism is shown in Fig. 4.35.

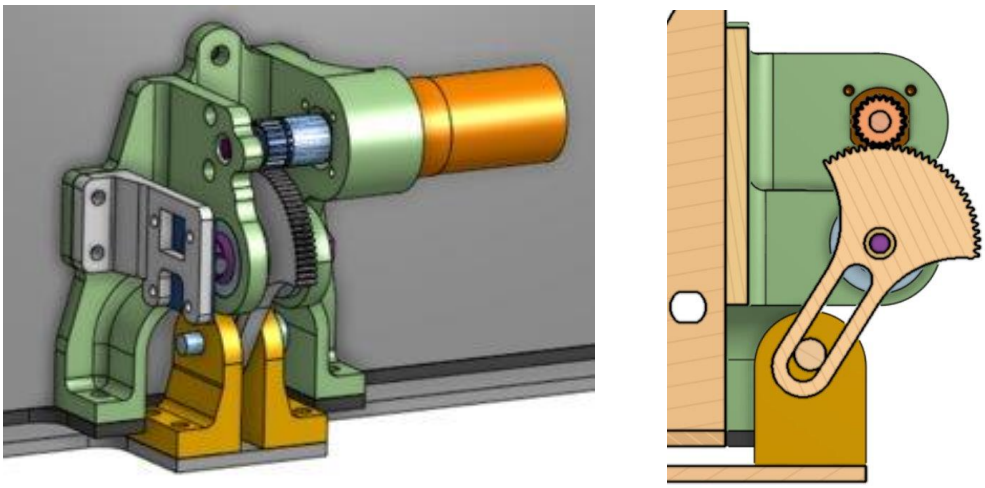

Fig. 4.35 Deposit Actuator.

Ultimately, we converged on a yoke mechanism driven by a DC brushed gear motor. It features a reduction on top of the gear motor of 4:1 to achieve the desired output speed and torque. The design also includes a rotary encoder that senses the absolute position of the output gear. To determine the torque requirements of the mechanism, we conducted a few trials of regolith/sand shear strength testing. These tests concluded that the JSC-1 and sand shear strength were 17.2 N/m^2 and 23.4 N/m^2 respectively. The test is shown in Fig. 4.36. Table 4.10 shows the motor calculations for the DC brushed motor.

Fig. 4.36 Regolith/Sand Shear Strength Testing.

Table 4.10 Motor Calculations for Deposit Mechanism.

Required Torque	0.91	Nm
Required RPM	25.57	rpm
Required Power	2.44	W
Stall Torque	0.93	Nm
Free Speed	142	rpm
Torque Safety Factor	4	
Safe Input Torque	0.23	Nm
Input Speed Loaded	106.5	rpm
Ratio	4	:1
Output Speed Loaded	26.63	rpm
Output Torque	0.93	Nm

Shown below in Fig. 4.37 is the aluminum frame structure (left) and the non-structural component additions (right). The storage bucket is the main structure of the robot. It holds all the collected regolith and reacts loads from the conveyor and drivetrain. Due to the high structural demands of this system, it is important that we can ensure that it is strong and stiff enough for the robot's needs. The non-structural members of this assembly include TPU 3D-printed front and back sides of the bucket. This compressibility allows us to easily preload the crossbars, making the structure a stiff composite sandwich.

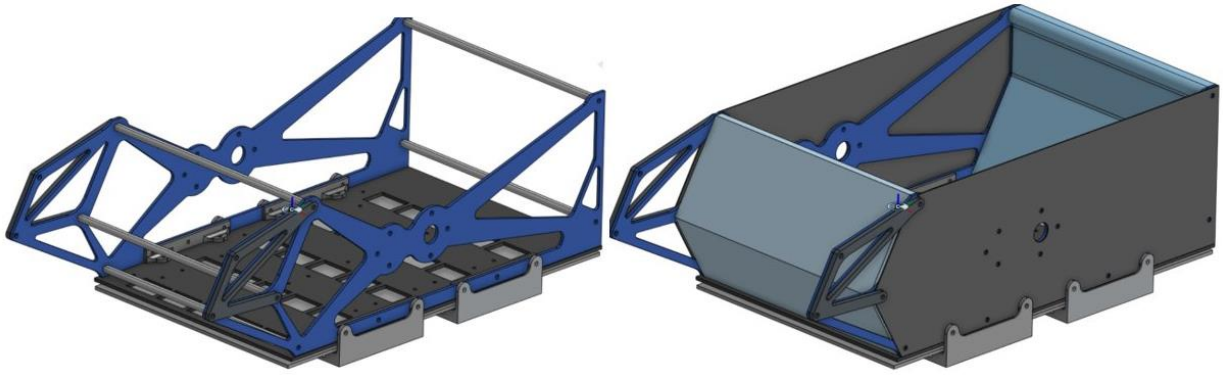

Fig. 4.37 Regolith Deposit Structure. Left: Structure. Right: Storage.

Using loads gathered from conveyor digging worst-case scenario and maximum payload weights, we were able to run finite element analysis on the aluminum structure and iterate upon the geometry until we achieve a structural safety factor of 5-10. Fig. 4.38 and 4.39 show this analysis.

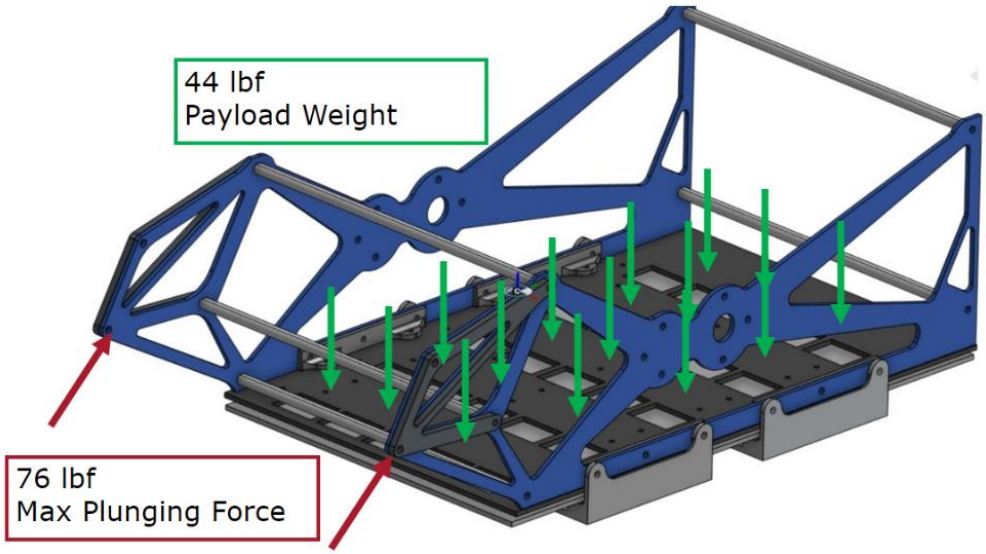

Fig. 4.38 Aluminum Structure Loads Summary.

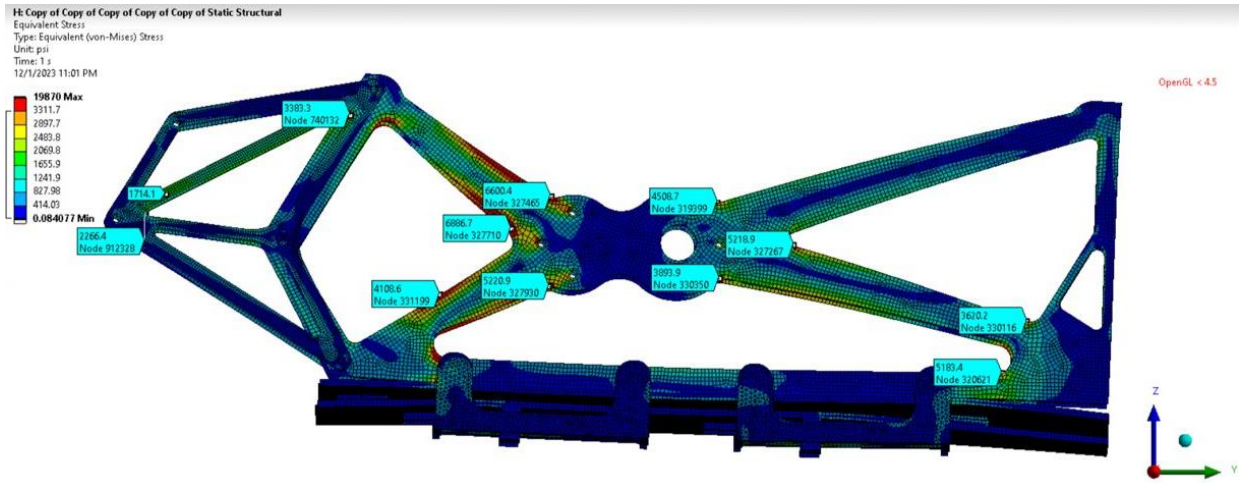

Fig. 4.39 Aluminum Structural Analysis Results.

Through the full structural model of the aluminum structure, we validated that the structure would have sufficient strength and stiffness in planar directions. However, under real loading conditions, lateral/through-plane loads are present. For this reason, we are stacking a 5mm G10 fiberglass plate on top of the conveyor mount (shown in Fig. 4.40).

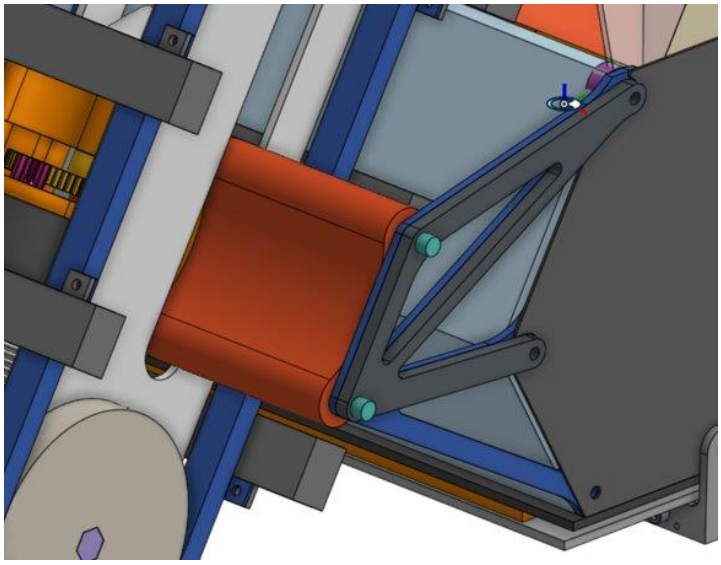

Fig. 4.40 Conveyor Attachment Point.

From studying previous Lunabotics robots, we noticed many conveyor-type intake systems would blindly throw regolith upwards, creating a cloud of aerosolized regolith around the robot. To ensure all the regolith collected from the intake goes into the storage, a fabric canopy (shown in Fig. 4.41) spans from the top of the storage bucket to the top of the conveyor, made from a thin, clear vinyl material. The vinyl is a non-woven fabric, and its transparent quality allows the regolith to be visible during operation. The canopy also increases the maximum volume of the storage system, giving the team more flexibility on what can be added inside the storage.

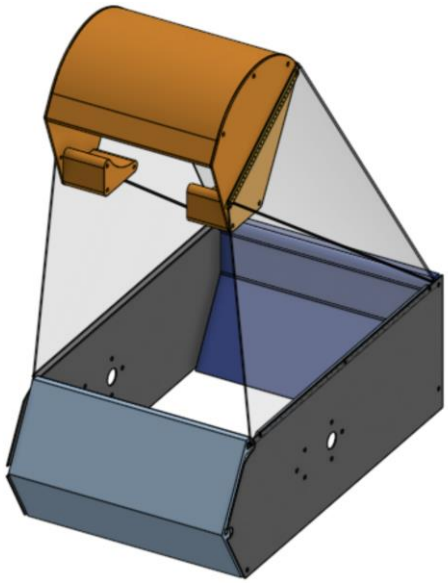

Fig. 4.41 Fabric Canopy.

Testing of the deposit and storage system can be found in Section 5.2.2.

4.5 Electronics

4.5.1 System Architecture

The electrical system of the robot can be divided into four subsystems: Power, Controllers, Actuators, and Peripherals, and is detailed in Fig. 4.42.

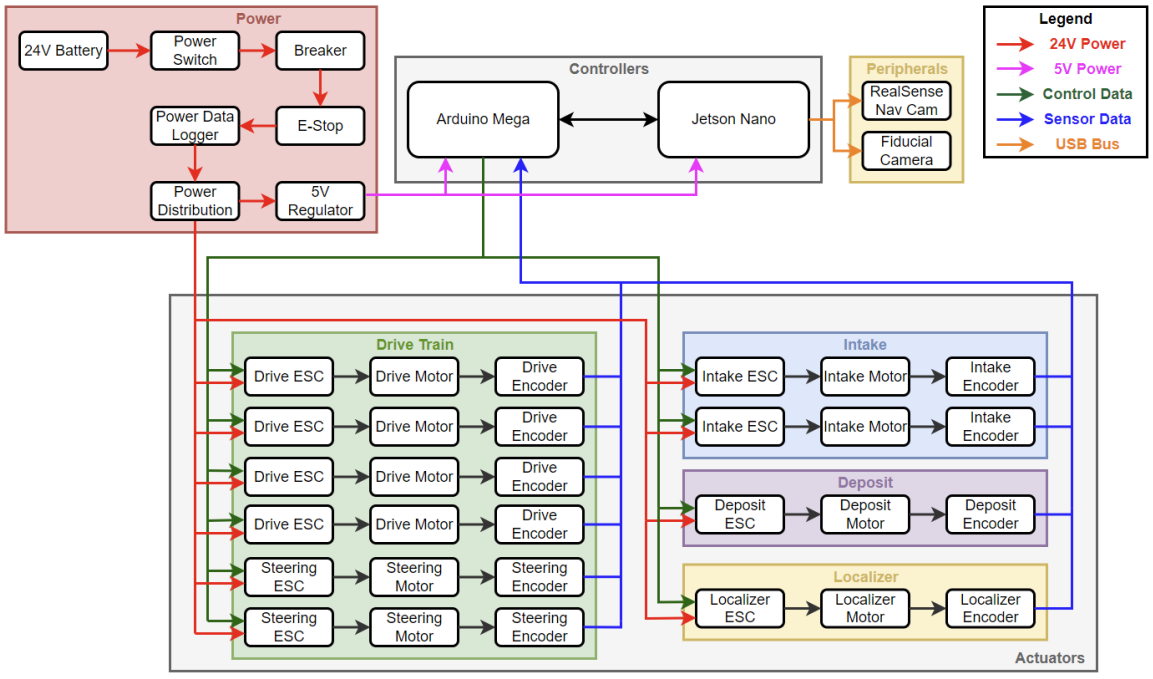

Fig. 4.42 Electronic System Architecture.

A 24V battery powers the robot for a full 30-minute competition run. This battery must be easily accessible for quick replacement. Power runs through a switch and a breaker, as well as through the emergency kill switch that NASA requires [3]. The team can safely access these components during a run. Additionally, NASA requirements require an inline COTS data logger to record power consumption. Power runs to the subsystems through a power distribution panel. Additionally, a 5V regulator is responsible for powering the microcontrollers.

A Jetson Nano and Arduino Mega control the robot. The Arduino handles low-level tasks, such as controlling subsystems, reading sensors, and tracking the position of the various subsystems. The Jetson handles high level tasks, such as image processing, localization, and navigation. The microcontrollers are connected to each other, and able to send and receive data.

Electronic speed controllers control the robot's actuators. The speed controllers are individually sized for each subsystem to use as little power as possible. They all receive the motor's nominal voltage through a step-down buck converter, as well as a control signal from the Arduino. For proprioception, every system implements Hall effect encoders, which send positional data back to the Arduino.

The robot's peripherals encompass all subsystems not included in the previous three categories. They are primarily responsible for sensing the environment, like the stereo vision camera for navigation, as well as the fiducial camera and its DC motor for field localization. They also include the sensor that is responsible for determining how full the storage system is. Additional sensors can be added if necessary for operation, but NASA regulations require them to be able to function in a lunar environment. There can be no sensors that make use of environmental conditions not present on the moon, such as a magnetometer or an ultrasonic range finder that requires an atmosphere.

4.5.2 Communications

Teams must establish wireless communication between their lunar mining robot and the mission control center during the competition. This communication is essential for transmitting commands to the robot and receiving telemetry data, video feeds, and sensor readings from the robot. Furthermore, teams must supply one or more laptop(s) or other device(s) for controlling the robot from within the mission control center, and a Wireless Access Point (WAP) for connecting the robot to the network in the field. Between the network switch and the WAP, NASA has a passive bandwidth utilization recording device to monitor bandwidth used by teams during their runs. We are minimizing the bandwidth we use to reduce the total points subtracted from our score at the end of the match.

4.6 Software

4.6.1 System Architecture

The software system architecture plays a pivotal role in the development of a NASA Lunabotics robot. It serves as the foundational framework that organizes how the robot interacts with its internal components and orchestrates the actions required to execute tasks within the robot's operational domain. By defining the software architecture, our team can plan how the robot will accomplish its assigned tasks, interact with external elements, and adapt to the unique challenges of lunar mining and construction.

The central focus of the robot's functionality lies in its mobility. Our chassis is capable of effectively navigating the simulated lunar terrain before, during, and after regolith collection. To achieve this mobility, our software implements two approaches: teleoperation and autonomous navigation. Teleoperation is controlled via a human operator, utilizing the camera feed provided by NASA to navigate the terrain. Conversely, autonomous navigation allows the robot to independently find paths and maneuver through the terrain.

In the architecture of the teleoperated control system, the design consists of communication between the drive motors and a controller or keyboard. These commands give the robot operator full control of some or all the subsystems.

For autonomous operation, the robot makes use of multiple methods of navigation. It will use fiducials to determine its general position on the field, and a version of simultaneous localization and mapping (SLAM) to navigate around obstacles. Fig. 4.43 demonstrates how the software implements the autonomous navigation task.

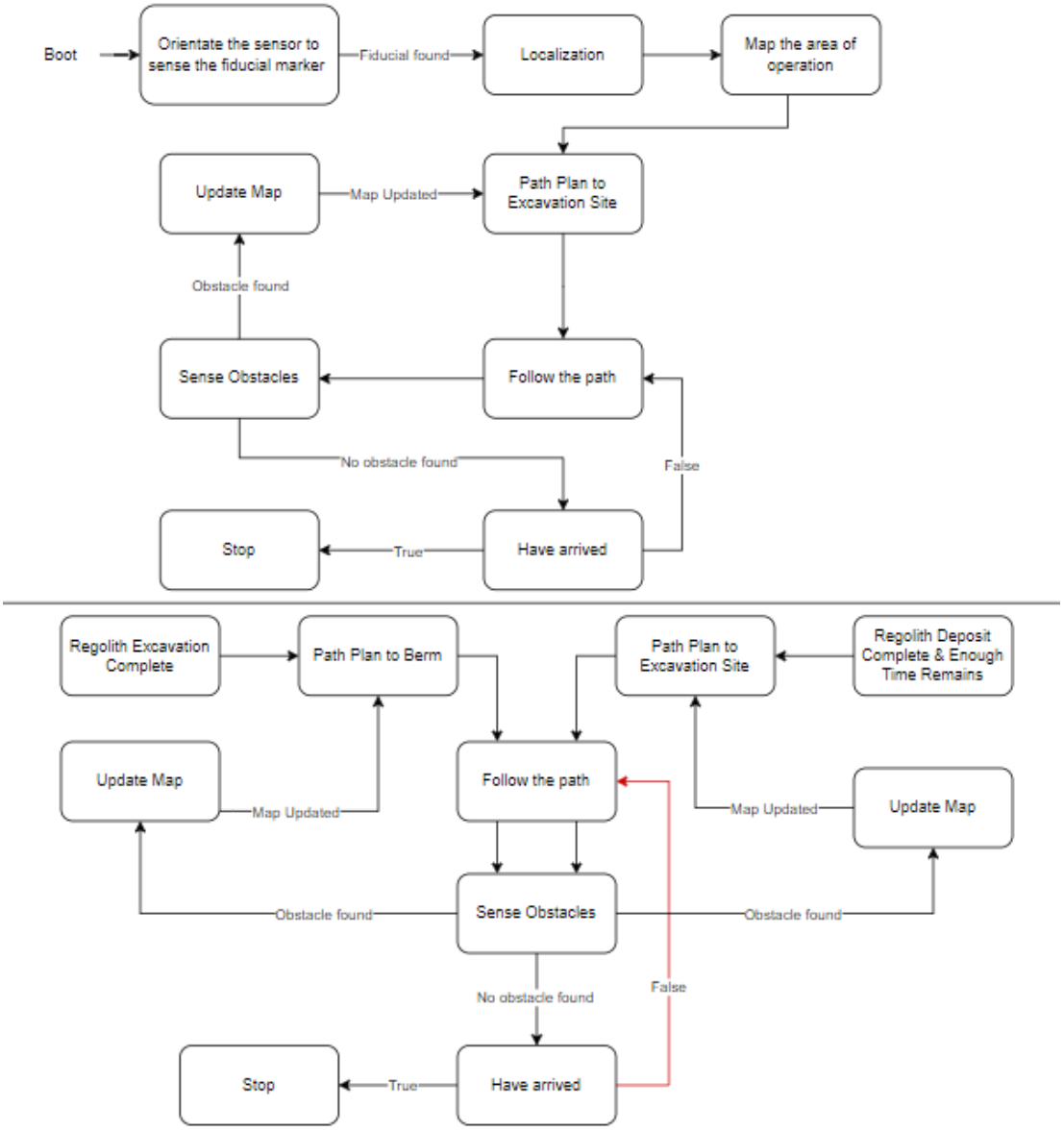

Fig. 4.43 Software System Architecture: Autonomous Navigation.

After reaching the excavation site, the robot's next task is to mine and store the regolith simulant. Fig. 4.44 illustrates how the software orchestrates the robot's actions to ensure continuous mining until a predetermined amount of regolith is collected or until the dig timer reaches its limit. A detection system actively monitors the excavation of regolith, measuring how long the system has dug (and the percentage of a completed cycle), if the system is jammed, or if the time is approaching its end. This real-time feedback enables the robot to discontinue its mining protocol, allowing ample time for a safe return to the berm. Upon return, the collected regolith can be deposited before the time expires.

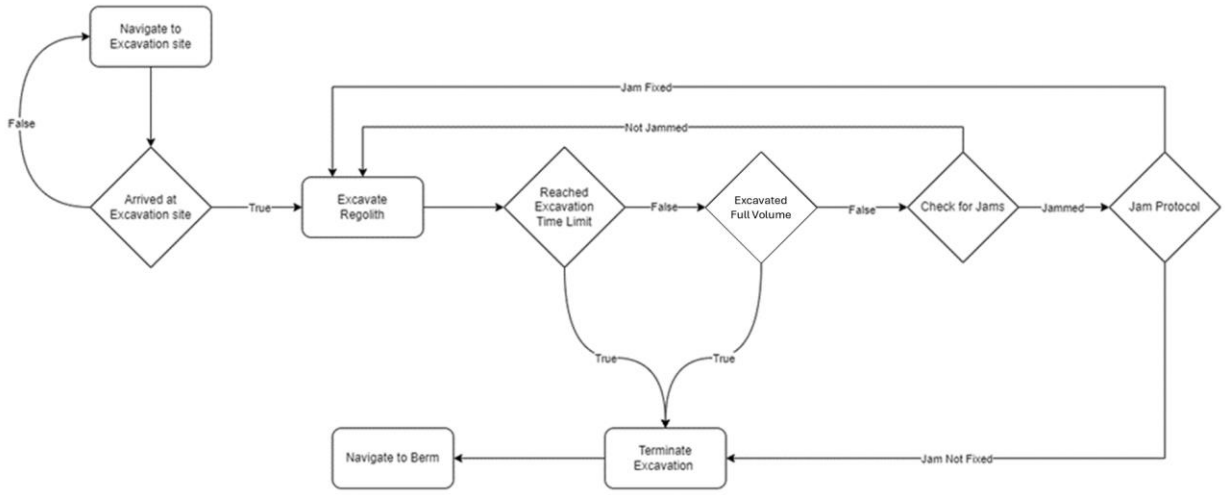

Fig. 4.44 Software System Architecture: Excavation of Regolith.

After arriving at the berm, the robot's next task is the deposition of the regolith into the berm. To achieve this, the robot first undergoes an orientation process, ensuring it aligns itself correctly with the berm zone. Sensors facilitate this alignment, allowing the robot to maneuver into the optimal position for regolith deposition. The robot proceeds to deposit the regolith. The robot continues depositing until the storage location on the robot reaches its minimum capacity. This process is represented in Fig. 4.45.

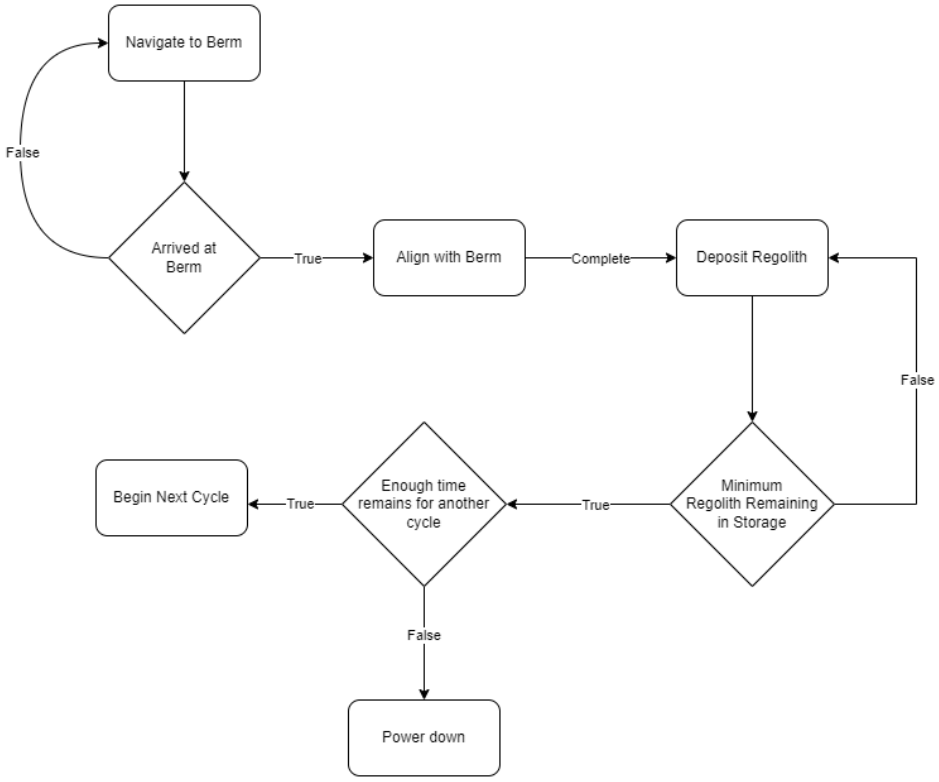

Fig. 4.45 Software System Architecture: Deposit of Regolith.

4.6.2 Environment

To achieve its objectives, a robot must effectively communicate with its sensors, actuators, motors, and other connected devices. However, facilitating this communication is not an easy task. A key consideration is the ability to independently test and develop subsystems. Previous sources of code can provide critical functionality and create a basis that our team can work from. We have chosen to utilize the Robot Operating System (ROS) framework to help us address these challenges and accelerate our development process.

ROS is an open-source middleware framework that provides a standardized way to develop, control, and communicate with robotic systems. ROS also provides an impressive library of prebuilt functionalities to help simplify the development process as well as offering robust simulation capabilities.

ROS nodes are individual software processes that perform specific tasks and communicate with each other to collectively control and coordinate a robotic system. ROS allows for nodes to be written in either C++ or Python, presenting a versatile approach for developing robotics applications. We are implementing most of the robot's low-level hardware-facing code in C++. This includes read values from sensors excluding cameras and code written to actuate motors or servos. All other code responsible for controls, computer vision, autonomy, navigation, and other tasks are written in Python. This is because Python is easier to read, write, and maintain. This combination of programing languages allows us to benefit from the performance offered by C++ and the developer productivity and maintainability of Python.

4.6.3 Localization and Pose Estimation

A critical component of the robot's operations (as described in Section 4.1) is localization at the beginning of the run, as well as continuous pose estimation during the run. For pose estimation, we have implemented two complimentary subsystems—a camera for reading field markings and wheel odometry.

The camera is placed atop a turntable on a tall pole, allowing it to have an unobstructed view of the field and the ability to rotate and detect markers. This camera position is shown in Fig. 4.46. The camera continually searches for fiducial markers placed on the field, allowing it to get accurate pose information.

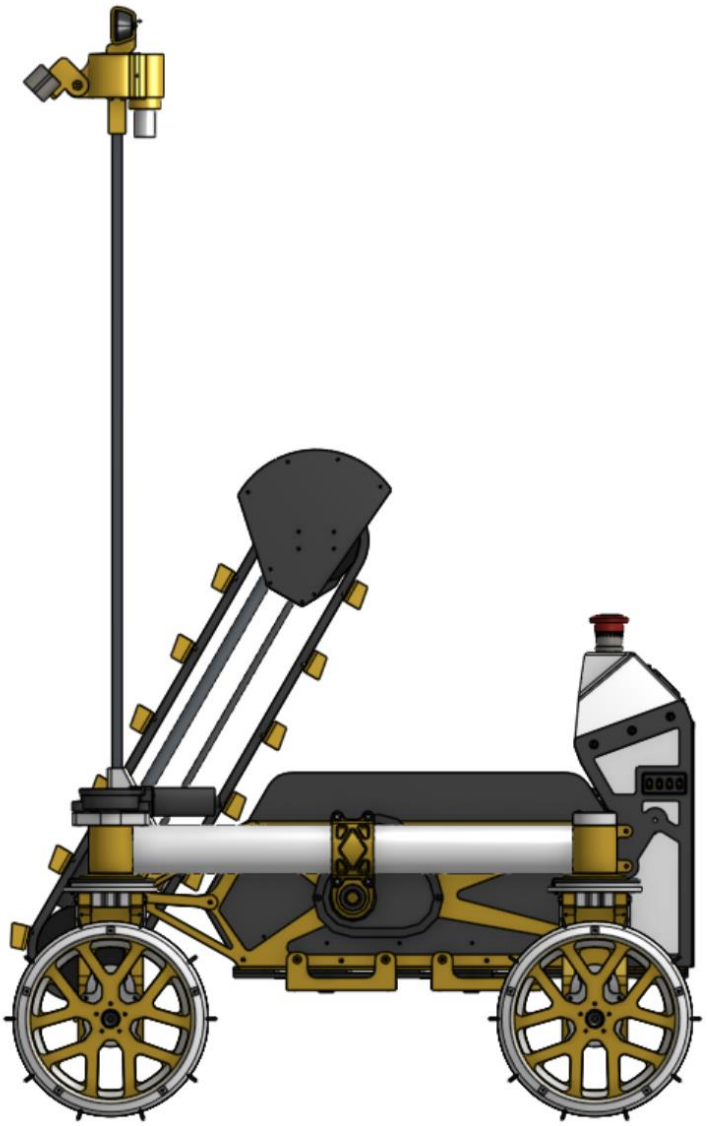

Fig. 4.46 Camera Position.

Once the camera can see a fiducial marker, the robot performs pose estimation using knowledge of the marker's location within the image and the marker's 3D coordinates with respect to the field coordinate frame. This establishes the robot's pose in the field's coordinate frame. This process of localizing using the starting zone's fiducial marker happens at the beginning of the run and is continuously repeated to maintain an accurate pose throughout the full duration of the run.

As the marker is the robot's only source of absolute position data, obtaining an accurate reading from the webcam is of high importance. From our testing with the camera, we found two different methods for improving fiducial tracking accuracy.

First, we implemented proportional control on the webcam pivot such that the marker was always in the center of the camera's field of view. This helps to prevent the robot from

losing sight of the marker as it turns during a run. It also keeps the marker fully within the frame because if any part of the marker is outside of view, the detection fails. Additionally, keeping the marker in the center reduces the effects of lens distortion. Although the library we are using accounts for distortion, results are best in the center of the camera. To implement proportional control, the Jetson calculates the distance from the center of the camera to the center of the fiducial. Next, the Jetson sends this data via a ROSTopic to the Arduino, which in turn controls the turntable motor. An example of a centered ArUco marker is depicted in Fig. 4.47.

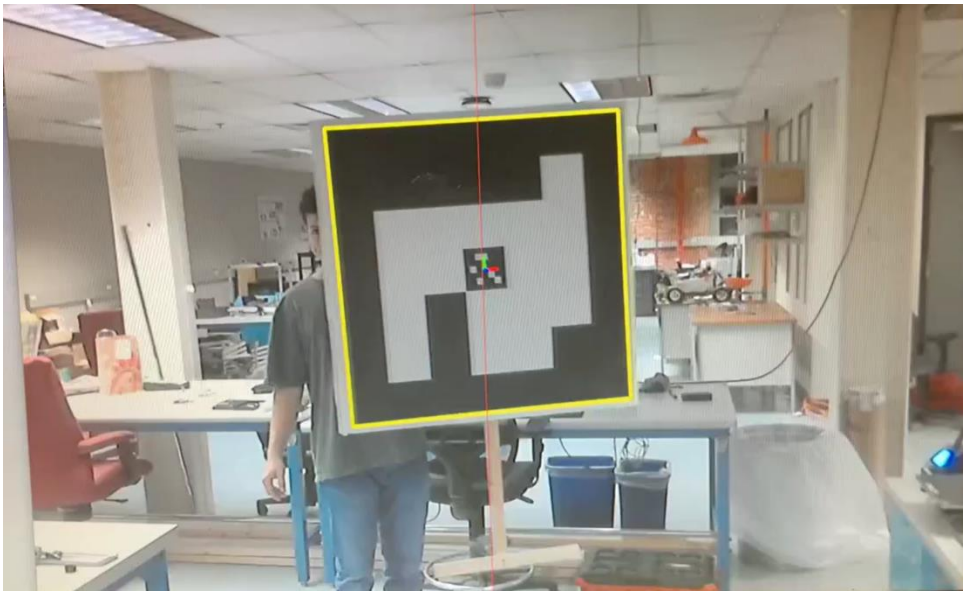

Fig. 4.47 Centered ArUco marker.

The second adjustment we made to improve fiducial tracking was to increase the size of the ArUco marker. This reduces accuracy loss due to limited camera resolution, especially at long ranges. By giving the camera more pixels to estimate the size of the marker, it can better estimate the distance. One drawback of an increased size is that the marker may be too large to be seen at close distances. In response, we developed a custom embedded fiducial marker from the ArUco 5x5 library. We did this by selecting a marker with many white squares and one black square in the center to be the outer maker and another marker with many black squares and fewer white squares to be the center marker. Next, we placed the center marker, downsized it by a scale of 7, in the center of the outer marker. This allows the camera to perceive the outer marker when farther away and perceive the inner marker at closer distances. Consequently, we can have more accurate localization estimates in more field locations without having to use a different fiducial detection library. An example of our embedded fiducial marker can be found in Fig. 4.48.

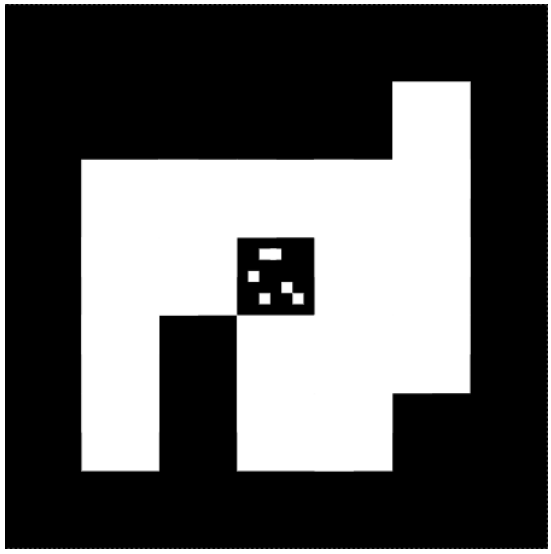

Fig. 4.48 Custom embedded fiducial marker. Adapted from [21].

Unfortunately, the webcam-fiducial method of localization runs into problems when the camera fails to detect the marker due to obstructions, dust, shaking, or other interference. Furthermore, the webcam is susceptible to noise in its readings. As such, there is a need for a second source of pose estimation, also helping to smooth out webcam noise. To address this need, the robot uses wheel odometry and a complimentary filter. We chose wheel odometry because it requires minimal additions to the robot and is not susceptible to any of the same interferences that could inhibit the webcam.

Odometry is accomplished by using the drivetrain encoders to track steering angles and wheel displacements. The Arduino uses this data to find updated poses for each wheel, which are then used to calculate the updated robot pose. These updates are sent over a ROSTopic to the complimentary filter. A schematic of this process is shown in Fig. 4.49.

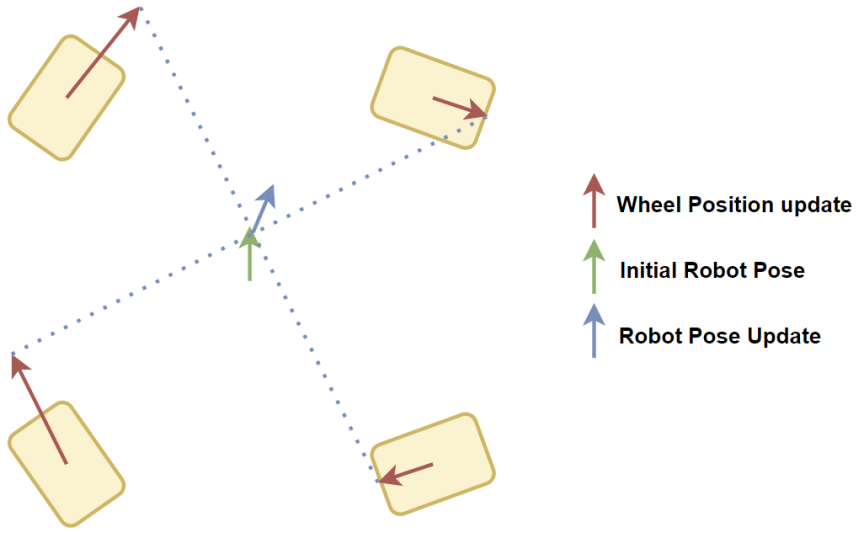

Fig. 4.49 Wheel odometry pose update.

The risk of odometry is that it is highly susceptible to drifting over time, especially in sand. As such, the robot uses a complimentary filter to merge both data streams. The filter runs as a ROS node on the Jetson Nano. It subscribes to camera pose estimates and odometry pose updates and fuses them together to obtain a better estimate. This is performed asynchronously, so that if one data stream goes down the system can rely on the other for estimates. When both systems are working properly, the robot can achieve an accurate and smooth pose estimation, and if one system goes down, the robot will default to the working system for its pose updates. A diagram of how this filter works can be seen in Fig. 4.50.

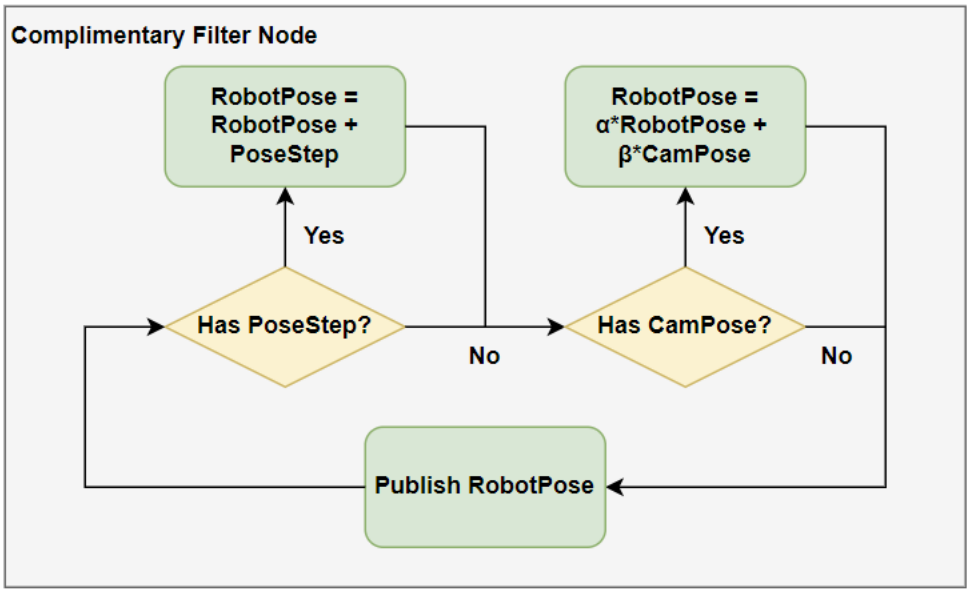

Fig. 4.50 Complementary filter.

4.6.4 Obstacle Detection

To perceive the environment and detect obstacles, we have equipped our robot with an Intel Realsense D455 stereo vision camera. We use this camera to produce color and depth images. We then use the depth data to estimate information such as the size and location of field obstacles. With this information we can calculate the location of any obstacles in the field's coordinate frame, and then save this information to a grid-cell representation of the field stored as the map of "drivable" and "undrivable" terrain. This map is critical for the implementation of efficient path planning algorithms. An example of the RBG images produced by the camera can be seen in Fig. 4.51.

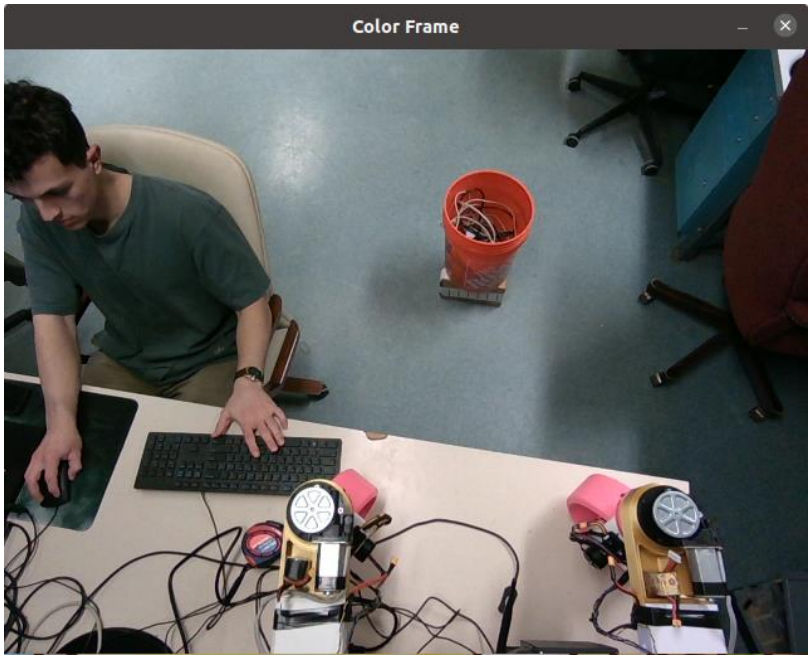

Fig. 4.51 Realsense RGB Imaging.

Next, to extract any useful data from the images regarding the location and size of obstacles, we align the depth data to the RBG image. Before we can do so however, it is important to crop the sides of the image to remove the data that is not useful. This avoids extra processing power being spent on detecting edges of the image that do not represent real obstacles. An example of an uncropped image that would have many contours that are not useful can be seen in Fig. 4.52.

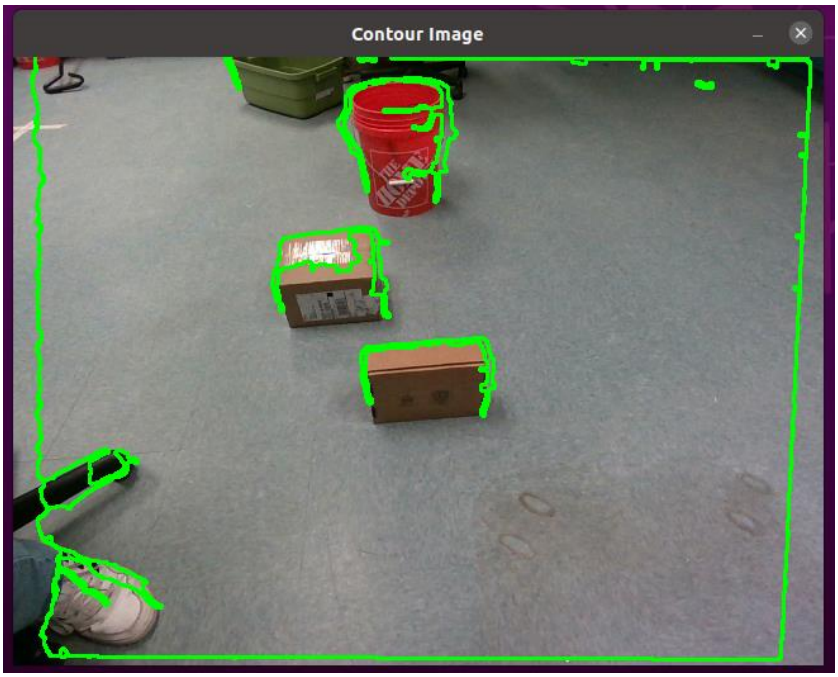

Fig. 4.52 Canny Edge detection with morphological operations applied, Uncropped.

Cropped RBG image and depth data can be seen in Fig. 4.53 and Fig. 4.54 respectively.

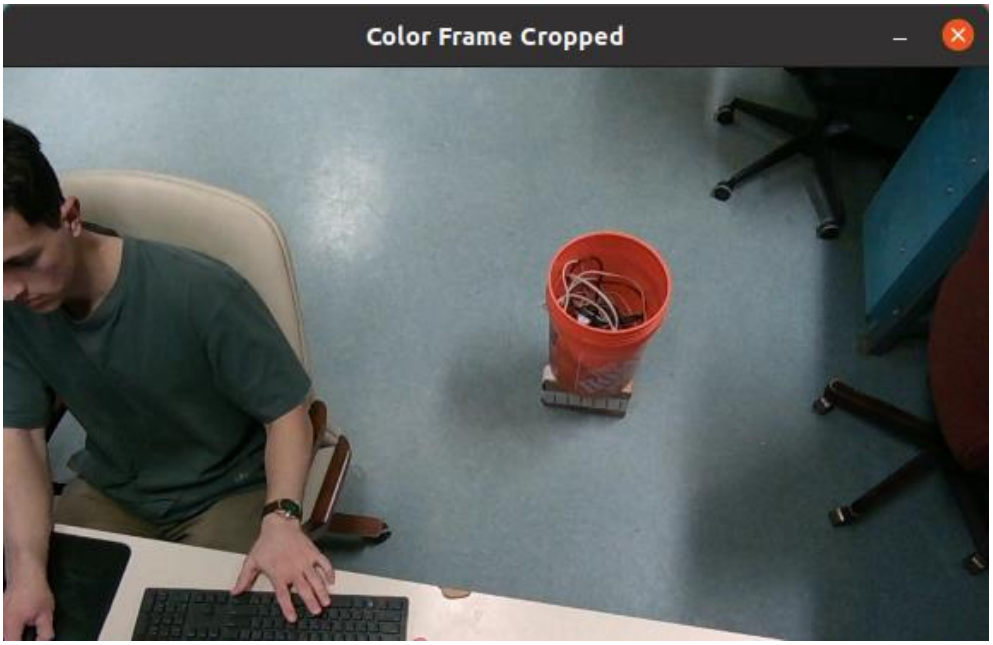

Fig. 4.53 Realsense RBG Imaging Cropped

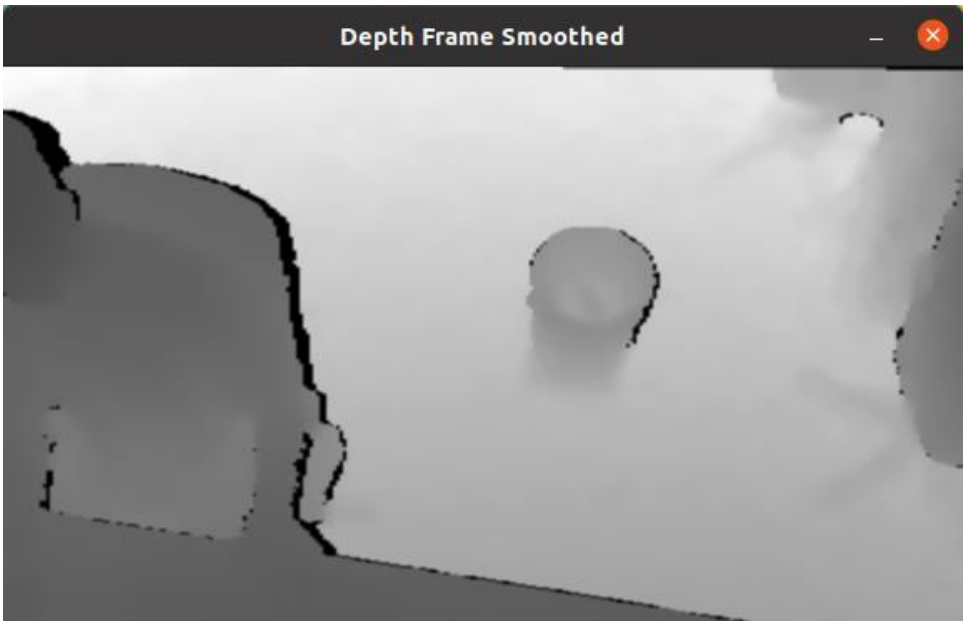

Fig. 4.54 Realsense Depth Imaging Cropped

Once the raw depth image is acquired, we can use OpenCV's Canny Edge Detection algorithm to detect rapid changes of depth in the image frame. After applying morphological operations to merge any immediately adjacent edges, we can then generate convex hulls to encapsulate all points included in the set of edge points. This will then allow us to filter the convex hulls by size and roundness to detect only obstacles such as rocks and craters without picking up on noise or the walls of the field. An example of the image after applying Canny Edge detection, morphological operations, and filtered convex hulls can be seen in Fig. 4.55.

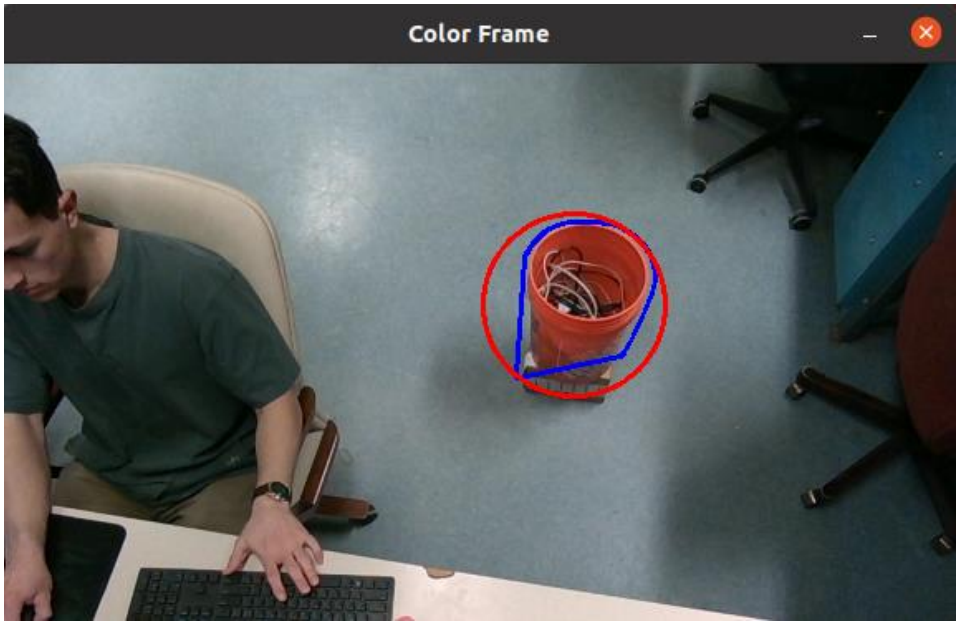

Fig. 4.55 Convex Hull Image

It is important to note that the team disregarded several perception techniques due to NASA's requirements. One example of a disregarded technique is the use of LIDAR modules for SLAM. NASA does not outright forbid the use of LIDAR; however, they explicitly state that the field walls shall not be used for the purposes of mapping, autonomous navigation, and collision avoidance. The reason for this rule is that there are no walls on the surface of the moon and therefore in the spirit of the competition, the use of walls is not allowed. Similarly, robots may not collide with walls. For this reason, touch sensors were not considered for perception.

4.6.5 Mapping and Autonomous Navigation

Autonomous navigation is a critical component of our robot's ability to complete mission objectives. It enables the robot to traverse the field and operate effectively without the intervention of human operators. This section details our plan for implementing autonomous navigation using stereo vision and SLAM techniques.

The primary objectives of autonomous navigation are to accurately determine the robot's position and orientation in the simulated lunar environment, implement perception techniques to understand what obstacles may be present in the way of the desired target location, and to

efficiently plan paths to allow the robot to get to the desired target location in the shortest possible time and while consuming the least amount of power.

Planning efficient motions is critical for reducing power consumption during movement and for minimizing the time required to move from one side of the field to the other. To plan efficient motions, we implemented the A* algorithm. A* is a widely used search algorithm that combines the best of both Dijkstra's algorithm as well as greedy algorithms [25]. Implementing this search algorithm allows our robot to make informed decisions on how to explore the field by considering the best possible paths to reach the target.

The code initializes an occupancy grid map using the OccupancyGrid message type from the nav_msgs.msg package in ROS. After initializing the ROS node named "map" and creating publishers for the occupancy grid map "/robot/map" and a transform (TF) broadcaster, the script sets up an empty grid space. Functions are defined to translate between the world coordinates and the grid coordinates. The grid's resolution and dimensions are set to the arena's dimensions to create the walls. The main loop publishes the grid map, broadcasts a transform between the "map" and "world" frames at a predefined rate, and periodically updates the occupancy grid with new obstacles.

In addition to path planning with the A* algorithm we also implemented a Pure Pursuit algorithm for local path tracking. Pure Pursuit utilizes a look-ahead point, which implements a steering angle for the robot, enabling it to smoothly follow a curved trajectory along the desired path of poses. Integrating A* for global path planning and Pure Pursuit for local tracking enables the robot to autonomously navigate the lunar terrain efficiently and effectively, consequently decreasing the drive time from point A to B.

4.6.6 Subsystem Controls

Controlling the many subsystems of this robot is a complex task, requiring many different techniques to keep everything working harmoniously. In the process of robot bring up, we encountered many different problems and solutions to handle the motion of the robot.

Every powered element of the robot is equipped with an AS5600 magnetic encoder to track position, and either an H-bridge or a proprietary motor controller to provide power. This allows us to perform proportional–integral–derivative (PID) controls on every subsystem of the robot to guarantee precise control of all actuators. We selected the AS5600 encoder due to its resistance to dust and its relatively low cost. It reads the absolute rotation of a diametrically-magnetized magnet attached to the output of each subsystem. Unfortunately, all the AS5600 encoders share an identical Inter-Integrated Circuit (I2C) address, resulting in the need for I2C multiplexers to handle switching between them. The robot uses ten encoders: four for the wheels, two for the steering, two for the intake, one for the localizer, and one for the deposit. As such, two 8-channel multiplexers switch between encoders. Fig. 4.56 shows the array of multiplexers used on the robot.

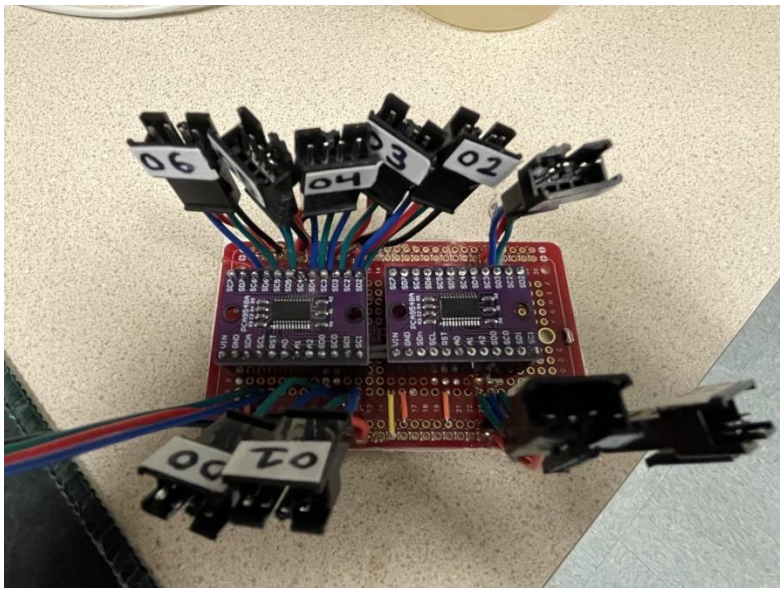

Fig. 4.56 Multiplexer Array.

The controls for the localizing camera proved to be a challenge, as the camera cannot continuously rotate due to it having a wire that wraps around the pole. To solve this, we implemented a system where upon reaching a limit in either direction, the camera will quickly turn around 360 degrees to unwrap the wire. To prevent a loop where the camera would turn around endlessly, we implemented hysteresis on the camera trigger such that the camera had an additional 30 degrees of rotation past the inflection point in both directions before it flipped around.

Drive train steering is accomplished using a state machine comprised of four states: Disabled, Driving Straight, Point Turning, and Instantaneous Center Turning. For both the Driving Straight and Point Turning states, the robot can set its wheels to predetermined angles and apply a given drive speed to all the wheels. However, for the Instantaneous Center Turning state, the robot must calculate the angles and speeds for both wheel sides. In this state, the robot is given an Instantaneous Center of Curvature (ICC), which is along the robot's y-axis. The robot is also given maximum wheel speed. With this, the robot calculates the necessary angles of the wheels to travel about the ICC. From there, the robot calculates the ratio of speeds between the wheels and sets the faster wheel to move at top speed while the other wheel moves at a proportional speed. A diagram of this is shown in Fig. 4.57.

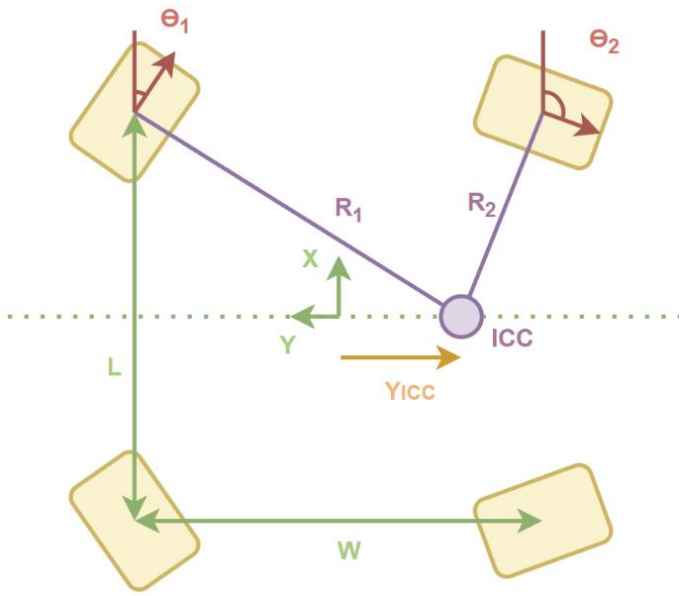

Fig. 4.57 ICC Turning.

5 System Testing and Validation

5.1 Drive Base

5.1.1 Steering

To validate the functionality of the duplex swerve steering concept, we programmed the prototype drivetrain with the ability to perform all three intended driving methods: driving straight, point turns, and turning about an instantaneous center. The prototype was able to perform all steering states without issue, as shown in Fig. 5.1 and 5.2.

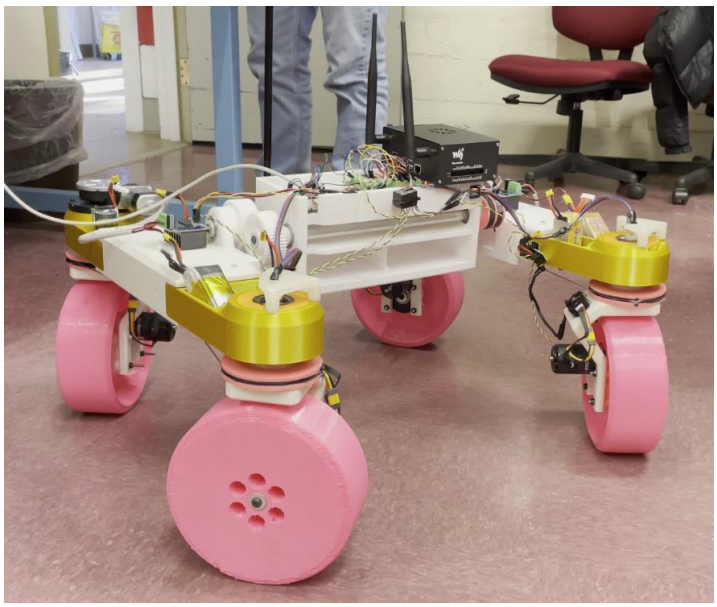

Fig. 5.1 Wheel Pods in Point Turn Configuration.

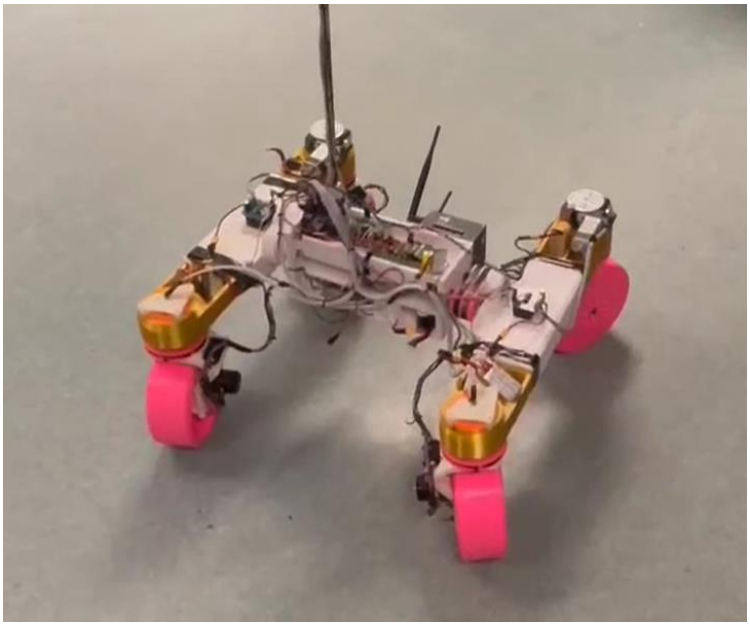

Fig. 5.2 Wheel Pods in ICC Configuration.

To test the functionality of the drivetrain in regolith simulant, we performed all driving techniques in sand. The purpose of these tests was to tune the driving motors so that the robot could easily traverse and maneuver over uneven terrain. Fig. 5.3 shows the set up for a sand test.

Fig. 5.3 Drivetrain Sand Test.

5.2 Regolith Management

5.2.1 Intake

We performed several tests in sand to evaluate the effectiveness of the intake subsystem. For these tests, we secured the intake and deposit subsystems to a rig, as seen in Fig. 5.4, that allowed the combined system to plunge and translate in a sand-filled tote of adequate depth. Plunging functionality is necessary because our excavation plan depends on the ability to reach

12 cm below the surface and the translation function is ineffective without plunging first. Translation functionality is necessary because most of the target volume is obtained by translating. The ability to use one rig to consecutively test both crucial functions allowed us to test the intake efficiently.

Fig. 5.4 Testing setup for sand tests.

After conducting the first sand test, we recognized some problems with the operation of the subsystem. These problems included a large accumulation of sand on the chain (and therefore, on the sprockets), insufficient motor power to run in sand, and rubbing between components. To resolve these issues, we made several changes to the intake system, detailed in Section 6.2.1. These changes resulted in less sand accumulation on the chain; although, the motor still had insufficient power to run in sand and some components were still rubbing.

Additional testing took place to determine actual conveyor motor torque requirements, based on a worst-case scenario. This scenario featured the bottom portion of the conveyor buried in the sand and all upward-facing scoops full of sand. We then calculated torque requirements using a lever arm (of known length) and a force gauge. This scenario and testing setup can be seen in Fig. 5.5. Based on these testing results, we decided on a motor that meets our updated power requirements, which is detailed in Section 4.4.1.

Fig. 5.5 Conveyor torque testing.

Bellows made from clear vinyl covered the lead screw and aluminum rods to protect against regolith. To verify the bellows' ability to keep out particles, we flipped the test bellow tubes inside out, then put regolith inside and aggressively shook them around. With the seam on the inside, the tube's ability to keep regolith in should correlate to the bellows' effectiveness. We found the ripstop nylon maintained the regolith inside, while the clear vinyl did not. The results of these tests are shown in Fig. 5.6.

Fig. 5.6 The results of the first bellows regolith test.

After assembling the robot, we completed more tests to tune the autonomous plunging and digging cycles. We primarily performed these tests in an indoor sand pit constructed in our lab space. This provided easy access to power, computers, and tools as needed. The testing setup is shown in Fig. 5.7.

Fig. 5.7 Intake testing setup.

5.2.2 Storage & Deposit

We conducted preliminary subsystem testing on the deposit mechanism after the first system assembly. We installed several dust mitigation features, including the fabric canopy and tubular nylon bellows, and tested them for dust rejection. These features can be seen in Fig. 5.8 and Fig. 5.9.

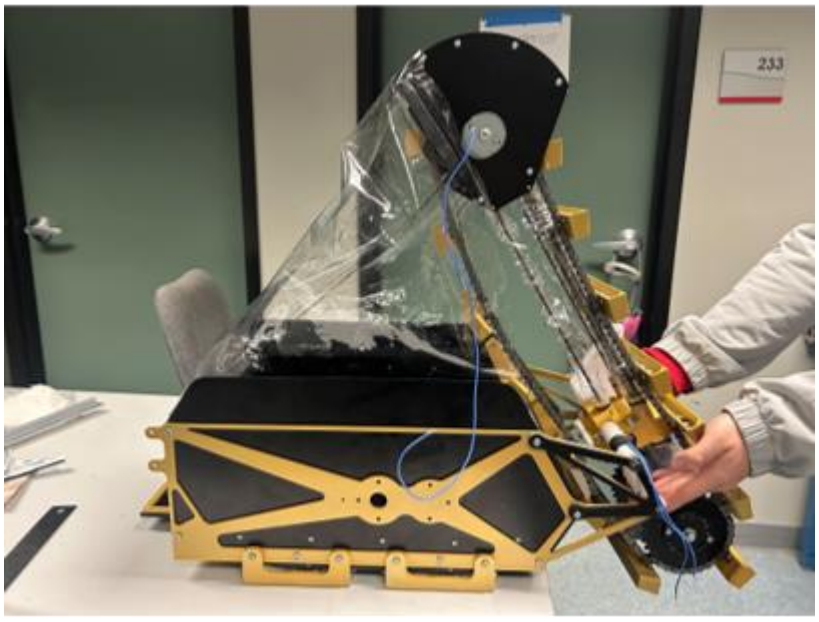

Fig. 5.8 Assembled Storage/Deposit system with canopy and intake mechanism.

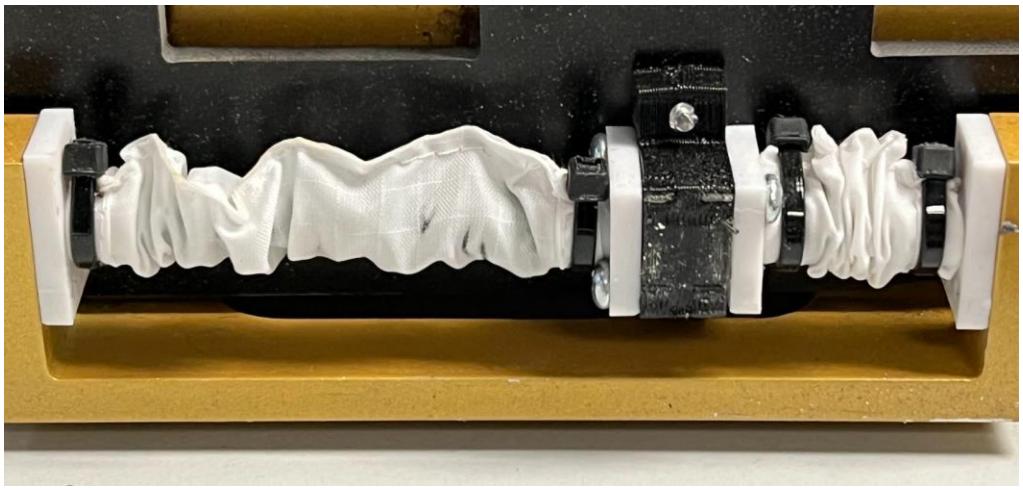

Fig. 5.9 Sliding mechanism with ripstop nylon bellows installed.

The bellows proved to provide sufficient dust protection for the linear rails, such that the mechanism did not bind up during initial testing. To validate that the storage structure was structurally sufficient to hold the nominal amount of sand/regolith and capable of depositing its load, 0.01 m^3 of sand was manually added to the storage. We connected a 3S LiPo battery to the yoke actuation motor and almost all the sand fell out of the storage. Unexpectedly, we found

that some slots jammed up because larger rocks clogged up the mechanism. We do not plan to encounter rocks of this size in the storage because the intake scoops are not large enough to pick them up. This test is found in Fig. 5.10-5.13.

Fig. 5.10 Testing Setup 2.

Fig. 5.11 Deposit Yoke Mechanism Activated.

Fig. 5.12 Deposit Process Ongoing.

Fig. 5.13 Results of Deposit Test.

At the first fully integrated test on the beach, a corner of the fabric canopy ripped during excavation. While the conveyor was in a lowered position, the loose fabric entangled itself between the scoops, and tore when the conveyor switched rotational directions. The team concluded that the excessive amount of slack given to the canopy in combination with the stiff, slightly tacky nature of the plastic vinyl caused this entanglement.

The system also had difficulties depositing wet sand on the beach. In the days leading up to the first test, the location experienced several days of cold weather and rain. The damp sand stuck together and clogged the trapdoor slots, failing to deposit. This issue is insignificant since the team successfully tested the deposit system with dry sand.

During testing of the intake system, we saw the much of the collected material would stay towards the front of the storage. Improvements to sand distribution and other storage and deposit issues are discussed in Section 6.3.2.

5.3 Electronics

To test the electronic systems of the robot, the team first completed benchtop subsystem testing. This way, the team could troubleshoot problems individually on a subsystem level before integrating subsystems together. After assembly of the robot, the team tested systems together, as detailed in other sections. A discussion about electronic issues and solutions can be found in Section 6.4.

5.4 Software

The team completed much of the testing for the robot's software capabilities using the prototype drivetrain. This allowed for the software team to work in parallel with the manufacturing and assembly of the final robot. The prototype drivetrain allowed for the development of autonomous localization, obstacle detection, and navigation.

For localization, we completed initial testing to determine the viability of the ArUco marker. For this test, we mounted an ArUco marker to the wall of our lab, detecting the marker with the Logitech webcam used for localization. Then, we estimated our position with respect to the marker as discussed in Section 4.6.3. Finally, we compared the calculated value to the true position of the camera and displayed the maximum positional error in Fig. 5.14. This chart overlays the testing results over the arena map, to show the results in each arena zone. We

contained the testing was to areas of importance—the excavation zone and construction zones. The size of the ArUco marker in this test was 0.5 m x 0.5 m. The results of these tests led to the development of the custom nested ArUco marker discussed in Section 4.6.3.

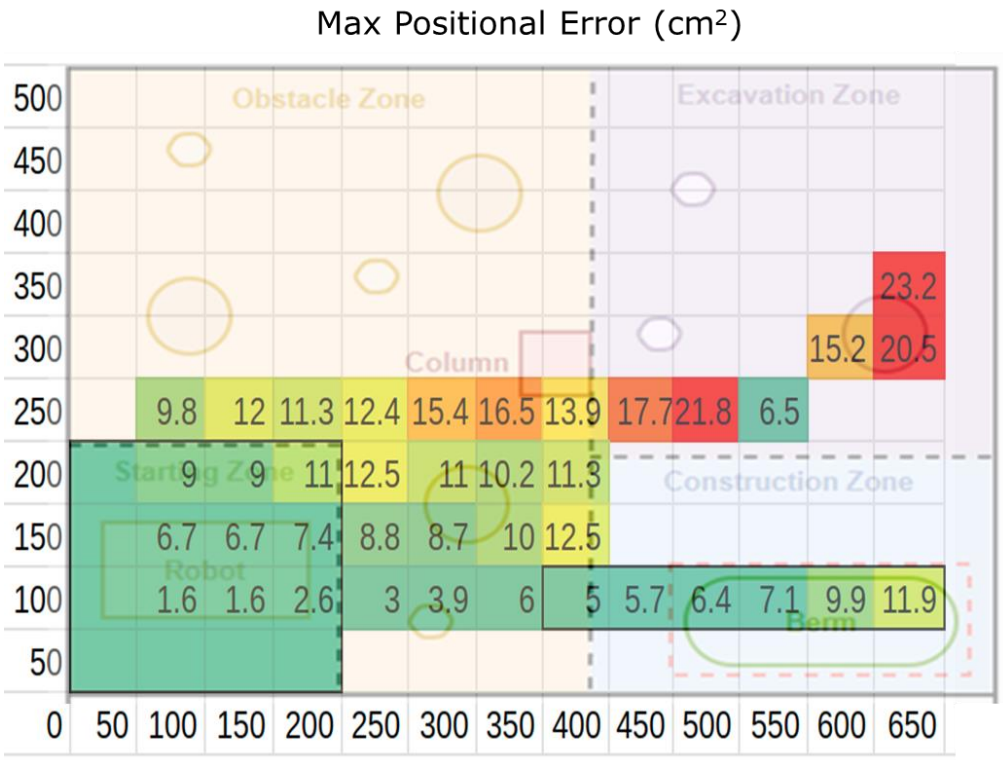

Fig. 5.14 Localization ArUco Testing.

Testing of navigation includes incorporated obstacle detection and SLAM. The team accomplished this by creating obstacles in the lab space for the prototype drivetrain to navigate around. This simulated environment would be indicative of the obstacle zone found in competition and allowed the team to develop the required software for navigation. The setup for these tests can be found in Fig. 5.15.

Fig. 5.15 Navigation Testing.

The final assembly of the robot allowed the team to develop autonomous digging and deposit sequences. The team achieved most of this progress in the indoor sand pit.

5.5 Validation

To validate our TPMs, we tested the robot in the lab sand pit and on the beach. The team validated the Maximum Mass and Size requirements in the lab, with the results of the tests listed in Table 5.1. The robot is oriented so that the longest dimension (length) is the height from the bottom of the wheels to the top of the camera pole.

Table 5.1 Mass and Size Validation

	TPM Minimum Goal	**Measured**
Mass	40 kg	28.39 kg
Width	75 cm	73.0 cm
Height	75 cm	64.1 cm
Length	150 cm	116.5 cm

To validate the Movement goal, the robot had to travel seven meters in a straight line in sand. This test is shown in Fig. 5.16. The robot completed this test in approximately 53 seconds.

Fig. 5.16 Movement Test.

For Berm Construction, the robot completed an autonomous digging cycle in the sand pit, including protocols to prevent jamming. This test is shown in Fig. 5.17. The robot then returned to its starting location and deposited all the collected material, shown in Fig. 5.18.

Fig. 5.17 Berm Construction Test, digging cycle.

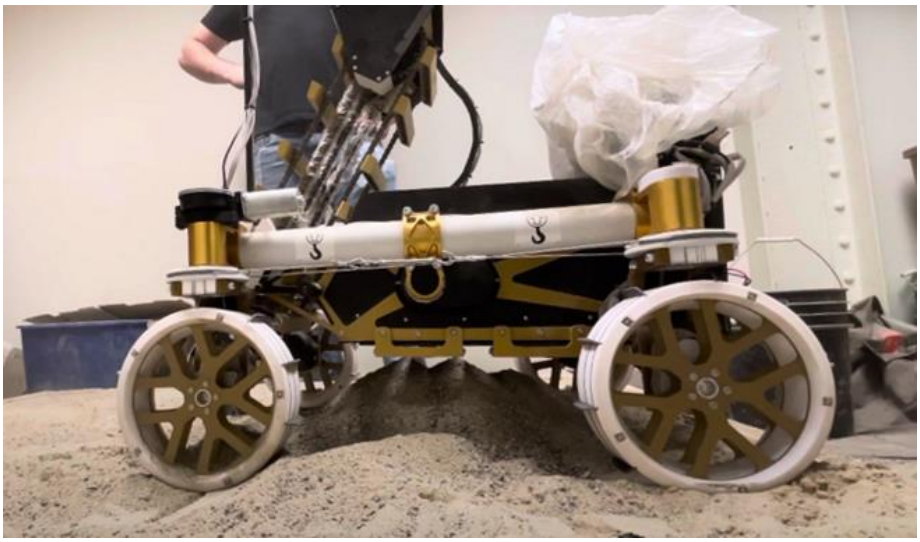

Fig. 5.18 Berm Construction Test, deposited material.

Finally, the team validated all safety guidelines by using a checklist with safety requirements from the NASA Lunabotics Guidebook [3]. This checklist can be found in Appendix C.

6 Analysis and Discussion

6.1 Requirements

The robot partially met the minimum goals at the end of the project and completed some reach goals. Table 6.1 displays each goal the robot met (highlighted in green), goals that the robot can complete but have not been validated through a recorded test (highlighted in yellow), and each goal the robot failed to accomplish (highlighted in red). The following sections detail the outcomes of system tests and address any unachieved goals.

Table 6.1 Performance Evaluation

Technical Performance Measures	Minimum Goals	Reach Goals
Movement	Shall be able to traverse at least 7 m in 2 min. Shall not get stuck on rocks or in craters.	Should be able to traverse at least 7 m in 1 min.
Berm Construction	Shall be able to deposit at least 0.01 m^3 of regolith in the berm construction zone after 15 min of operation.	Should be able to deposit at least 0.03 m^3 of regolith in the berm construction zone after 15 min of operation.
Dust Protection	Shall not lose functionality due to ingress of particulate matter after operating for 30 min in sand.	Should operate without the ingress of particulate matter in any critical system.
Maximum Mass	Shall be less than 40 kgs.	Should be less than 20 kgs.
Size Requirements	Shall fit within an envelope of 1.50 m x 0.75 m x 0.75 m.	-
Energy Consumption	Shall be able to operate for at least 30 min.	Should be able to operate for at least 45 min.
Autonomy	Shall be able to detect obstacles, prevent collisions, and complete the digging sequence autonomously.	Should be able to complete navigation, digging, and dumping completely autonomously.
Safety	Shall comply with competition required safety precautions as defined in the Lunabotics guidebook.	Should have a graphical display of robot system telemetry for monitoring purposes.

The following goals were not successfully tested by the end of project submission: Berm Construction, Dust Protection, Energy Consumption, and Autonomy. These unsuccessful goals are discussed below, with some to be tested before the date of competition. Some goals were not fully validated before project submission, but the robot proved its capabilities to achieve these goals (Berm Construction and Autonomy) through system testing. Persevering electronic issues before project submission prevented the team from successfully validating these requirements.

The robot demonstrated its ability to collect and deposit sand, but the collected material was never measured to ensure its volume. Regarding the reach goal, it was important to design an intake system that could complete multiple digging and deposition cycles sequentially. Aptly, the reach goal for Berm Construction drove the digging requirements for intake; although this goal was never tested, multiple cycles will be used in longer trial runs.

The team did not have the opportunity to record a 30-minute test for Dust Protection, due to electronics issues discussed in Section 6.4. The team successfully tested the dust isolation features of each subsystem and intends to test all integrated systems before the competition.

The team set the reach goal for Maximum Mass at 20 kg, an ambitious goal given the scale of past Lunabotics robots. The mass of the robot totaled around 28 kg, and the team believes that lightweighting efforts to reach 20 kg would require major redesign of some subsystems.

Like Dust Protection, the team was unable to test the reach goal for Energy Consumption but intends to do so before the competition.

The team successfully tested the autonomous digging and dumping capabilities of the robot, but never fully validated the navigation and obstacle detection systems. The robot displayed its ability to detect obstacles using its RealSense camera, but never validated its capability to navigate around obstacles like those found in competition.

The team did not have time to implement a graphical display of telemetry data, but rather opted to monitor the system health through terminal output.

6.2 Drive Base

We solved many of the mechanical issues with the drivetrain before final assembly, because we had time to troubleshoot with the prototype drivetrain. Some of the changes include a more robust cable capstan system and limits for the rocker suspension. The final design for the drivetrain is discussed in Section 4.3. Overall, the drivetrain was able to perform all desired steering techniques, maneuver at the chosen speed, and the rocker suspension always held all four wheels on the driving surface.

6.3 Regolith Management

6.3.1 Intake

For the intake subsystem, we created a course of action to address each issue found in testing. Firstly, we hypothesized that the lubrication oil on the chain, which was applied by the vendor, could be causing the sand and dust to stick to the chain, as seen in Fig. 6.1 (left). The plan to resolve this was to degrease the chain overnight. Additionally, we were aware that sand or regolith particles could compact in the roots of the sprocket teeth. To prepare for possible compaction issues, we proactively cut escape holes in the sprockets, as seen in Fig. 6.1 (center).

After conducting the second sand test, we noticed significantly less sand and dust sticking to the degreased chain, as seen in Fig. 6.1 (right).

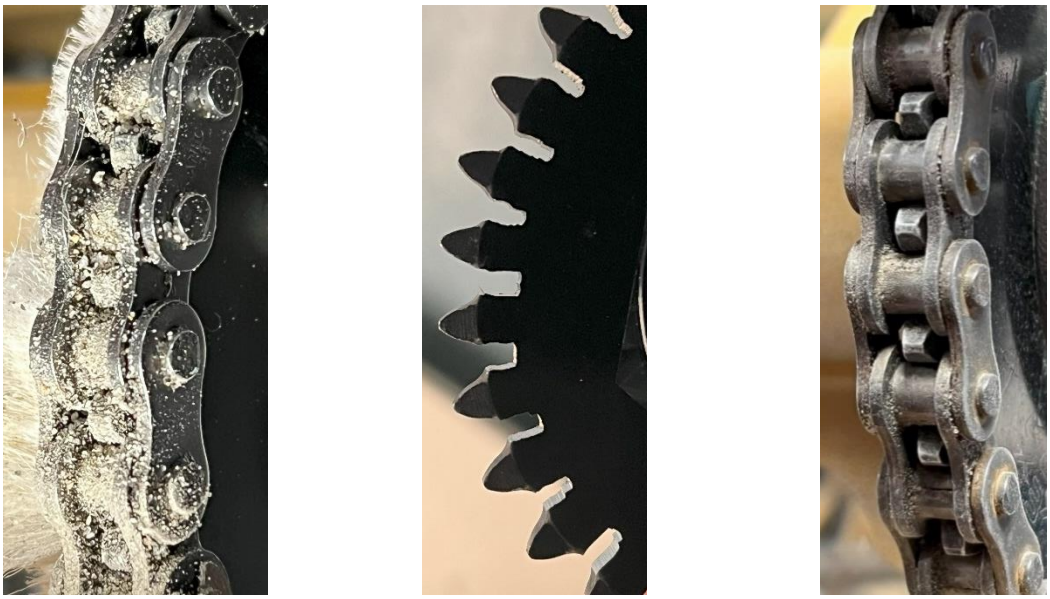

Fig. 6.1 Left: Sprocket and chain after first sand test. Center: Escape holes cut into sprockets. Right: Degreased sprocket and chain after second sand test.

During testing of the intake system, the lead screw deformed, incapacitating conveyor actuation. The deformed lead screw can be seen in Fig. 6.2 (left). We hypothesized that an existing bend in the screw caused this deformation, exacerbated by handling and digging loads. To remedy the actuation system, we replaced the previous lead screw with a thicker lead screw (approximately 0.1” larger in diameter), more apt to take both bending and buckling loads. The new lead screw can be seen in Fig. 6.2 (right).

Fig. 6.2 Left: Bent lead screw, with bellows removed. Right: New lead screw replaced in system.

As a result of the bellows test, we concluded the leaking was caused by the holes poked in the vinyl during the sewing process. To solve this, we explored other ways to seal the vinyl, such as reinforcing the stitches with fabric glue to seal the holes. Ultimately, the best solution we found was to melt the edges of the clear vinyl together, successfully keeping regolith inside during testing.

After making the listed changes to the intake system, it was able to meet all its design requirements, including digging at intended speed and plunging to the desired depth. The autonomous digging routine limited the conveyor jamming to a minimum.

6.3.2 Storage & Deposit

The first issue the team encountered with the deposit system was that the sliding mechanism was over-constrained, creating a large buildup of friction when actuating the trapdoor. Small adjustments were made to mitigate this problem, such as trimming the brushes and printing some parts out of flexible TPU.

As a result of the canopy ripping during the beach test, we fabricated a new canopy from ripstop nylon, which is more flexible and slippery. This allows the fabric to move out of the scoops' path more easily than the vinyl. All edges were reinforced with a rolled hem to resist tearing and less slack was given. This proved to be effective in eliminating any snagging of the canopy.

To address the material bias towards the front of the storage, we implemented louvers that would direct the sand to the middle and back of the storage. This allowed for the distribution of collected material to spread more evenly across the storage. The improvement from the louvers is shown in Fig. 6.3.

Fig. 6.3 Left: Initial material distribution. Right: Material distribution with louvers.

The storage system allowed for storage of 0.013 m^3 of collected material, surpassing the desired volume in one dig cycle. Furthermore, the deposit system allowed for a quick and energy-efficient deposition of the material held in storage.

6.4 Electronics

A major electronics issue caused inconsistent control while simultaneously running brushless and brushed motors. The team discovered this problem while completing integrated system testing, determining the root cause via isolated system testing with an oscilloscope. This issue would cause the Arduino Mega to crash, requiring the team to E-stop the robot and reset the Arduino. The team solved the crashing by isolating the power sources for the brushless and brushed motors and controllers.

Persistent issues with electromagnetic interference (EMI) caused additional crashing issues that prevented many long-running tests. By the time of project submission, many of these issues still caused frequent problems. Before the competition, the team intends to isolate wiring for encoders, motors, and other electronic components to mitigate EMI as much as possible.

Further improvements to the robot's electronics system included the incorporation of circuit breakers, improved battery life for the 5V systems (up to 5 WH), and neater wiring. With these changes, the electronics system allowed for short-term teleoperation as well as autonomous control of each subsystem.

6.5 Software

The intended software capabilities of the robot were autonomous navigation, excavation, and deposition. The team confirmed these capabilities through validation of the TPMs, including autonomous navigation around obstacles and a completely autonomous digging and deposition cycle. By the submission of the project, the robot lacks the capability to autonomously navigate to the berm construction zone and deposit in accordance with the strategy listed in Section 4.4.

7 Management

7.1 Timeline

It is difficult to accurately predict a timeline on a complex year-long project that interfaces with many students. To do so, the team designated a Project Manager who oversaw the long-term and short-term goals of the project, keeping everyone on track throughout the year. Initial project deadlines are shown in Gantt form in Fig. 7.1. Apart from milestones, the schedule pictured in Fig. 7.1 was not a hard timeline, but rather a tool for the team to reference.

This schedule evolved over the year, to accommodate shifts in priority, unforeseen events, and design changes. Fig. 7.2 shows an updated schedule in Gantt form (updated March 27th).

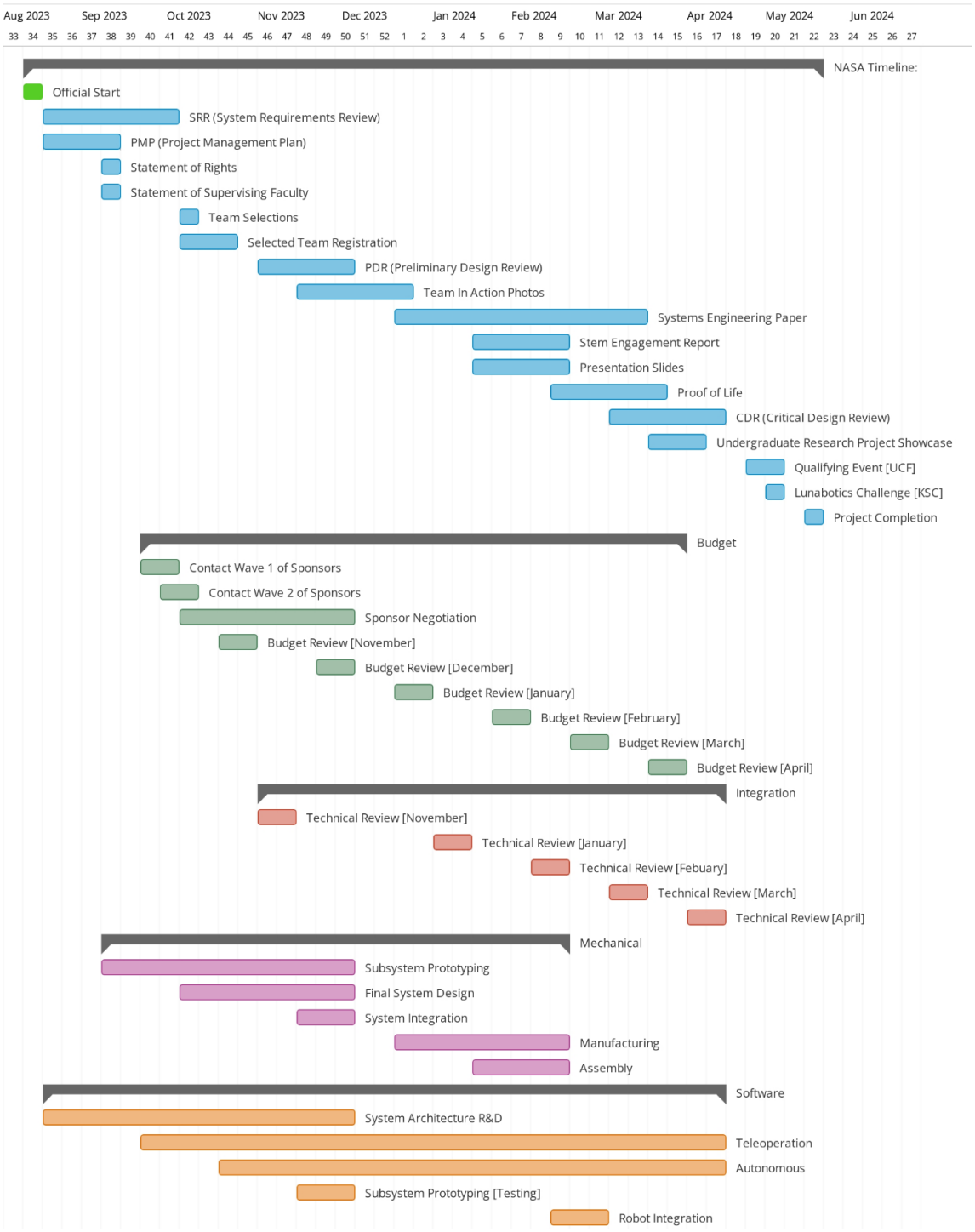

Fig. 7.1 Timeline in Gantt view. Critical deadlines can be found in [2].

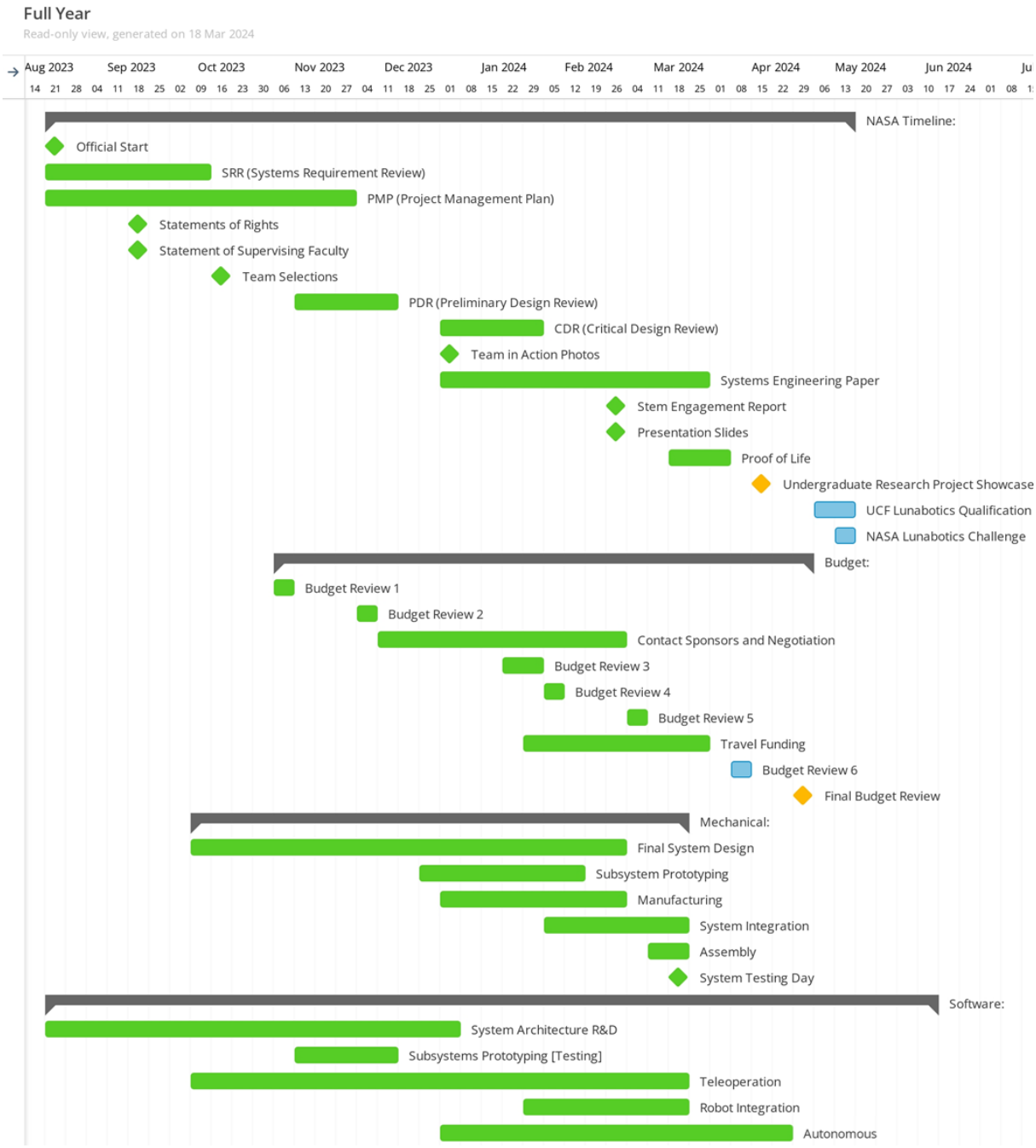

Fig. 7.2 Updated Project Timeline in Gantt view. Updated as of March 27th, 2024.

Notable changes between the two charts are listed as follows. Firstly, our group determined to hold final design reviews per subsystem during the month of January.

Next, sponsor outreach and negotiations took longer than previously planned. This had a major impact on the finances of the project, requiring careful budgeting for the procurement of robot materials. We also added the task of obtaining funding for travel expenses, which the team predominately acquired through WPI.

Finally, due to unforeseen setbacks, manufacturing took longer than originally planned. This pushed back final assembly and integration of robot systems. Our initial schedule included buffer time to account for delays of this nature, allowing us to successfully complete assembly of the robot to meet all required deadlines.

In tandem with the Gantt chart, our team utilized a prioritized to-do list, updated weekly. This list helped to divide tasks between team members and reallocate effort as necessary to meet schedule deadlines.

7.2 Budget

Table 7.1 shows a preliminary budget demonstrating the intended spending breakdown for building and competing with our Lunabotics robot. The team projected prices for various expense categories using the 2022 WPI Lunabotics Team's documentation [4], research of current market prices of supplies, and culmination of prior knowledge. The team made this budget at the outset of the project to determine how much monetary and in-kind support they needed.

Table 7.2 shows the current amount spent by the team (updated April 25th, 2024). There are many notable changes from the original cost budget and the current spending/remaining budget. These are listed as follows:

Some sections were merged with corresponding subsystem-level sections, including ESCs, cameras/sensors, and software. We also added a category to the budget, called miscellaneous expenses. This category included materials for outreach, tools, and hardware storage.

Next, our team spent much less than originally planned on electronics, because we were able to source many components from past teams.

The estimated cost of outtake/storage is much less than initially budgeted. This is because the team was able to use much of the prototype structure in the final assembly. We were able to reallocate some of this unused budget towards outsourced parts for the drivetrain, explaining the increase in spending in that category. This helped us to combat some of the manufacturing setbacks.

Finally, the estimated cost of travel and associated expenses are much higher in the updated table. The qualification stage at UCF makes the trip to Florida longer than previous years, increasing the cost of travel.

Table 7.1 Initial Team Budget

System Hierarchy Cost Estimates			
Drivetrain	Frame	$	(800.00)
	Wheels	$	(600.00)
	Actuators	$	(600.00)
	Miscellaneous	$	(500.00)
	Drivetrain Total	$	(2,500.00)
Intake	Prototype	$	(400.00)
	End Effector	$	(250.00)
	Actuators	$	(200.00)
	Structure	$	(300.00)
	Miscellaneous	$	(350.00)
	Intake Total	$	(1,500.00)
Outtake/Storage	Prototype	$	(200.00)
	Actuators	$	(100.00)
	Agitator	$	(200.00)
	Structure	$	(200.00)
	Miscellaneous	$	(250.00)
	Outtake/Storage Total	$	(950.00)
Electronics & Power	Power	$	(300.00)
	Speed controllers	$	(630.00)
	Microcontrollers	$	(430.00)
	Cameras and Sensors	$	(700.00)
	Wiring	$	(150.00)
	Wireless Access Point	$	(180.00)
	Electronics Total	$	(2,390.00)
Software		$	-
System Hierarchy Total		$	(7,340.00)
Labor Costs			
(factored into subsystem budget)		$	-

Funding		
Expected Student Contribution	$	2,000.00
Expected Sponsor Contribution	$	2,140.00
Secured Funding (WPI and past)	$	4,500.00
WPI Funding Request for Travel	$	5,200.00
Funding Total	$	13,840.00
Lunabotics Deliverables		
Public Outreach Project	$	(300.00)
Travel Cost to Florida		
Travel (for one car)	$	(400.00)
Lodging (Airbnb)	$	(2,400.00)
Food (per person)	$	(200.00)
Robot Shipping	$	(400.00)
Travel Total	$	(5,200.00)
TOTALS		
Project Cost Excluding Travel	$	(7,640.00)
Project Balance Excluding Travel	$	6,200.00
Project Cost	**$**	**(12,840.00)**
Project Balance	**$**	**1,000.00**

Table 7.2. Amount Spent

System Hierarchy Costs		
Drivetrain	Frame	$ (1,290.08)
	Wheels	$ (716.99)
	Actuators	$ (861.79)
	Miscellaneous	$ (309.01)
	Drivetrain Total	$ (3,177.87)
Intake	Prototype	$ (13.35)
	End Effector	$ (212.80)
	Actuators	$ (492.58)
	Structure	$ (869.36)
	Miscellaneous	$ (31.83)
	Intake Total	$ (1,619.92)
Outtake/Storage	Prototype	$ (201.24)
	Actuators	$ (38.98)
	Agitator	$ -
	Structure	$ (80.55)
	Miscellaneous	$ (190.46)
	Outtake/Storage Total	$ (511.23)
Electronics & Power	Power	$ (191.70)
	Speed Controllers	(merged)
	Microcontrollers	$ (282.76)
	Cameras and Sensors	(merged)
	Wiring	$ (98.50)
	Wireless Access Point	$ -
	Electronics Total	$ (572.96)
Misc. Expenses		$ (439.44)
System Hierarchy Total		$ (6,321.42)
Labor Costs		
(factored into subsystem budget)		$ -

Funding	
Student Contribution	$ 2,320.62
Sponsor Contribution	$ 5,830.00
Secured Funding (WPI and past)	$ 4,000.00
WPI Funding for Travel	$ 3,550.00
Funding Total	$ 15,700.62
Lunabotics Deliverables	
Public Outreach Project	(merged)
Travel Cost to Florida	
Travel (round trip flight)	$ (2,613.29)
Lodging (Airbnb)	$ (4,566.09)
Car Rental	$ (958.58)
Robot Shipping (estimated)	$ (600.00)
Travel Total	$ (8,737.96)
TOTALS	
Project Cost Excluding Travel	$ (6,321.42)
Project Cost	**$ (15,059.38)**
Project Balance	**$ 0.00**

To track cost budget across the year, the team updated all spending compared against the initial budget as the project progressed and updated planned expenses for future weeks. This is shown in the figures below: Fig. 7.3 shows the planned expenses over the project duration and Fig. 7.4 shows the budget as many major purchases were completed (February 26th, 2024). Monthly reviews of the cost budget, along with a running list of itemized expenditures, helped keep the team expenses in agreement with the initial project cost budget. The team also proactively contacted sponsors, deans, and department heads to secure funding for the project and the travel cost associated with the competition.

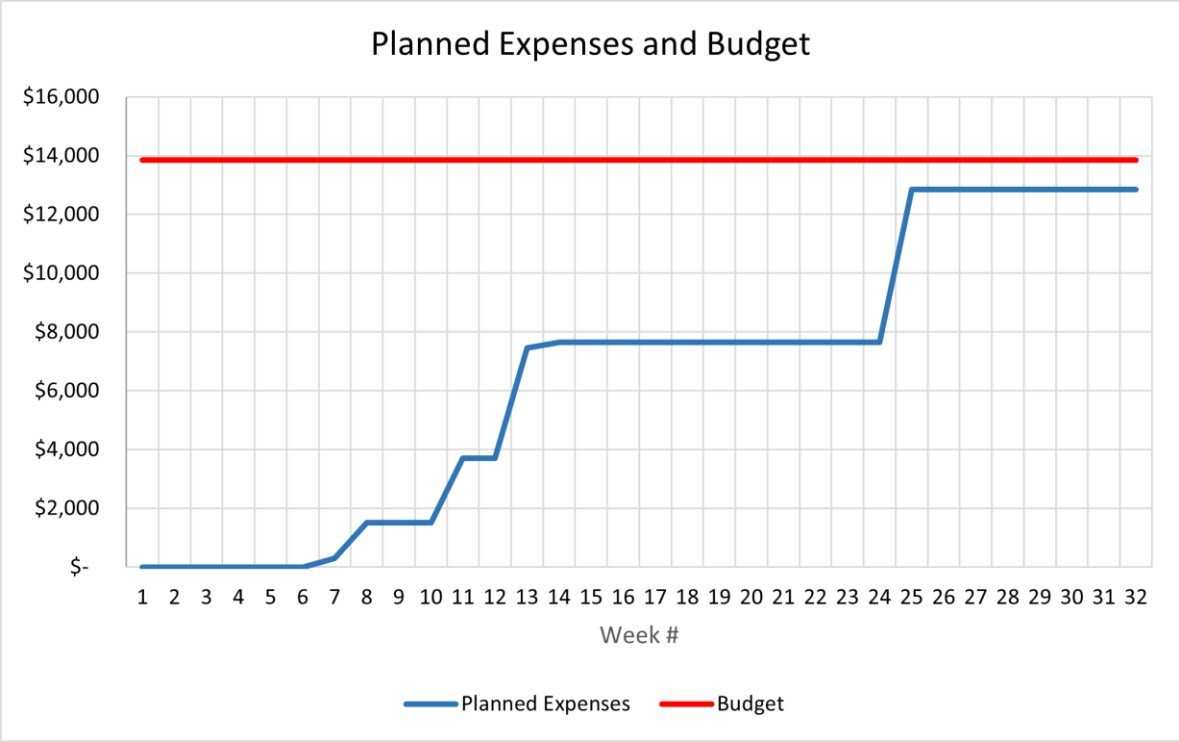

Fig. 7.3 Initial planned expenditures over the course of the project.

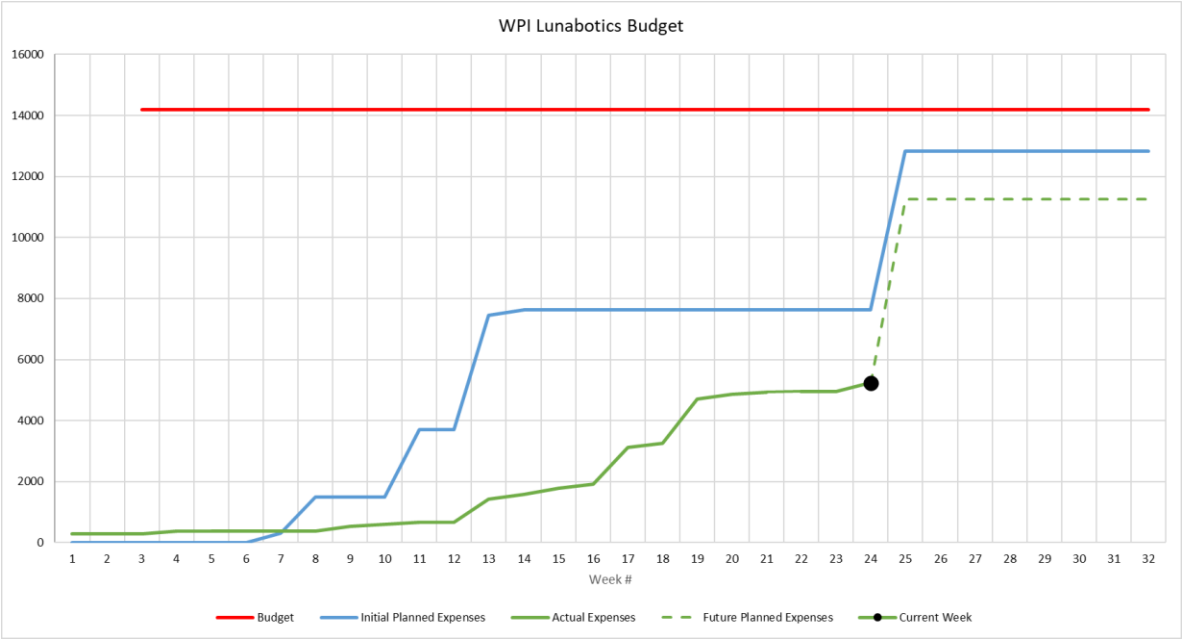

Fig. 7.4 Expenditures as of February 26th, 2024.

8 Conclusions and Recommendations

The project was able to surpass several key objectives, most notably mobility and mass goals. The robot has a highly articulated drive base which allows it to easily move, even in rough or uneven terrain. We have seen many past Lunabotics robots struggle with mobility, a major reason why we emphasized it this year. Regarding mass, although we were not able to achieve our reach goal of 20 kg, the team made significant strides in reducing the mass of our subsystems. In fact, Muffin (a ~28 kg robot) has roughly a 35% mass reduction of its predecessor: Comet (~45 kg). This mass reduction has real world implications because the SLS (Space Launch System) which is used for the Artemis Mission can bring ~46 metric tons of payload into a trans-Lunar injection orbit [26]. The cost to bring each kilogram of payload to the moon is roughly $1.2 million, so any mass reductions equate to a significant cost savings [3].

Some aspects of the project that we struggled with were assembly and maintenance of several subsystems, with the intake subsystem presenting the largest challenge. We found that the tension block lacked sufficient range to tension the chain. The block was designed with the capability to tension the length of exactly two links. This means that if the chain length terminated at the end of block's range, removing or adding two links would not have much effect. Future teams can mitigate this issue by ensuring the tension range is larger than the required length to tension two links. In addition, we tightly packaged the intake and deposit subsystems to meet the robot's size requirements. Although this made assembly and maintenance of hardware a great challenge, we believe that there were great benefits of these dense subsystems. Nonetheless, it is important for future teams to consider assembly and maintenance when designing such subsystems.

Managerially, the team recommends future teams to pay great attention to their timeline. The team created and updated a Gantt chart displaying important milestones to present at weekly advisor meetings, but sometimes lost sight of major upcoming goals. Using the Gantt chart as a tool to work more efficiently will save time and effort. This project has many moving parts and systems that depend on the completion of other systems. It is important for members working on different subsystems to maintain constant communication, preventing any unforeseen delays or integration issues. We recommend that future teams establish an overarching timeline for their project and routinely discuss progress towards goals to ensure deadlines are met and systems integrate smoothly.

Muffin is a low-berm-output robot due to our design objectives. Because of this, the ground clearance of the robot is marginal to the clearance required from berms built after a 30-minute run. In a real-world scenario, this gives a robot with Muffin's archetype the ability to build wide, short berms. This is presumably unlike the tall berms NASA will require to protect lunar infrastructure. For this reason, Muffin is likely not effective in a lunar application expected by NASA; however, Muffin's archetype is highly effective in the competition's reduced scope.

NASA's Lunabotics Challenge provides students with the ability to test their engineering skills, gain new design experiences, and demonstrate their acquired expertise. While NASA seeks to establish humanities' first long-term presence on the moon, exploring the field of robotics will help to protect and maintain semi-permanent moon structures. Autonomous robots are the future of space exploration, paving the way for lunar colonization.

References

[1] "Artemis - NASA." [Online]. Available: https://www.nasa.gov/feature/artemis/. [Accessed: Oct. 02, 2023]

[2] "Lunabotics Challenge - NASA." [Online]. Available: https://www.nasa.gov/learning-resources/lunabotics-challenge/. [Accessed: Oct. 02, 2023]

[3] "Lunabotics 2024 Guidebook – DRAFT Ver 2.0." NASA [Online]. Available: https://www.nasa.gov/wp-content/uploads/2023/09/a-lunabotics-2024-guidebook-draft-ver-2.0-09.12.2023.pdf

[4] J. Akinyele *et al.*, "NASA Lunabotics 2021-2022." [Online]. Available: https://digital.wpi.edu/pdfviewer/9593tz415

[5] A. Brattstrom *et al.*, "NASA Lunabotics 2022-2023." [Online]. Available: https://digital.wpi.edu/pdfviewer/0k225f55s

[6] "NASA LUNABOTICS 2022," Alabama Astrobotics. [Online]. Available: https://www.alabamaastrobotics.com/nasa-lunabotics-2022.html. [Accessed: Oct. 02, 2023]

[7] "WPI-sponsored Robotics Team Wins $500,000 at NASA Moondust Excavation Challenge | Worcester Polytechnic Institute." [Online]. Available: https://www.wpi.edu/news/2009robot. [Accessed: Oct. 02, 2023]

[8] "$500,000 treasure dug up in lunar soil," New Scientist. [Online]. Available: https://www.newscientist.com/article/dn18001-500000-treasure-dug-up-in-lunar-soil/. [Accessed: Oct. 02, 2023]

[9] Moonraker Full Cycle Demonstration. [Online]. Available: https://www.youtube.com/watch?v=jmMidYBFfTY. [Accessed: Oct. 02, 2023]

[10] "5 Gallon Orange Homer Bucket," *Home Depot*. [Online]. Available: https://www.homedepot.com/p/The-Home-Depot-5-Gallon-Orange-Homer-Bucket-05GLHD2/100087613#overlay

[11] "90368717 - Online Store." [Online]. Available: https://ublegoodvs.life/product_details/90368717.html. [Accessed: Sep. 29, 2023]

[12] "Archimedes screw | Water Pump, Irrigation & Hydraulics | Britannica." [Online]. Available: https://www.britannica.com/technology/Archimedes-screw. [Accessed: Sep. 29, 2023]

[13] "Conveyor Belts: What Is It? How Does It Work? Types, Parts." [Online]. Available: https://www.iqsdirectory.com/articles/conveyor-belts.html. [Accessed: Sep. 29, 2023]

[14] Curran, "This powerful Roomba vacuum is $300 off right now," *CNN*, Feb. 21, 2023. [Online]. Available: https://www.cnn.com/cnn-underscored/deals/roomba-i7-plus-sale

[15] "Amazon.com." [Online]. Available: https://www.amazon.com/River-Hill-Golf-Retriever-Collector/dp/B0B9FPQ9S1. [Accessed: Sep. 29, 2023]

[16] R. G. Budynas and J. K. Nisbett, *Shigley's mechanical engineering design*, 9th ed. in McGraw-Hill series in mechanical engineering. New York: McGraw-Hill, 2011.

[17] "3200 Series Cleated Belt - Dorner Conveyors," *Dorner Conveyors - Conveying Systems and Manufacturing*. [Online]. Available:

https://www.dornerconveyors.com/products/3200-series/3200-belted/cleated-belt. [Accessed: Oct. 01, 2023]
[18] “Manual Grain Gate Open Door Farm Tipping Trailer,” *Depositphotos*. [Online]. Available: https://depositphotos.com/photo/manual-grain-gate-open-door-farm-tipping-trailer-550837612.html. [Accessed: Oct. 01, 2023]
[19] “Electric Gate and Hoist.” [Online]. Available: https://www.shurco.com/products/shur-co-brand/farm-bodies/electric-gate-and-hoist/. [Accessed: Oct. 01, 2023]
[20] “CaDA Articulated Dump Truck C61054W,” *Doublee_CaDA*. [Online]. Available: https://decadastore.com/products/articulated-dump-truck-c61054w. [Accessed: Oct. 01, 2023]
[21] “heavy truck unloading illustration flat style,” *iStock*, Oct. 01, 2018. [Online]. Available: https://www.istockphoto.com/vector/heavy-truck-unloading-illustration-flat-style-gm1047498558-280188899. [Accessed: Oct. 01, 2023]
[22] “Connect 4 Game,” Entertainment Earth. [Online]. Available: https://www.entertainmentearth.com/product/connect-4-game/hga5640
[23] H. M. Beakawi Al-Hashemi and O. S. Baghabra Al-Amoudi, “A review on the angle of repose of granular materials,” *Powder Technology*, vol. 330, pp. 397–417, 2018, doi: 10.1016/j.powtec.2018.02.003.
[24] “Online ArUco markers generator.” [Online]. Available: https://chev.me/arucogen/. [Accessed: Oct. 02, 2023]
[25] “Introduction to A*.” Available: https://theory.stanford.edu/~amitp/GameProgramming/AStarComparison.html. [Accessed: Mar. 01, 2024]
[26] “Space Launch System - NASA.” Available: https://www.nasa.gov/reference/space-launch-system/. [Accessed: Apr. 23, 2024]

Appendix A: Regolith Rate/Capacity Analysis

Regolith Densities		
Max	1800	kg/m3
Min	1500	kg/m3

Robot Properties		
Robot Mass	20	kg
Excavation: Robot Dry Mass	1.2	Unitless
Storage: Robot Dry Mass	1.4	Unitless
Worst Case Regolith Mass	24	kg
Worst Case Regolith Storage	0.019	m3

Type 1 Excavator	**Vertical Auger Diameter**	0.076 [3]	0.127 [5]	0.178 [7]	0.229 [9]	m [in]
	Digging Depth	0.4	0.4	0.4	0.4	m
	# Digging Cycles	7.30	2.63	1.34	0.81	cycles
	Time per Cycle	0.32	0.91	1.78	2.95	min
	Dig Rate	0.02	0.007	0.004	0.002	m/s

Type 2 Excavator	**Conveyor Width**	0.102 [4]	0.102 [4]	0.178 [7]	0.178 [7]	0.229 [9]	0.229 [9]	m [in]
	Thickness	0.102 [4]	0.102 [4]	0.102 [4]	0.102 [4]	0.102 [4]	0.102 [4]	m [in]
	Angle from Vertical	30	30	30	30	30	30	deg
	Digging Depth	0.2	0.4	0.2	0.4	0.2	0.4	m
	Mechanism Length	0.230 [9.09]	0.461 [18.1]	0.230 [9.09]	0.461 [18.1]	0.230 [9.09]	0.461 [18.1]	m [in]
	Required Translate Distance	0.55	0.12	0.27	None	0.19	None	m

Archimedes Screw Diameter	0.076 [3]	0.127 [5]	0.178 [7]	0.229 [9]	m [in]
Angle from Vertical	30	30	30	30	deg
Digging Depth	0.4	0.4	0.4	0.4	m
Mechanism Length	0.461 [18.1]	0.461 [18.1]	0.461 [18.1]	0.461 [18.1]	m [in]
Required Translate Distance	0.242	0.051	None	None	m

Appendix B: Drivetrain Tube Calculations

Tube OD		0.03	0.06	0.09	0.12	0.15	0.18	0.21	0.24	0.27	0.3	0.33	0.36	0.39	0.42	0.45	0.48
1	ID	0.94	0.88	0.82	0.76	0.7	0.64	0.58	0.52	0.46	0.4	0.34	0.28	0.22	0.16	0.1	0.04
	Moment of Inertia	0.010762	0.01965	0.026894	0.032711	0.037302	0.040852	0.043532	0.045498	0.04689	0.047831	0.048431	0.048786	0.048972	0.049055	0.049082	0.049087
	Bending stress	11242.78	6157.79	4499.16	3699.088	3243.837	2961.919	2779.538	2659.44	2580.534	2529.753	2498.378	2480.237	2470.78	2466.608	2465.238	2464.998
	FOS	2.668379	4.871878	6.667912	8.110107	9.248307	10.12857	10.79316	11.28057	11.6255	11.85886	12.00779	12.09562	12.14192	12.16245	12.16921	12.17039
	Mass (g)	179.2826	347.4756	504.5789	650.5926	785.5166	909.351	1022.096	1123.751	1214.316	1293.792	1362.178	1419.475	1465.682	1500.799	1524.826	1537.764
1.25	ID	1.19	1.13	1.07	1.01	0.95	0.89	0.83	0.77	0.71	0.65	0.59	0.53	0.47	0.41	0.35	0.29
	Moment of Inertia	0.021405	0.039807	0.055499	0.068762	0.07986	0.089044	0.096546	0.102587	0.107368	0.11108	0.113894	0.115969	0.117447	0.118455	0.119106	0.119495
	Bending stress	7065.977	3799.625	2725.289	2199.625	1893.933	1698.604	1566.607	1474.365	1408.702	1361.633	1327.987	1304.228	1287.816	1276.854	1269.881	1265.743
	FOS	4.245697	7.895517	11.00801	13.63869	15.84005	17.66156	19.14966	20.34774	21.2962	22.03237	22.59058	23.00212	23.29526	23.49524	23.62426	23.7015
	Mass (g)	225.4895	439.8893	643.1995	835.42	1016.551	1186.592	1345.544	1493.406	1630.178	1755.861	1870.454	1973.957	2066.371	2147.695	2217.929	2277.074
1.5	ID	1.44	1.38	1.32	1.26	1.2	1.14	1.08	1.02	0.96	0.9	0.84	0.78	0.72	0.66	0.6	0.54
	Moment of Inertia	0.037438	0.070478	0.099478	0.124781	0.146717	0.165598	0.181722	0.195371	0.206813	0.216299	0.224066	0.230335	0.235313	0.239191	0.242143	0.244331
	Bending stress	4848	2575.281	1824.53	1454.543	1237.073	1096.026	998.7781	929.0012	877.6057	839.1176	810.0303	787.9822	771.3124	758.8088	749.5566	742.8449
	FOS	6.188118	11.64921	16.44259	20.62503	24.25079	27.37161	30.0367	32.29275	34.18392	35.75184	37.03565	38.07193	38.89475	39.53565	40.02366	40.38528
	Mass (g)	271.6963	532.303	781.8201	1020.247	1247.585	1463.833	1668.992	1863.061	2046.04	2217.929	2378.729	2528.439	2667.06	2794.591	2911.032	3016.384
1.75	ID	1.69	1.63	1.57	1.51	1.45	1.39	1.33	1.27	1.21	1.15	1.09	1.03	0.97	0.91	0.85	0.79
	Moment of Inertia	0.059965	0.113872	0.162144	0.205188	0.243395	0.277142	0.306791	0.332688	0.355163	0.374532	0.391095	0.405138	0.416929	0.426724	0.434762	0.441266
	Bending stress	3531.221	1859.538	1305.936	1031.982	869.9854	764.048	690.2088	636.4826	596.2054	565.3725	541.4284	522.6618	507.8799	496.222	487.048	479.8688
	FOS	8.495646	16.13304	22.97202	29.07028	34.48334	39.26455	43.46511	47.13404	50.31823	53.06236	55.40899	57.39849	59.06908	60.45681	61.59557	62.51708
	Mass (g)	317.9032	624.7167	920.4406	1205.075	1478.619	1741.074	1992.44	2232.715	2461.901	2679.998	2887.005	3082.922	3267.749	3441.487	3604.135	3755.693
2	ID	1.94	1.88	1.82	1.76	1.7	1.64	1.58	1.52	1.46	1.4	1.34	1.28	1.22	1.16	1.1	1.04
	Moment of Inertia	0.090091	0.172199	0.246812	0.314399	0.375415	0.430303	0.479485	0.523372	0.562359	0.596824	0.627132	0.65363	0.676653	0.696519	0.713529	0.727973
	Bending stress	2686.178	1405.348	980.5047	769.7237	644.6192	562.395	504.7082	462.386	430.3302	405.4796	385.8839	370.2399	357.6426	347.4423	339.1592	332.43
	FOS	11.16828	21.34703	30.59649	38.97502	46.5391	53.34329	59.44028	64.88086	69.71391	73.98645	77.74359	81.02854	83.88263	86.34528	88.45405	90.24457
	Mass (g)	364.11	717.1305	1059.061	1389.902	1709.654	2018.316	2315.888	2602.37	2877.763	3142.066	3395.28	3637.404	3868.438	4088.383	4297.238	4495.003

Appendix C: Safety Requirements Checklist

Requirement	Meets?
Robot(s) shall be contained within a payload envelope measuring 1.50 m length x 0.75 m width x 0.75 m height with a maximum mass of 80kg. It may deploy or expand beyond the envelop after the start of each attempt but may not exceed 1.75 m in additional height which is 2.5 m above the surface of the regolith.	Y
Robots shall have a central hoist point or sling system based around the robot's center of gravity (CG).	Y
Robots shall have a minimum of four (4) lifting points, safe for human hands and clearly marked (ISO 7000-1368) for students and NASA staff to use.	Y
The robot can run either by telerobotic (remote control) or in autonomous operations and cannot have any touch sensors to sense and avoid obstacles.	Y
Reference Point Arrow - must mark the forward direction of the mining robot in the starting position configuration (the reference location and arrow pointing forward can point any direction of the team's choosing, except up or down).	Y
The robot shall be equipped with an easily accessible red emergency stop button or "Kill Switch" as follows:	-
• Use sound engineering practices and principles in placing the "Kill Switch" on your robot. It shall be located on the surface of the construction robot and require no additional steps to access it.	Y
• The "Kill Switch" shall have a minimum diameter of 40 mm.	Y
• An unmodified "Commercial Off-The-Shelf" (COTS) red button is required.	Y
• The emergency stop button must stop the construction robot's motion and disable power with one push motion on the button. It must be highly reliable and instantaneous.	Y
• The button should disconnect the batteries from all controllers (high current, forklift type button) and it should isolate the batteries from the rest of the active sub-systems as well. Only onboard laptop computers and data-logger(s) may stay powered on.	Y
The robot must provide its own onboard power. The energy consumed must be recorded with a "Commercial Off-The-Shelf" (COTS) electronic data logger device.	Y
To ensure the robot is usable for an actual mission, it cannot employ any fundamental physical processes, gases, fluids or consumables that would not work in an off-world environment.	Y
You are expected to be aware of the specific hazards associated with your robot.	Y